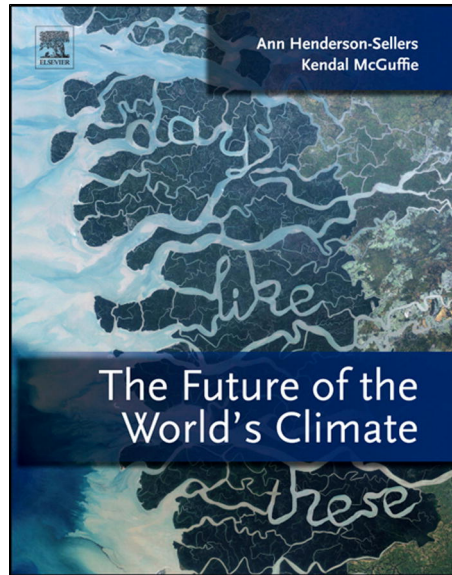


**Provided for non-commercial research and educational use only.
Not for reproduction, distribution or commercial use.**

This chapter was originally published in the book *The Future of the World's Climate*. The copy attached is provided by Elsevier for the author's benefit and for the benefit of the author's institution, for non-commercial research, and educational use. This includes without limitation use in instruction at your institution, distribution to specific colleagues, and providing a copy to your institution's administrator.



All other uses, reproduction and distribution, including without limitation commercial reprints, selling or licensing copies or access, or posting on open internet sites, your personal or institution's website or repository, are prohibited. For exceptions, permission may be sought for such use through Elsevier's permissions site at:

<http://www.elsevier.com/locate/permissionusematerial>

From Harvey, L. D. D. (2012), Fast and slow feedbacks in future climates, in *The Future of the World's Climate*, edited by A. Henderson-Sellers and K. McGuffie, pp. 99–139, Elsevier, Amsterdam.

ISBN: 9780123869173

Copyright © 2012 Elsevier B.V. All rights reserved.

Elsevier

Fast and Slow Feedbacks in Future Climates

Danny Harvey

Department of Geography, University of Toronto, Ontario, Canada

Chapter Outline

5.1. Introduction: The Sensitive Climate	100		
5.1.1. Radiative Forcing	100		
5.1.2. Climate Sensitivity and Feedback Processes	101		
5.1.2.1. Fast and Slow Feedback Process	101		
5.2. Fast-Feedback Climate Sensitivity	101		
5.2.1. Linear Feedback Analysis	101		
5.2.1.1. Relationship between Total Feedback Strength and Climate Sensitivity	103		
5.2.2. Climate Sensitivities of AML Models and AOGCMs	103		
5.2.2.1. Feedback Parameters for Individual Processes in AOGCMs	105		
5.2.3. Observational Validation of the Water Vapour Feedback in AOGCMs	106		
5.2.4. Climate Sensitivity Deduced from Historical Temperature Trends	107		
5.2.5. Climate Sensitivity Deduced from Observed Short-Term Temperature Changes	108		
5.2.6. Climate Sensitivity Deduced from Past Climates and Forcings	110		
5.2.6.1. Late Glacial Maximum	110		
5.2.6.2. Pliocene Climate Sensitivity	110		
5.2.6.3. Palaeocene–Eocene Thermal Maximum (PETM)	110		
5.2.7. Evidence from the Co-variation of Temperature and CO ₂ Over Geological Time	111		
5.2.7.1. Ordovician Glaciations	112		
5.2.8. Climate Sensitivity Deduced from Slow Variations in Atmospheric CO ₂ Concentration	112		
5.2.9. Conclusion Concerning the Fast-Feedback Climate Sensitivity	113		
5.3. Slow Feedback Processes Related to the Carbon Cycle	114		
5.3.1. Oceanic Carbon Cycle Processes	114		
5.3.2. Ocean Carbon Cycle Feedback Processes	115		
5.3.3. Ocean Climate–Carbon Cycle Feedback Processes	115		
5.3.4. Observed Climate-Related Changes in Oceanic CO ₂ Uptake and Related Variables	116		
5.3.4.1. Estimates of Recent Changes in CO ₂ Uptake by the Oceans	116		
		5.3.4.2. Inter-annual and Longer Variations in NPP and Chlorophyll	116
		5.3.4.3. Observed Relationship between Temperature and the Size Distribution of Phytoplankton	117
		5.3.5. Climate–Ocean-Sink Feedbacks as Projected by Models	117
		5.3.6. Terrestrial Carbon Cycle Processes	118
		5.3.7. Terrestrial Carbon Cycle Feedback Processes	119
		5.3.8. Terrestrial Climate–Carbon Cycle Feedback Processes	119
		5.3.8.1. Feedbacks Involving GPP, NPP, and Foliar Respiration	119
		5.3.8.2. Increased Respiration of Soil Carbon	120
		5.3.8.3. Dieback of Middle- and High-Latitude Forests	120
		5.3.8.4. Amazon Ecosystem Collapse	121
		5.3.8.5. Methane Emissions from Wetlands	122
		5.3.8.6. Feedbacks Involving Permafrost Soils	123
		5.3.8.7. Summary	123
		5.3.9. Terrestrial Climate–Carbon Cycle Feedback: Local and Large-Scale Observations	124
		5.3.9.1. Trends in Photosynthesis and Net Primary Productivity	124
		5.3.9.2. Response of NPP to Inter-annual Variability	124
		5.3.9.3. Tree Mortality and Insect Outbreaks	124
		5.3.9.4. Increased Incidence and Severity of Forest Fires	125
		5.3.9.5. Fires in Peatlands	126
		5.3.9.6. Empirical Estimate of the Global-Scale Climate–Soil Carbon Feedback	126
		5.3.9.7. Summary	126
		5.3.10. Destabilization of Methane Clathrate	126
		5.4. Coupled Climate–Carbon Cycle Model Results and Linear Feedback Analysis	127
		5.4.1. Effect of the Oceans in Limiting the Transient Temperature Response	127
		5.4.2. Climatic Change As a Feedback on the Carbon Cycle	129
		5.4.3. The Carbon Cycle As a Climate Feedback	130

5.4.4. Role of Carbon–Nitrogen (C–N) Coupling	132	5.5.2. Shifts in the Distribution of Plant Functional Types	137
5.4.5. Combination of Climate Sensitivity and Carbon Feedback Gain Formulation	133	5.5.3. Decrease in the Extent of the Greenland Ice Cap	138
5.4.6. Applying Climate Sensitivity to Future Climate Policy Strategies	134	5.5.4. Delayed Ocean Circulation Changes and Cloud Feedback	138
5.5. Other Slow and Less-Considered Feedbacks	137	5.5.5. Collapse of Marine Bioproductivity and Cloud Feedback	138
5.5.1. Enhanced Land Surface Warming Due to the Physiological Effect of Higher CO ₂	137	5.6. Climate Feedbacks and the Future Climate	139
		Acknowledgements	139

5.1. INTRODUCTION: THE SENSITIVE CLIMATE

Changes in climate over the coming centuries will be dominated by the effects of human emissions of greenhouse gases (GHGs) and the resulting increase in GHG concentrations, as these effects will overwhelm the long-term effects of natural causes of climatic change, such as changes in solar luminosity, changes in volcanic activity, internally-driven fluctuations in the exchange of heat between the ocean surface layer and the deep ocean, and slow changes in the Earth's orbit (which operate over periods of thousands of years, as discussed by Berger and Yin, 2012, this volume). Human emissions of aerosol precursors as a by-product of fossil fuel use and biomass burning also have a strong effect on climate (largely a cooling effect), but these are particles that last in the atmosphere only for days, requiring a continuous emission source for a sustained effect. The carbon dioxide (CO₂) added to the atmosphere, on the other hand, requires on the order of 100,000 years to be fully removed, while most other GHGs have atmospheric lifespans on the order of 100 years or less. Thus, when the fossil fuel era comes to an end (either due to exhaustion of the fossil fuel resource or through deliberate actions to make the transition to renewable energy), aerosol-cooling effects will drop out and we will be largely left with the accumulated increase in atmospheric CO₂.

The temperature response to increases in the concentration of CO₂ and other GHGs is thus of crucial importance to future climate. The eventual response to a *given* increase in GHG concentrations can be broken into the product of *radiative forcing* and *climate sensitivity*, as outlined below. However, as climate changes, the natural fluxes of CO₂ and methane (CH₄) into and out of the atmosphere will also change, amplifying or diminishing the initial changes in CO₂ and CH₄ concentration. These subsequent changes constitute a *climate–carbon cycle feedback*. In this chapter, that nature of the radiative forcing due to increasing CO₂ is discussed, followed by a comprehensive and critical review of the evidence concerning the magnitude of the climate sensitivity and of climate–carbon cycle and other slow feedbacks. An analytical framework is presented for the quantification of individual climate and climate–carbon cycle feedback processes and on how to combine them in assessing their effect on the eventual climate response. The chapter closes

with some illustrative scenarios of global mean temperature change for low and high future GHG emissions, climate sensitivity, and strength of the positive climate–carbon cycle feedback.

5.1.1. Radiative Forcing

Temperatures within the atmosphere and of the surface tend to adjust themselves such that the absorption of solar radiation is balanced by the emission of infrared radiation to space in the global and annual mean. If we now *impose* a change in the absorption of solar radiation (through, for example, a change in the solar luminosity or the concentration of reflective aerosols in the atmosphere) or in the emission of infrared radiation (by, for example, changing the concentration of GHGs), the temperatures will re-adjust. Because an imposed change in the radiative fluxes drives a subsequent change in temperature, the imposed change is called the *radiative forcing*. Changes in surface temperature respond to the change in net radiation at the tropopause (the boundary between the troposphere and stratosphere), rather than at the surface itself or at the top of the atmosphere. This is because the surface and troposphere are tightly coupled through radiative and non-radiative heat exchanges and so respond together to the net energy input into the combined surface–troposphere system, whereas the stratosphere is largely decoupled from the troposphere (due to the strong inversion at the base of the stratosphere, which inhibits vertical motions across the tropopause) and so can respond independently of the troposphere. Thus, the additional downward emission of infrared radiation from the stratosphere to the troposphere when CO₂ increases adds to the troposphere–surface warming while causing the stratosphere to cool. The cooling of the stratosphere occurs quickly (within months) and subtracts slightly from the initial increase in downward emission at the tropopause. Thus, the relevant forcing for the surface temperature response is the change in net radiation at the tropopause after allowing for adjustment of stratospheric temperatures, but holding all other temperatures constant¹. This is

1. After adjustment of stratospheric temperature, the change in net radiation at the tropopause is the same as the change in net radiation at the top of the atmosphere.

referred to as the *adjusted* radiative forcing, but will usually be referred to as just “the forcing” here. A CO₂ doubling produces a radiative forcing of about 3.5–4.0 W m⁻² in most models (Williams et al., 2008, their table 2). In the absence of stratospheric adjustment, the forcing would be about 4.0–4.5 W m⁻².

5.1.2. Climate Sensitivity and Feedback Processes

The term ‘climate sensitivity’ refers to the ratio of the steady-state (or ‘equilibrium’) increase in the global and annual mean surface air temperature to the global and annual mean radiative forcing. It is standard practice to include only the fast feedback processes, including changes in water vapour, in the calculation of climate sensitivity, but to exclude possible induced changes in the concentrations of other GHGs.

Changes in climate in response to changes in GHG concentrations and other driving factors can be computed using relatively simple climate models in which the climate sensitivity is prescribed and the radiative forcing is computed from the concentrations of individual GHGs using simple formulae based on the results of detailed calculations (as reviewed in Harvey et al., 1997), or they can be computed using 3D atmospheric general circulation models (AGCMs) coupled to a slab that represents the surface layer (mixed layer) of the ocean only (giving atmosphere–mixed layer or AML models). Alternatively, they can be computed using coupled 3D atmospheric and oceanic general circulation models (AOGCMs). In simple models, one can simply add up the individual radiative forcings to get the total global mean radiative forcing, and then apply the climate sensitivity obtained for a CO₂ doubling in simulating the global mean temperature response. AML models and AOGCMs, on the other hand, have the flexibility to respond in separate ways to different forcing mechanisms.

The climate sensitivity is essentially the same for different well-mixed GHGs (and also for ozone if an appropriately adjusted forcing is used), so it is appropriate to compute an *equivalent CO₂ concentration*, which is the concentration of CO₂ alone that would give the same radiative forcing as that produced by the sum of the forcings due to the increases in individual GHG concentrations. For example, the estimated radiative forcings in 2000, due to all the increases of GHGs since pre-industrial times, sum to 2.5–3.7 W m⁻² (Forster et al., 2007, their table 2.12) whereas the forcing for a CO₂ doubling is about 3.75 W m⁻². Thus, the GHG radiative forcing in 2000 was equivalent to a 67%–99% increase in CO₂ concentration, whereas CO₂ alone had increased by only about 32% by 2000.

Although the climate sensitivity is a ratio (temperature change over forcing), it is common to refer to the eventual

global mean warming for a fixed CO₂ doubling (or equivalent CO₂ doubling) as the ‘climate sensitivity’. Henceforth, this is how the term ‘climate sensitivity’ will be used here.

5.1.2.1. Fast and Slow Feedback Process

The fast feedback processes, on which the climate sensitivity depends, include:

- Changes in the amount and vertical distribution of water vapour in the atmosphere
- Changes in the temperature lapse rate
- Changes in the occurrence and properties of clouds
- Changes in the extent of seasonal snow and sea-ice (altering the surface reflectivity or albedo)

In addition to these fast feedbacks, there are a number of slow feedbacks that would further amplify the response to a CO₂ doubling or would lead to further increases in the concentration of CO₂ and other GHGs. These slow processes include:

- Shifts in the distribution and extent of different terrestrial biomes, thereby altering the surface albedo
- Melting and retreat of the Greenland and West Antarctic ice caps (and also the East Antarctic ice sheet if enough warming occurs), thereby adding to the positive surface albedo feedback
- Changes in the natural fluxes of CO₂, CH₄, and other GHGs, and in the production of natural aerosols, leading to changes in their concentrations

This chapter reviews multiple lines of evidence concerning the magnitude of the climate sensitivity as determined by fast-feedback processes, followed by a review of evidence concerning the magnitude of the feedback arising from slow climate–carbon cycle feedbacks and slow shifts in the distribution of vegetation. An analytical framework will be presented that allows the intercomparison and combination of slow and fast feedback processes so as to permit estimation of their interactive effect on long-term changes in global mean temperature.

5.2. FAST-FEEDBACK CLIMATE SENSITIVITY

This section reviews climate sensitivity by first presenting an analytical framework for the analysis of climate feedbacks in computer climate models, as this provides a number of useful insights.

5.2.1. Linear Feedback Analysis

As noted earlier, the temperatures of the atmosphere and surface tend to adjust themselves such that there is

a balance between the absorption of energy from the Sun and the emission of infrared radiation to space. That is:

$$(1 - \alpha_p(T))\frac{Q_s}{4} - F(T) = N(T) = 0 \quad (5.1)$$

where $\alpha_p(T)$ is the planetary albedo, Q_s is the average solar flux density (W m^{-2}) on a plane perpendicular to the Sun's rays, $F(T)$ is the emission of infrared radiation to space, $N(T)$ is the net radiation, and T is the global mean surface air temperature. The first term on the left-hand side is the global mean rate of absorption of solar radiation and the second term is the rate of emission of infrared radiation.

If a radiative perturbation ΔR is imposed that is independent of the radiating temperature, the temperature will tend to adjust such that:

$$(1 - \alpha_p(T))\frac{Q_s}{4} + \Delta R - F(T) = N^*(T) + \Delta R = 0 \quad (5.2)$$

where N^* is the net radiation excluding the radiative forcing. Let T_1 be the temperature that satisfies Equation (5.1) and T_2 be the temperature that satisfies Equation (5.2). Furthermore, write T_2 as $T_2 = T_1 + \Delta T$. Then $N^*(T_2) \sim N(T_1) + (dN/dT)\Delta T$ and:

$$N^*(T_2) + \Delta R = N(T_1) + (dN/dT)\Delta T + \Delta R = 0 \quad (5.3)$$

But $N(T_1) = 0$ by definition, so we get:

$$\Delta T_{eq} = -\frac{\Delta R}{dN/dT} = \frac{\Delta R}{\lambda} \quad (5.4)$$

where $\lambda = -dN/dT = dF/dT - dQ/dT$. It is common to call λ the *radiative damping* or *feedback parameter*. dF/dT and dQ/dT can be expanded as:

$$\frac{dF}{dT} = \frac{\partial F}{\partial T} + \sum_{i=1}^n \frac{\partial F}{\partial I_i} \frac{dI_i}{dT} \quad (5.5)$$

and

$$\frac{dQ}{dT} = \sum_{i=1}^n \frac{\partial Q}{\partial I_i} \frac{dI_i}{dT} \quad (5.6)$$

respectively. The total derivative dF/dT involves the dependence of F on temperature in two ways: a direct dependence on temperature ($\partial F/\partial T$) and an indirect dependence on temperature through the direct dependence of F on various internal variables I_i ($\partial F/\partial I_i$) which, in turn, directly depend on temperature (dI_i/dT). The direct dependence of F on temperature arises through the *Planck function*, which gives the maximum possible rate of emission at each wavelength solely as a function of temperature. The maximum possible emission over all wavelengths, F_{max} , is given by $F_{max} = \sigma T^4$, so $\partial F/\partial T = 4\sigma(T_{eff})^3$ where T_{eff} (the effective radiating temperature of the planet) is the

temperature such that $\sigma(T_{eff})^4$ = the observed emission of infrared radiation to space (for Earth this is about 240 W m^{-2} in the global and annual mean). Q depends on many individual variables, such as cloud amounts and cloud optical properties, and on atmospheric and surface reflectivity, all of which change with temperature, but does not depend directly on temperature (so there is no $\delta Q/\delta T$ term in Equation (5.6)).

As $N(T) = Q(T) - F(T)$, the total derivative dN/dT can be written as:

$$\frac{dN}{dT} = \frac{\partial N}{\partial T} + \sum_{i=1}^n \frac{\partial N}{\partial I_i} \frac{dI_i}{dT} = -\left(\lambda_o + \sum_{i=1}^n \lambda_i\right) \quad (5.7)$$

where $\lambda_o = -\delta N/\delta T = \delta F/\delta T$, $\delta N/\delta I_i = \delta Q/\delta I_i - \delta F/\delta I_i$, and $\lambda_i = -(\delta N/\delta I_i)(dI_i/dT)$. The fast feedbacks involve the direct dependence of F on T and the dependence of F and/or Q on changes in water vapour, temperature lapse rate, clouds, and surface albedo. The total radiative feedback parameter λ can thus be written as:

$$\lambda = \lambda_o + \lambda_{wv} + \lambda_{lr} + \lambda_c + \lambda_a \quad (5.8)$$

where the λ_i represent the inherent strengths of a given feedback process i , with $\lambda_i > 0$ representing a negative feedback and $\lambda_i < 0$ representing a positive feedback. Our physical understanding of the various radiative feedback processes is reviewed in Bony et al. (2006). The overall feedback is negative ($\lambda > 0$, $dN/dT < 0$), as otherwise there could not be a stable climate. The single largest factor contributing to the overall negative feedback is the increase in emission through the Planck function, represented by λ_o , where $\lambda_o = dF/dT|_{T_{eff}} = 4\sigma T_{eff}^3 = 3.76 \text{ W m}^{-2} \text{ K}^{-1}$ for the idealized case of globally uniform warming². λ_o is referred to as the Planck feedback.

The key assumption underlying the above analysis is that the feedbacks due to individual processes do not interfere with each other and so can be simply added together to get the total feedback. That is, that the feedbacks combine linearly. This is not exactly true when combining cloud feedbacks with other feedbacks, but does not introduce a large error. More importantly, considerable qualitative insight can be gained into how climate sensitivity changes as additional positive feedbacks are added when this simplifying assumption is made, as is shown next.

2. At any given location, λ_o is equal to the rate of increase of infrared emission to space with surface temperature when all atmospheric temperatures increase at the same rate as the surface temperature (that is, with fixed lapse rate). Thus, λ_o will be large at low latitudes and small at high latitudes. The global mean value of λ_o is equal to $(\int_A (\delta F/\delta T) dT/dT dA)/(\text{global area})$ and, because surface warming is larger at high latitudes compared to low latitudes, the global mean λ_o will be smaller than the value of 3.76 W m^{-2} obtained by evaluating $\delta F/\delta T$ once at T_{eff} . The greater the polar amplification of the warming, the smaller the global mean value of λ_o will be.

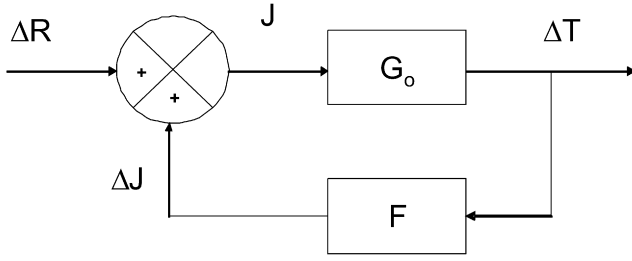


FIGURE 5.1 Block diagram showing a climate feedback loop.

5.2.1.1. Relationship between Total Feedback Strength and Climate Sensitivity

The following analysis is based on Schlesinger (1985). Consider the case where there are no feedbacks except through the direct dependence of infrared emission on temperature (so $dF/dT = \partial F/\partial T$ and $dQ/dT = 0$). The temperature response ΔT can be written as:

$$\Delta T_{eq} = G_o \Delta R \quad (5.9)$$

where $G_o = (\partial F/\partial T)^{-1}$ is the *system gain*. When indirect feedbacks are allowed, the change in temperature leads to a further change, ΔJ , in the net radiation, which then feeds back into the system, as shown in Figure 5.1.

The temperature response is now given by:

$$\Delta T_{eq} = G_o(\Delta R + \Delta J) \quad (5.10)$$

On the assumption that the individual feedbacks are independent of one another, then $\Delta J = \Sigma \Delta J_i$, where each ΔJ_i is the change in net radiation due to the change ΔT_{eq} provoking feedback process i . It can be written as:

$$\Delta J_i = \left(\frac{\partial Q}{\partial I_i} - \frac{\partial F}{\partial I_i} \right) \frac{dI_i}{dT} \Delta T_{eq} = \frac{\partial N_i}{\partial I_i} \frac{dI_i}{dT} \Delta T_{eq} = -\lambda_i \Delta T_{eq} \quad (5.11)$$

If ΔR and ΔJ_i are both positive or both negative, then the feedback involving variable i is a positive feedback since it reinforces the initial heating perturbation. Letting $G = -\Sigma \lambda_i$ (excluding λ_o), we can rewrite Equation (5.10) as:

$$\Delta T_{eq} = G_o(\Delta R + G \Delta T_{eq}) \quad (5.12)$$

Solving for ΔT_{eq} , we obtain:

$$\Delta T_{eq} = \left(\frac{G_o}{1 - f_\lambda} \right) \Delta R \quad (5.13)$$

where $f_\lambda = G G_o = \Sigma f_{\lambda i}$, and:

$$f_{\lambda i} = G_o \frac{\partial N}{\partial I_i} \frac{dI_i}{dT} = G_o \frac{\Delta J_i}{\Delta T_{eq}} = -G_o \lambda_i \quad (5.14)$$

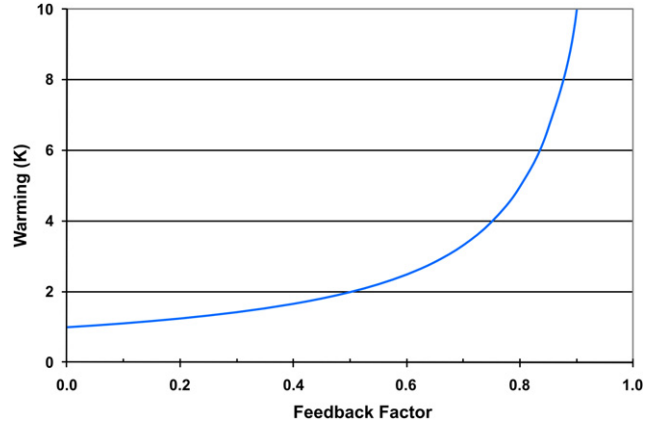


FIGURE 5.2 Equilibrium global mean warming for a CO₂ doubling as a function of the total feedback factor, f_λ .

The variables f_λ and $f_{\lambda i}$ are referred to as the *feedback factor*. The magnitude of $f_{\lambda i}$ is a dimensionless measure of the strength of the feedback involving variable i . The ratio of ΔT_{eq} with all feedbacks to ΔT_{eq} without indirect feedbacks, R_f , is equal to $1/(1 - f_\lambda)$.

Figure 5.2 shows the warming for a CO₂ doubling as a function of f_λ . As $f_\lambda \rightarrow 1$, the temperature change approaches infinity; that is, there is a runaway positive feedback. In deriving the results leading up to this figure, we have assumed that: (i) the strength of each feedback is independent of all the other feedbacks; and (ii) the strength of the feedback does not change as the magnitude or sign of ΔR and ΔT_{eq} changes. In other words, we have assumed that the system is *linear*. Nevertheless, the increase in ΔT_{eq} with increasing f_λ (as more positive feedbacks are added) is decidedly non-linear: a given increase in f_λ has a greater absolute effect on ΔT_{eq} the greater the initial value of f_λ . Thus, the effect of a given feedback on ΔT_{eq} depends on what other feedbacks are already present.

Another important implication of this analysis is that the effect of uncertainty in the sign of a given feedback is not symmetric. Rather, adding a positive feedback has a greater effect on climate sensitivity than adding a negative feedback of the same magnitude.

5.2.2. Climate Sensitivities of AML Models and AOGCMs

It is prohibitively expensive to run an AOGCM until it has reached a new equilibrium after applying a radiative forcing (thousands of years of simulated time would be required). Instead, the sensitivity of an AOGCM has been assumed to be approximately equal to the sensitivity of the corresponding AML model. An AML model does not permit simulation of ocean currents, so the heat transport associated with ocean currents is prescribed and held fixed

as the climate changes. Because of differences in the radiative feedbacks, the AML climate sensitivity will only approximate the climate sensitivity of the AOGCM. Feedbacks can differ because of differences in the initial amount of ice and snow (if there is too much ice and snow, the potential ice–snow feedback is larger), differences in the initial cloud amounts or distributions, and differences in the cloud feedback due to differences in the spatial pattern of temperature change arising from the fact that ocean currents can change in strength in the AOGCM but are implicitly held fixed in the AML.

However, the equilibrium climate sensitivity expected from an AOGCM itself can be estimated without running the AOCGM to a new equilibrium (Gregory et al., 2004; Williams et al., 2008). The temperature change at any given time during the transient satisfies:

$$\Delta T(t) = \frac{\Delta R - N(T)}{\lambda} \quad (5.15)$$

(at $t = 0$, just after ΔR has been applied, $N = \Delta R$, while in the final equilibrium, $N = 0$). Thus, the best-fit slope through a plot of N against ΔT provides an estimate of λ , and extrapolation of the curve to the N axis (where $\Delta T = 0$) gives an estimate of ΔR . However, the ΔR obtained in this way does not agree with the expected ΔR based on the change in net radiation at the tropopause when only stratospheric temperatures are allowed to adjust. Call the forcing obtained from the plot of N against T the effective radiative forcing, ΔR_{eff} (the reason ΔR_{eff} differs from ΔR will be explained later). ΔR_{eff} and λ from the slope of N against ΔT can be used in Equation (5.4) to estimate ΔT_{eq} . Conversely, the equilibrium response that is consistent with the partial transient response of the AOGCM can be estimated as the value of ΔT where the best-fit line intercepts the ΔT axis (where $N = 0$).

This procedure is illustrated in Figure 5.3 for an experiment with an AOGCM in which atmospheric CO_2 concentration increased by 1% per year for 70 years (at which the point the concentration had doubled), then was held fixed while the model was integrated a further 500 years or more. The radiative forcing in this model when CO_2 doubles ($\Delta R'$) is 3.8 W m^{-2} , but the data points in Figure 5.3 lie close to a straight line that extrapolates to an effective forcing ΔR_{eff} of only 2.3 W m^{-2} . The slope of the line going through the point $(0, \Delta R_{eff})$ is much smaller (and the corresponding climate sensitivity much larger) than for a line constrained to go through the point $(0, \Delta R')$. Furthermore, the slope of a line from $(0, \Delta R')$ to successive $(\Delta T, N)$ data points becomes progressively smaller, which corresponds to the effective transient climate sensitivity increasing during the simulation. However, if the slope of the best-fit line is allowed to intersect the net radiation axis at the effective forcing

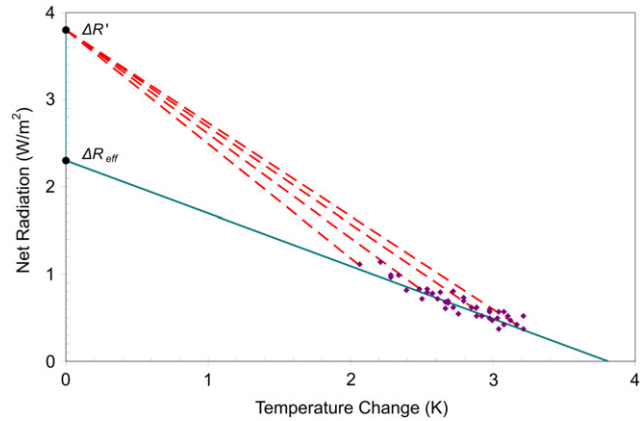


FIGURE 5.3 Example of the determination of the effective radiative forcing and the radiative feedback parameter, from the transient response of an AOGCM. Purple diamonds give model simulated net radiation after various amount of global mean warming. These extrapolate (green line) to a net radiation of 2.3 W m^{-2} at 0 K warming, which is the effective forcing. Lines (red) drawn from the calculated adjusted forcing (3.8 W m^{-2}) to successively later net radiation–warming combinations have a progressively less negative slope, which corresponds to an increasing climate sensitivity. (Source: Williams et al., 2008. © American Meteorological Society. Reprinted with permission.)

(ΔR_{eff}), the effective climate sensitivity during the transient is roughly constant at the higher, final sensitivity.

The reason for this behaviour is that a CO_2 increase induces a rapid adjustment in tropospheric temperatures even with fixed surface temperatures, and this adjustment reduces the net forcing at the tropopause. An increase in CO_2 alters the vertical variation in radiative net heating or cooling within the atmosphere through emission and absorption of infrared radiation, and this in turn causes rapid local changes to the vertical temperature profile that, in turn, alter the stability, vertical mixing, and moisture profile (Gregory and Webb, 2008). Like stratospheric adjustment, these changes occur in much less than one year. It is the adjusted forcing that the ocean sees, so the transient response of the surface is governed by this adjusted forcing and the radiative feedbacks that are triggered as the coupled ocean–troposphere–land surface system warms in response to the adjusted forcing.

Thus, to properly simulate the transient response, we need to break the response into two parts:

- One part that is rapid (within much less than one year) and that produces a change in net radiation that is subtracted from the initial forcing to give the adjusted forcing
- One part that is gradual and driven by the adjusted forcing

If one were interested in only the equilibrium response, the difference between initial and adjusted forcing would not matter, because there would be a compensating change in the deduced equilibrium climate sensitivity. However,

TABLE 5.1 Comparison of Climate Sensitivities Estimated for Various AOGCMs with the Climate Sensitivity of the Corresponding AML Model

Model	ΔR (W m^{-2})	ΔR_{eff} (W m^{-2})	AOGCM ΔT_{eq} (K)	AML ΔT_{eq} (K)
CCSM3	4.0	2.9 ± 0.4	2.4 ± 0.5	2.7
CGCM3.1	3.3	4.0 ± 0.4	2.8 ± 0.4	3.4
ECHAM5	4.0	3.2 ± 0.3	3.7 ± 0.3	3.4
GFDL	3.5	1.7 ± 0.2	3.2 ± 0.2	2.9
GISS	4.1	3.8 ± 0.3	2.4 ± 0.3	2.7
MIROC3.2	3.1	3.2 ± 0.2	4.3 ± 0.3	4.0
HadCM3	3.8	2.3 ± 0.1	3.8 ± 0.2	3.3
HadGEM1	3.8	2.0 ± 0.1	3.4 ± 0.2	4.4

Also shown is the traditional radiative forcing ΔR (based on adjustment of stratospheric temperatures only) for each model and ΔR_{eff} . AOGCM ΔT_{eq} and ΔR_{eff} were computed from transient runs whereby CO_2 concentration increases by 1% per year for 70 years, then is held fixed at a doubling while the simulation continues for at least another 150 years.
(Source: Williams et al., 2008.)

the distinction is relevant for the transient response, because the adjustment in the forcing is not proportional to the evolving temperature change.

Williams et al. (2008) used this approach to estimate the equilibrium climate sensitivity for eight different AOGCMs and compared these with the climate sensitivities of the corresponding AMLs. Results are summarized in Table 5.1, along with ΔR and ΔR_{eff} . AOGCM sensitivities differ by up to 0.6 K from the corresponding AML sensitivities. However, the range in climate sensitivity is similar for the two groups: 2.7–4.4 K for the AMLs and 2.4–4.3 K for the AOGCMs.

5.2.2.1. Feedback Parameters for Individual Processes in AOGCMs

The feedback factors associated with individual feedback processes in an AML model or an AOGCM can be directly computed from the equilibrium or transient changes produced by the model. To do so, one would first compute the global mean net radiation over the course of one year associated with the equilibrium (unchanging) climate prior to applying a radiative forcing. To compute the feedback factor associated with water vapour changes, for example, one would then repeat the calculation of annual net radiation using the new water vapour amounts produced after some period of simulated time following an increase in CO_2 , but using the original values for all other variables including temperature. The difference in global mean net radiation gives ΔJ_{wv} , from which the product λ_{wv} and f_{wv} can be computed using the difference in global mean temperature. This is referred to as the partial radiative

perturbation method, and agrees to within a few percent with a more accurate method developed by Soden et al. (2008).

Figure 5.4a compares the radiative feedback parameters for different feedback processes for 14 different AOGCMs computed in this way. There is a large spread in the calculated feedbacks for water vapour and for lapse rate changes. However, the water vapour and lapse rate feedbacks are negatively correlated, as can be seen in Figure 5.4b, which plots the water vapour feedback parameter against the lapse rate feedback parameter. The negative correlation arises because relative humidity (RH) in the upper troposphere tends to be constant as temperatures change. Thus, a decrease in lapse rate as the climate warms (which occurs in the tropics) serves as a negative feedback (because temperatures in the upper troposphere then increase faster than at the surface, leading to stronger radiative damping to space) but, subject to constant RH, the amount of water vapour in the upper troposphere will increase more than if the lapse rate were constant, which produces a stronger positive water vapour feedback. Thus, the uncertainty in the combined water vapour + lapse rate feedback is much less than the uncertainty in the individual feedbacks (as seen from Figure 5.4a). The albedo feedback is positive, but modest. There is a large uncertainty in the cloud feedback, which ranges from near zero to strongly positive. The final column of Figure 5.4a shows the net feedback for each model. Combined with the λ_o for each model, the overall feedback parameter ranges from $0.88 \text{ W m}^{-2} \text{ K}^{-1}$ to $1.63 \text{ W m}^{-2} \text{ K}^{-1}$, which, assuming a radiative forcing of 3.8 W m^{-2} , corresponds to a climate sensitivity ranging from 4.3 K to 2.3 K.

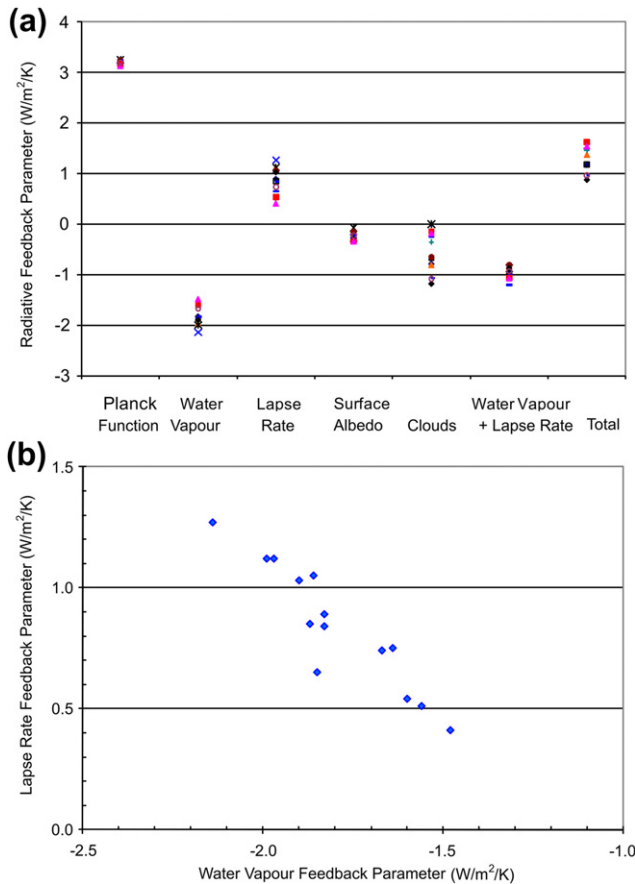


FIGURE 5.4 (a) Radiative feedback parameters for changes in water vapour, lapse rate, surface albedo, clouds, and water vapour + lapse rate, as estimated from 14 AOGCMs. (b) Relationship between water vapour and lapse rate feedback parameters in 14 AOGCMs. (Source: Soden and Held, 2006.)

5.2.3. Observational Validation of the Water Vapour Feedback in AOGCMs

The water vapour feedback is a consistently strong positive feedback in AGCMs, with absolute humidity increasing with warming by an amount that roughly holds RH constant. This matches observations. Observed trends in both surface (Dai, 2006) and lower and middle tropospheric (McCarthy et al., 2009) humidity are very close to what is required to maintain constant RH. In the upper troposphere, where water vapour is particularly effective as a GHG, Gettelman and Fu (2008) find that RH, averaged over the region from 30°S to 30°N, increased by $2 \pm 2\% \text{ K}^{-1}$ at 250 hPa over the period September 2002 to February 2007. Similar trends are obtained in simulations with an AGCM driven with observed changes in sea surface temperature (SST). Minschwaner and Dessler (2004), in contrast, found RH to be decreasing by $4.8 \pm 1.7\% \text{ K}^{-1}$ at 215 hPa between $\pm 20^\circ$ latitude over the period 1992–1997. Seventeen AOGCMs driven by GHG and other forcings simulated

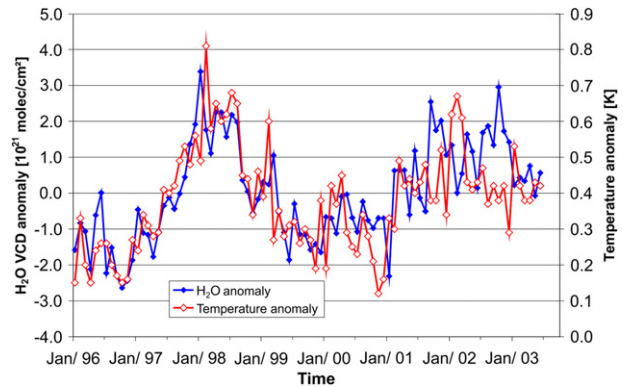


FIGURE 5.5 Variation in globally averaged precipitable water and surface temperature under clear sky conditions for the period 1996–2003. (Source: Wagner et al., 2006 © Copyright 2006 American Geophysical Union. Reproduced/modified by permission of American Geophysical Union.)

a decrease over the period 1980–2000, ranging from 1% K^{-1} to 4% K^{-1} (Minschwaner et al., 2006), so there is a tendency in the models for absolute humidity in the upper tropical troposphere to increase slightly faster than observed over the period 1992–1997.

Wagner et al. (2006) assessed global trends in total column precipitable water under mainly clear sky conditions over the period 1996–2003, as measured by the Global Ozone Monitoring Experiment. They find that variations in globally averaged precipitable water and surface temperature are highly correlated at monthly and longer timescales (Figure 5.5). However, over Northern Hemisphere (NH) continents, there is much scatter in the correlations, and trends in precipitable water can be opposite to trends in surface temperature in some regions.

It is possible to compare the water vapour, lapse rate, and cloud feedbacks predicted by AOGCMs to operate during short-term oscillations, such as the seasonal cycle or inter-annual variability, with those observed in the real atmosphere. However, such a comparison is only a partial test of the correctness of the processes in AOGCMs that determine the feedbacks in response to long-term forcing, because the feedbacks that operate in the long-term response to an increase in GHGs are likely to be quite different from the short-term feedbacks (due to different changes in spatial temperature gradients and in the atmospheric circulation in response to the seasonal cycle, El Niño oscillations, and long-term climatic change). Dessler and Wong (2009) compared the water vapour feedback over the period 1979–2002, as simulated by 10 AGCMs with that computed from re-analysis data³ for the period 1979–2002; the AGCMs were driven by observed variations in SST and sea-ice which, apart from the long-term

3. These are the fields simulated by meteorological forecast models that are continuously nudged towards intermittent observations.

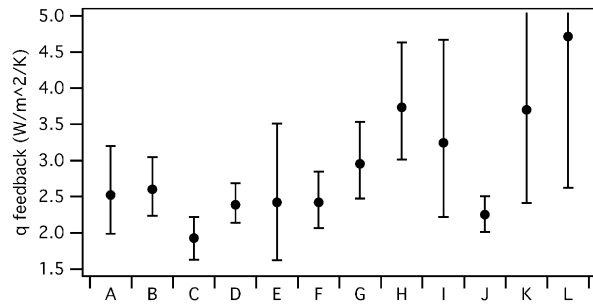


FIGURE 5.6 Comparison of the global mean water vapour radiative feedback parameter as estimated by 10 AGCMs when forced with observed variations in SST and sea-ice extent for the period 1979–2002 (cases A to J), and as computed from observations using two different re-analysis datasets (cases K and L). (Source: Dessler and Wong, 2009. © American Meteorological Society. Reprinted with permission.)

trend, are largely due to El Niño oscillations. The water vapour feedback (λ_{wv}) in the models (1.5–2.8 $\text{W m}^{-2} \text{K}^{-1}$ for full uncertainty range, 1.7–2.4 $\text{W m}^{-2} \text{K}^{-1}$ based on best estimates only) is similar to, but probably modestly weaker than, the re-analysis dataset (1.7–4.4 $\text{W m}^{-2} \text{K}^{-1}$, with best estimates of 2.5 and 2.8 $\text{W m}^{-2} \text{K}^{-1}$ based on two different re-analysis datasets) (Figure 5.6).

Another indication of the reliability of water vapour processes in AGCMs is the excellent agreement found between model-simulated and observed variations in emitted radiation at wavelengths sensitive to the amount and distribution of water vapour in the troposphere (the 6.3 μm brightness temperature) following the eruption of Mount Pinatubo in 1991 (Soden et al., 2002).

In summary, computer climate models simulate an increase in absolute humidity at all levels in the atmosphere with increasing temperature that is sufficient to hold RH approximately constant. This is true both for inter-annual variations driven by observed changes in SST and for longer term changes, and makes the water vapour feedback in models a significant positive feedback. Comparison of AOGCM or AGCM simulations with a variety of observations (or with re-analysis data) indicates that models either slightly overestimate or slightly underestimate the strength of the water vapour feedback compared to the real climate system, depending on the observational dataset used and time period considered.

5.2.4. Climate Sensitivity Deduced from Historical Temperature Trends

The variation in global mean surface temperature over the past 150 years, for which there are good observations (Brohan et al., 2006), depends on the total radiative forcing, the rate of absorption of heat by the oceans, and the climate sensitivity. The total radiative forcing is the sum of forcings due to increasing GHG concentrations; changes in the

atmospheric loading of various aerosols (sulfate, nitrate, reflective organic compounds, and soot); changes in land use (which alter the surface albedo); changes in the solar luminosity; and variations in the activity of volcanoes. With the exception of soot, aerosols have a cooling effect on climate by increasing the reflection of sunlight and so offset the heating effect of increasing GHGs to some extent. The most important uncertainty in the radiative forcing is the uncertainty in the forcing due to aerosols. Based on calculations from first principles, the aerosol-cooling tendency could exceed the total forcing from GHGs. However, the true aerosol forcing must have been less than the GHG forcing, as otherwise there would be no net heating and thus no means of explaining the highly unusual warming of the past century.

For a given variation in net radiative forcing over the past century, the surface temperature response and the oceanic heat uptake will be larger the greater the climate sensitivity, but the surface temperature response will be smaller the larger the effective vertical diffusion coefficient in the upper ocean while the oceanic heat uptake will be larger. Thus, if too large a product of radiative forcing times climate sensitivity is offset by too large an ocean diffusivity, the oceanic heat uptake will be too large. Additional constraints arise from the fact that the effective vertical diffusion coefficient for heat (K_v) must be consistent with the effective vertical diffusion coefficient needed for the correct simulation (in non-diffusive models) of the total inventory and vertical distribution of natural and atomic-bomb ^{14}C in the oceans⁴.

With regard to the uncertain aerosol forcing, the larger the aerosol offset, the smaller the net forcing, and so the greater the permitted climate sensitivity for a given oceanic heat uptake while still producing the same observed surface warming. However, the magnitude of the permitted aerosol cooling is constrained by the fact that most of the aerosol cooling is in the NH. If too large a climate sensitivity is offset by too large an aerosol cooling, this will suppress the warming in the NH more than observed (even if the correct global average warming is simulated). On this basis, Harvey and Kaufmann (2002) concluded that aerosols offset, at most, about half of the GHG heating so far, and that the climate sensitivity is likely to be 2–3 K, with a possible extreme range of 1–5 K. They did not systematically vary K_v in their analysis but, rather, chose the K_v deduced by Harvey (2001) and confirmed that their simulated uptake of heat by the oceans fell within observational uncertainties.

Thus, the key unknowns are the climate sensitivity, the aerosol forcing, and the effective diffusion coefficient for

4. For reasons explained in Harvey and Huang (2001), these coefficients differ for heat, CO_2 , and ^{14}C , but the differences are constrained by physical considerations.

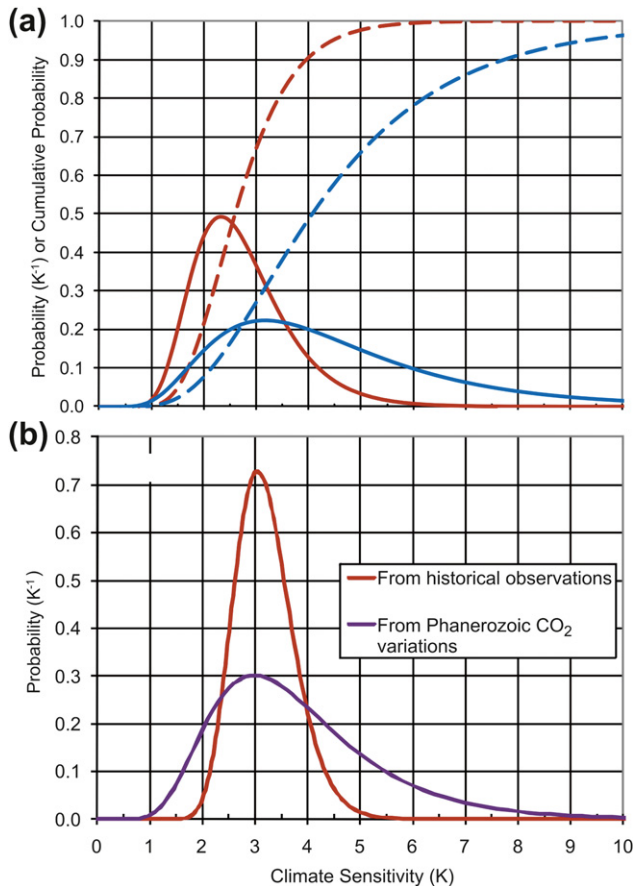


FIGURE 5.7 (a) Illustration of a pdf for climate sensitivity with a 5%–95% probability range of 1.5–4.5 K and a mode of 2.5 K (red curves) or a 5%–95% range of 1.8–9.2 K and a mode of 3.2 K (blue curves) (solid lines are probabilities and dashed lines are cumulative probabilities). (b) pdfs derived by Annan and Hargreaves (2006) with 5 constraints from recent observed changes (red curve), and as derived by Royer et al. (2007) based on the simulation of Phanerozoic CO₂ variations (purple curve).

the oceanic uptake of heat. The observational constraints are the variation in global mean temperature, the variation in NH–SH temperature difference, the change in oceanic heat content, and the amount and distribution of natural and bomb-produced ¹⁴C in the oceans. Uncertainty in the observations can be translated into a probability distribution function (pdf) for climate sensitivity, which gives the probability of the climate sensitivity falling within different climate sensitivity intervals. Two climate sensitivity pdfs are illustrated in Figure 5.7a, one with a 5%–95% probability range of 1.5–4.5 K and a mode (most likely climate sensitivity) of 2.4 K, and the other with 5%–95% range of 1.8–9.2 K and a mode of 3.2 K. The case with a long tail extending to the high climate sensitivities represents a substantially greater societal risk and is representative of many of the pdfs derived in the mid-2000s, but has only a slightly higher mode than the first case. As noted by

Annan and Hargreaves (2006), the long tails are a result of considering, in each study, only a subset of the total body of evidence that could be used to constrain the climate sensitivity. Annan and Hargreaves (2006) show that, when all the evidence is combined together, the long tail is greatly reduced. They estimate that there is less than a 5% probability that the climate sensitivity exceeds 4.5 K and negligible probability that it exceeds 6 K. Their pdf (and a further pdf developed from the simulation of inferred CO₂ variations during the past 420 Ma, which will be discussed later) is shown in Figure 5.7b.

Forest et al. (2008) calculated a 3D pdf associated with joint variation in climate sensitivity, K_v , and aerosol radiative forcing. The pdf was constructed by selecting permissible ranges for all three parameters, choosing some sampling interval for each of the three parameters, and performing simulations of twentieth century climate change for all possible combinations of the three parameters (chosen from the sampled values within the permitted ranges). A given set of parameters is rejected if the corresponding simulation of upper-air temperature, surface temperature, and oceanic heat content is inconsistent with the observed variation in these parameters, given observational uncertainties and the magnitude of internal variability (unrelated to external forcing) as estimated by AOGCMs. Figure 5.8 shows the marginal pdfs for each of these unknown, but adjustable, parameters. The marginal pdf for climate sensitivity (for example) is obtained as follows: the probability of each climate sensitivity interval is given as the proportion of the simulations using a climate sensitivity in that interval and all other combinations of the other two variables that were not rejected, normalized to give a total probability of unity. The 5%–95% probability ranges deduced in this way are 2.0–5.0 K for climate sensitivity, 0.04–4.1 cm² s⁻¹ for the effective K_v , and -0.27 to -0.7 W m⁻² for the aerosol forcing in 1995. Figure 5.9 shows a 2D pdf for climate sensitivity and K_v . The most probable combination is a climate sensitivity of 2.5 K and an effective K_v of 0.7 cm² s⁻¹.

5.2.5. Climate Sensitivity Deduced from Observed Short-Term Temperature Changes

Climate sensitivity has also been estimated based on a variety of short-term observations: the temperature response to the seasonal cycle of solar irradiance, to volcanic eruptions, and to the recent decline in aerosol radiative forcing. In particular:

- Knutti et al. (2006) estimated that there is a 90% probability of the climate sensitivity falling between 1.5–2.0 and 5–6.5 K, with a most likely climate sensitivity of 3.0–3.5 K, based on the temperature response to the seasonal cycle in solar irradiance.

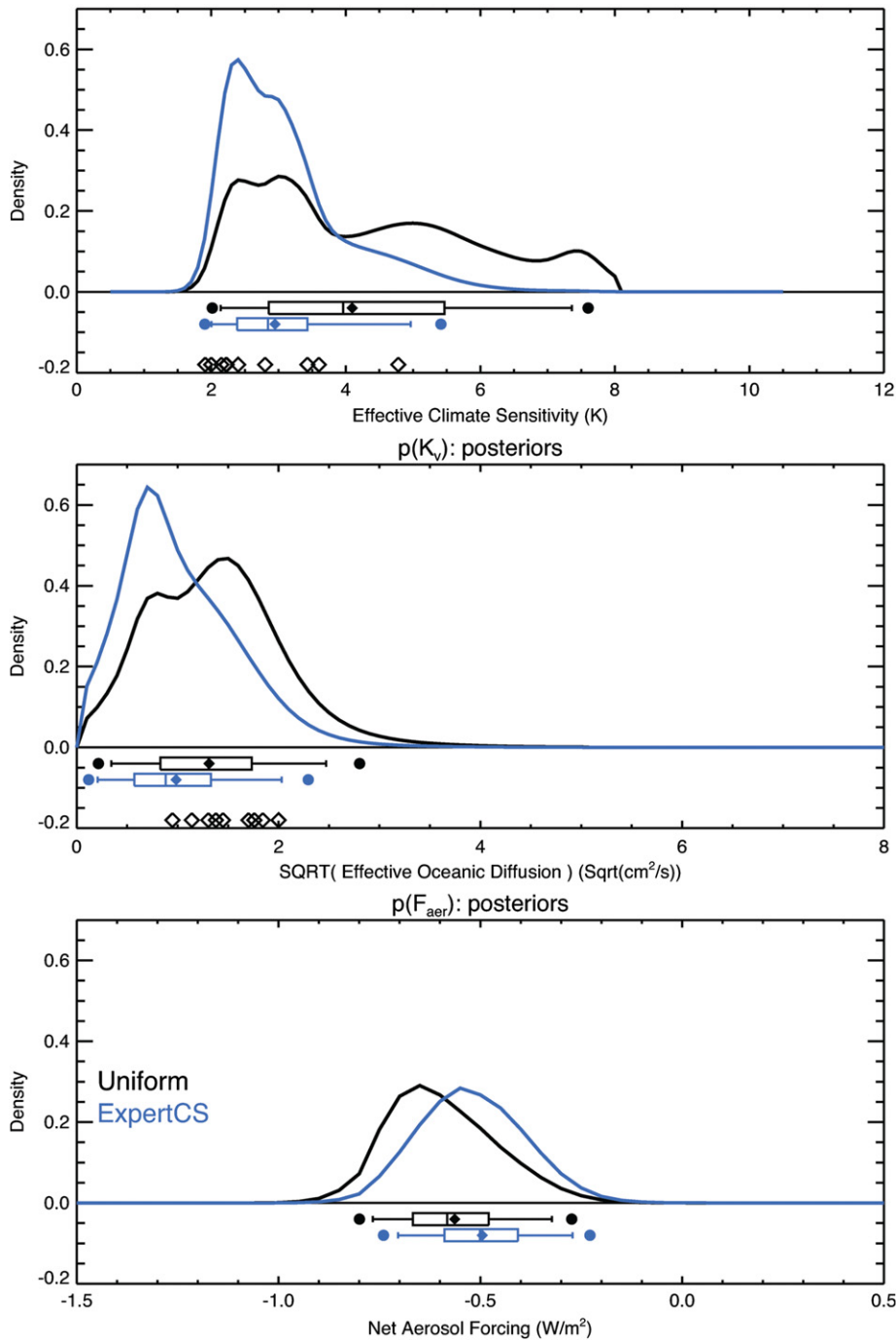


FIGURE 5.8 One-dimensional pdfs for climate sensitivity, effective K_v , and aerosol radiative forcing in 2000 or so as deduced by Forest et al. (2008). The deduced pdfs depend on an initial assumption concerning the shape of the pdf, and results are shown initially assuming the same probability for all values of a parameter within the specified range of probabilities (black curves, uniform priors) or assuming an initial pdf based on expert judgement for climate sensitivity (expert priors, blue curves). The whisker plots indicate boundaries for percentiles 2.9–97.5 (dots), 5–95 (vertical bars at ends), 25–75 (box ends), and 50 (vertical bar in box). Means are indicated by solid diamonds.

- Wigley et al. (2005) concluded that the observed peak temperature response and subsequent rate of recovery to a composite of various volcanic eruptions during the past century appear to rule out climate sensitivities of less than 1.5 K, but cannot rule out sensitivities greater than 4.5 K.
- Bender et al. (2010) estimated a climate sensitivity of 1.7–4.1 K based on the ratio of the integrated temperature response to the integrated radiative perturbation following the eruption of Mount Pinatubo.
- Chylek et al. (2007) computed a climate sensitivity of 2.1–3.4 K based on an estimate in the change in aerosol optical depth over the period 2000–2005, combined with data on the associated change in global mean temperature and a parameterization of the oceanic heat uptake.

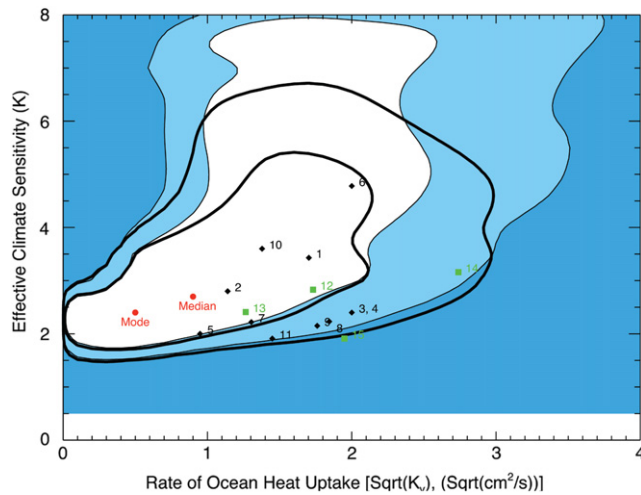


FIGURE 5.9 The joint climate sensitivity, K_s , pdf as deduced by Forest et al. (2008). Diamonds and squares represent parameter combinations required in the MIT 2D ocean model to replicate the behaviour of specific AOGCMs. The inner and outer boundaries of the lightly shaded area represent 10% and 1% significance levels, respectively, for the rejection of specific parameter combinations using uniform priors (defined in the caption to Figure 5.8). The thick black lines show the same thing using expert priors.

Other analyses of the observed response to volcanic eruptions lead to the conclusion that the climate sensitivity is very low, but these analyses have been found to have various flaws.

5.2.6. Climate Sensitivity Deduced from Past Climates and Forcings

If global mean temperature changes and global mean radiative forcing (including that due to slow feedback processes) can be estimated for various times in the geological past when temperatures were substantially different than today, then the climate sensitivity can be estimated. This has been done for the last glacial maximum (LGM) and for warm conditions during the middle Pliocene and at the Palaeocene–Eocene boundary (see also Harrison and Bartlein, 2012, this volume).

5.2.6.1. Late Glacial Maximum

Hoffert and Covey (1992) deduced a climate sensitivity of 1.4–3.2 K based on conditions during the LGM, about 20,000 years ago, while Lea (2004) deduced a sensitivity of tropical SSTs of 4.4–5.6 K.

One of the largest sources of uncertainty in the radiative forcing during the LGM is the negative forcing due to an increase in the content of dust aerosols in the glacial atmosphere. Dust concentrations in Antarctic ice cores indicate large (up to a factor of 50) increases in the rate of dust deposition over Antarctica during the LGM, compared

to the present (Lambert et al., 2008). The uncertainty in LGM aerosol forcing affects the lower limit to the possible climate sensitivity, but not the upper limit. This is because the aerosol forcing adds to the other forcings, so if the aerosol forcing is zero, the total forcing is small and the required climate sensitivity is large, but the required climate sensitivity is an upper limit because the aerosol forcing could not have been positive. On this basis, Schneider von Deimling et al. (2006) estimated an upper limit for climate sensitivity during the LGM of about 5.3 K. Conversely, the larger the aerosol forcing, the smaller the climate sensitivity, but there is no clear upper limit to the possible aerosol forcing and thus no clear lower limit to the climate sensitivity based on glacial conditions.

5.2.6.2. Pliocene Climate Sensitivity

Pagani et al. (2010) estimated a rather high climate sensitivity of 6.1–10.0 K for the middle Pliocene (4 Ma) based on rather convincing indications that the atmospheric CO_2 concentration was only 365–415 ppmv and global mean temperatures were about 2.5–3.0 K warmer than pre-industrial values⁵. This sensitivity includes the effect of slow changes in the distribution of vegetation and the extent of ice sheets, and possible increases in non- CO_2 GHGs as a feedback from climatic change, but does not include positive climate–carbon cycle feedbacks involving CO_2 because the CO_2 concentrations are taken as a given when inferring climate sensitivity.

5.2.6.3. Palaeocene–Eocene Thermal Maximum (PETM)

Just prior to the broad early Eocene temperature peak was a sharp climatic aberration referred to as the Palaeocene–Eocene Thermal Maximum (PETM), occurring on the Palaeocene–Eocene boundary at 55 Ma. This involved a 4–8 K increase in surface and deep-sea temperature in less than 10,000 years (Sluijs et al., 2006). Temperatures subsequently recovered over a period of 200,000 years. This was accompanied by a significant negative deviation in the carbon isotope ratio of marine carbonate sediments (Figure 5.10). The leading theory to explain both the temperature and C-isotope deviations is the release of ~2000–2600 Gt of ^{13}C -depleted CH_4 from CH_4 clathrate deposits (which exist today and are a cause of concern over possible future releases, as explained later). Another brief (one to several million years) warming of 3–6 K (in the southwest Pacific Ocean) developed over a period of 400,000 years during the middle Eocene in clear association with a CO_2 increase by a factor of 2–3 (Bijl et al., 2010).

5. A recent workshop converged on a consensus that Pliocene CO_2 concentration was likely 400 ± 50 ppmv (Schneider and Schneider, 2010).

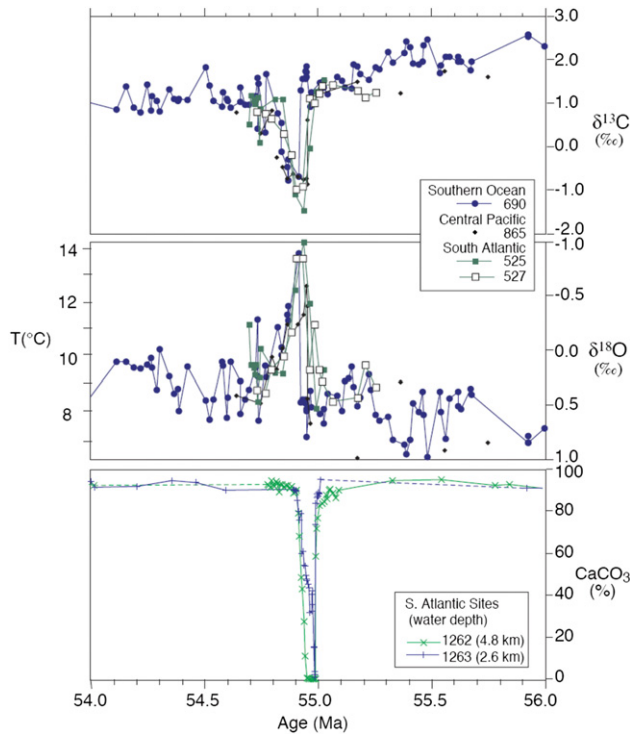


FIGURE 5.10 Co-variation of $\delta^{13}\text{C}$ in marine carbon sediments (an indicator of a CO_2 pulse into the atmosphere), the $\delta^{18}\text{O}$ in marine sediments (an indicator of seawater temperature), and the percentage of CaCO_3 in marine sediments (an indicator of ocean acidity) at the Palaeocene–Eocene transition. (Source: Zachos et al., 2008. Copyright 2008 National Academy of Sciences, U.S.A.)

The negative $\delta^{13}\text{C}$ perturbation seen during the PETM (Figure 5.10) and associated warming can be used to constrain both the magnitude of carbon release and the climate sensitivity at this time. Pagani et al. (2006) worked out combinations of carbon release and climate sensitivity that satisfy the observed excursion in the $\delta^{13}\text{C}$ of -3‰ to -5‰ in marine carbonate sediment, while producing an assumed global mean warming of 5 K during the PETM. If the source of the carbon was CH_4 from CH_4 clathrate (with a $\delta^{13}\text{C}$ of -60‰), then the permitted release is 1800–3500 GtC. To explain a 5 K warming, the required climate sensitivity is 5.5–7.8 K. On the other hand, if the source of the carbon was terrestrial and marine organic carbon (with a $\delta^{13}\text{C}$ of -20‰), the carbon release required to produce a $\delta^{13}\text{C}$ excursion of -3‰ to -5‰ is 5500 to 35,000 Gt and the required climate sensitivity is only 2.3–4.5 K. However, release of 5500–35,000 Gt of organic carbon in such a short time currently defies explanation. Furthermore, Zeebe et al. (2009) estimated the maximum possible release of carbon released during the PETM to be about 3000 Gt, based on two lines of evidence: the shallowing of the carbonate compensation depth (the transition zone between deep water that is unsaturated with respect to calcium carbonate and shallower water that is supersaturated) and the reconstructed deep-sea

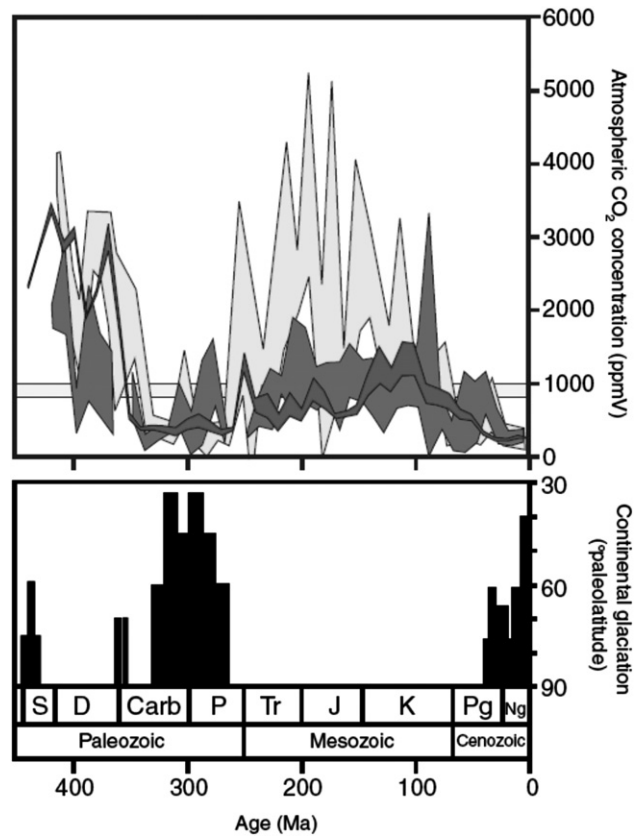


FIGURE 5.11 Inferred variation in CO_2 from carbonate sediments (upper panel) and occurrence of glacial epochs (lower panel) over the past 420 Ma. Blue: model-simulated CO_2 variation; yellow: recent proxy-based estimates of CO_2 variation; red: revised proxy-based estimates of CO_2 variation that take into account the seasonality of carbonate formation. (Source: Breecker et al., 2010. Reprinted by permission from Macmillan Publishers Ltd.)

$[\text{CO}_3^{2-}]$ gradient between different ocean basins. This supports Pagani et al.'s (2006) inference of a high climate sensitivity unless other, unknown, radiative forcings were also at work during the PETM.

5.2.7. Evidence from the Co-variation of Temperature and CO_2 Over Geological Time

There is widespread evidence that variation in atmospheric partial pressure of CO_2 ($p\text{CO}_2$) played an important role in climatic changes during the past 450 million years (see Belcher and Mander, 2012, this volume), a period for which there are various proxy indicators for both atmospheric CO_2 concentration and temperature. CO_2 concentrations have been high during periods of particularly warm climate (such as during most of the Mesozoic era and the Eocene epoch) and low during times of cold climate, including the major epochs with periodic glaciations (namely, the Permian-carboniferous and late Cenozoic glaciations), as illustrated in Figure 5.11 and Figure 14.1 in Harrison and Bartlein, (2012, this volume). In particular, atmospheric $p\text{CO}_2$ was

considerably higher than present during the early Silurian period (423–443 Ma), according to various proxy indicators and carbon cycle modelling, and at the same time, tropical temperatures were 6–8 K warmer than at present (Came et al., 2007). During the Permian and Carboniferous periods, there seems to have been two glacial phases (from 326–312 Ma and 302–290 Ma), each associated with low CO₂ (300–350 ppmv, according to Park and Royer, 2011; but cf. Berger and Yin, 2012, this volume). Atmospheric pCO₂ rose to a broad peak of 1000–1500 ppmv in the mid-Cretaceous period (100 Ma), followed by another decline. Previously, $\delta^{13}\text{C}$ ratios in pedogenic carbonates had been interpreted as implying CO₂ concentrations as high as 4000 ppmv during the Palaeozoic and Mesozoic eras, but the recent discovery that pedogenic carbonate forms preferentially under seasonally dry and warm conditions, rather than throughout the year, has led to a substantial downward revision in the atmospheric CO₂ concentrations estimated from pedogenic carbonates, which are now believed to have never persisted above 1500–2000 ppmv during the past 420 million years (Breecker et al., 2010). The smaller the past CO₂ concentration during warm periods, the greater the climate sensitivity must have been (all else being equal) in order to explain the warmth.

Temperature and CO₂ rose during the Palaeocene epoch (of the Cenozoic era) to a peak in the early Eocene (about 52 Ma), and then a slow decline began. Simultaneous boron, Mg/Ca, and oxygen isotope measurements from the same samples document a decline in temperatures across the Eocene/Oligocene boundary (at 33.7 Ma), along with a decline in CO₂ concentration from 900–1300 ppmv 34.4 Ma to about 700–900 ppmv about 33.5 Ma. At this point, a threshold was reached allowing glaciation of Antarctica to begin (Pearson et al., 2009), as indicated by a step-like increase in the ¹⁸O/¹⁶O ratio that can be explained by the geologically rapid accumulation of isotopically-light ice on land⁶. Continued decrease in atmospheric CO₂ permitted small-scale ice sheets to form first in the NH during the late Miocene (6–10 Ma) (Zachos et al., 2001), while extensive glaciation covering most of Greenland occurred during the late Pliocene, around 3 Ma, at a CO₂ concentration of about 400 ppmv. Tripathi et al. (2009) show that atmospheric CO₂ transitions, as estimated from boron/calcium ratios in foraminifera, closely match inferred climate transitions during the mid-Miocene (5–10 Ma), late Pliocene (5.3–2.4 Ma), and early Pleistocene (1.4–0.9 Ma)⁷.

6. The separation of India from Antarctica, permitting the replacement of north–south ocean currents that transported heat poleward with east–west currents, was likely another factor in the development of ice on Antarctica.

7. The Ba/Ca-based pCO₂ variation continues through to the present and has been validated over the past 800,000 years with the pCO₂ variation that has been directly measured in polar ice cores.

5.2.7.1. Ordovician Glaciations

An apparent exception to the CO₂ temperature correlation presented above is the evidence for short-lived glaciations during the late Ordovician and early Silurian periods (at 460 and 440 Ma), which was also a time of generally high atmospheric CO₂. Early analyses of palaeosol proxies (reviewed by Royer, 2006) suggested CO₂ concentrations of almost 6000 ppmv during the Ordovician period, but more recent analyses and modelling indicate concentrations of only 700–1200 ppmv at 450 Ma, rising to a peak of 1500–1800 ppmv (5–6 times pre-industrial) at 400 Ma (Park and Royer, 2011). Climate model simulations by Herrmann et al. (2004) indicate that a combination of the unusual configuration of the supercontinent Gondwanaland, which was tangent to the South Pole at that time, a solar luminosity that was about 5% lower than at present and either a lowering of sea level from mid-Ordovician levels or ocean heat transport that is reduced by 50% can account for Ordovician glaciations with CO₂ concentrations as high as 15 pre-industrial times. The confounding influences of orbitally induced variations in solar radiation and GHG concentrations are reviewed by Berger and Yin (2012, this volume).

5.2.8. Climate Sensitivity Deduced from Slow Variations in Atmospheric CO₂ Concentration

The atmospheric CO₂ concentration varied in the geological past over periods of million years in response to imbalances between volcanic outgassing and changing rates of weathering due to variations in plate tectonic activity and associated mountain uplift. The magnitude of the CO₂ variation depends in part on a negative feedback between CO₂ concentration and removal rates by chemical weathering, whereby higher atmospheric CO₂ leads to a warmer climate that, in turn, accelerates chemical weathering, leading to more rapid removal of CO₂ from the atmosphere. This feedback, in turn, depends on how large the climate sensitivity is: a small climate sensitivity results in a weaker negative feedback on CO₂ concentration through enhanced weathering and a larger variation in CO₂ concentration on million-year and longer timescales.

Simulations of CO₂ variations during the past 420 million years by Royer et al. (2007) indicate that if climate sensitivity is less than about 1.5 K, impossibly high CO₂ peaks are obtained at certain times while, if it is greater than about 3 K, unreasonably low values are obtained at other times. The main sources of uncertainty are: (i) uncertainty in the real variation in atmospheric CO₂ concentration during the past 420 Ma, which is based on various proxies⁸;

8. Examples include ¹³C/¹²C isotope ratios in phytoplankton and carbonate concretions in palaeosols, stomatal density of fossil leaves, boron/calcium ratios, and boron isotope ratios.

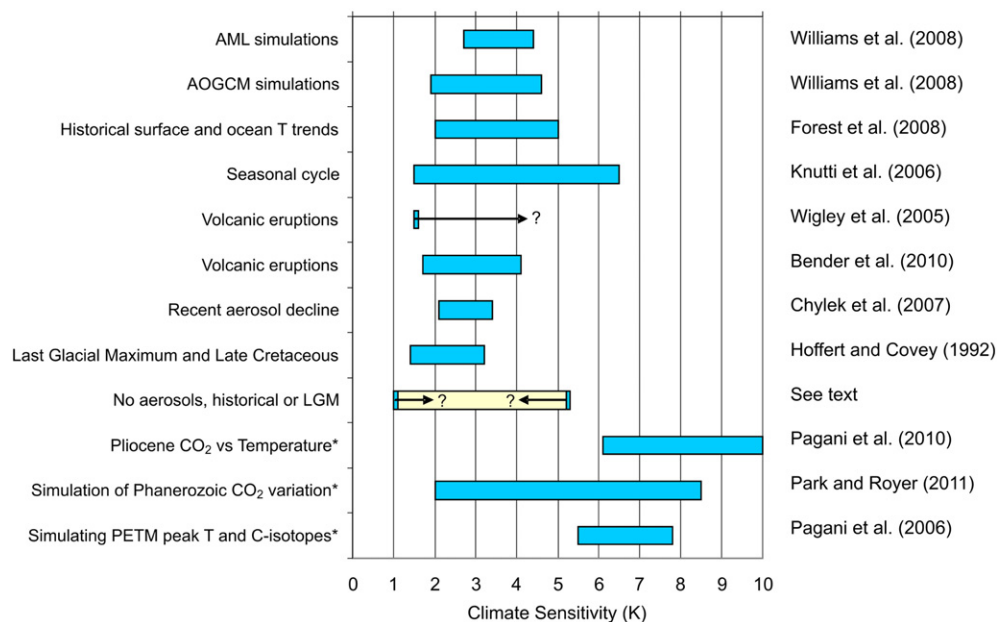


FIGURE 5.12 The range of climate sensitivities calculated using the various estimation methods discussed in this chapter. Methods marked with an asterisk (*) include the effect of changes in vegetation distribution and the full response of ice sheets, but do not include the effect of positive climate–carbon cycle feedbacks as the GHG concentrations are taken as a given in computing the climate sensitivity.

and (ii) uncertainties in four factors other than climate sensitivity that also affect the link between atmospheric CO₂ concentration and the rate of removal by weathering⁹. Assuming that all values of the various parameters in the carbon cycle model are equally likely within their specified uncertainty range, a pdf for climate sensitivity can be generated¹⁰. The resulting pdf is shown in Figure 5.7b. Interestingly, the most probable climate sensitivity from this analysis (3 K) is the same as that deduced by Annan and Hargreaves (2006) from historical data, although – not surprisingly – the uncertainty is much larger, resulting in a very long tail extending out to high climate sensitivities.

Park and Royer (2011) updated the earlier analysis by: (i) using revised weathering rates; (ii) using updated and expanded proxy CO₂ concentration indicators (which reduced the highest CO₂ concentrations previously inferred

to have occurred); and (iii) allowing for a greater climate sensitivity during glacial epochs (260–340 Ma and 0–40 Ma) than during non-glacial epochs during the past 420 Ma. The most probable climate sensitivity deduced for non-glacial epochs remains around 3 K, but the most probable climate sensitivity for glacial epochs (including the present) is about 6 K, with a 99% probability that the glacial climate sensitivity is >2 K¹¹. This greater sensitivity is due in part to the slow albedo feedback arising from changes in the extent of polar ice sheets. The 5%–95% probability range for the glacial climate sensitivity is 3.0–15 K, although little credence can be placed on the upper limit. Like the non-glacial climate sensitivity and 6.1–10.0 K sensitivity range inferred by Pagani et al. (2010) from Pliocene climates, the glacial climate sensitivity would include the effect of changes in the distribution of vegetation zones and any feedbacks between climate and CH₄, N₂O, ozone, and aerosols, but would not include feedback between climate and the CO₂ concentration, since the CO₂ concentrations are given.

5.2.9. Conclusion Concerning the Fast-Feedback Climate Sensitivity

The ranges of climate sensitivities as estimated by the various methods reviewed here are summarized in Figure 5.12. A remarkably wide range of evidence supports

9. These factors are the temperature coefficient for the weathering of calcium and magnesium silicates, the CO₂ fertilization of plant-assisted weathering, the weathering rate ratio of early biota to that of modern trees, and the weathering rate ratio of gymnosperms to angiosperms.

10. The pdf is generated as follows: for each climate sensitivity considered, perform 10,000 simulations (arising from 10 different values for each of four uncertain parameters, giving $10^4 = 10,000$ possible combinations) of the variation in atmospheric CO₂ concentration over the past 420 Ma and count the number of simulations where the statistical misfit between the simulated and proxy CO₂ variation is no greater than the statistical uncertainty in the proxy CO₂ concentrations themselves. The number of simulations where this condition is satisfied for different climate sensitivities indicates the relative probabilities of the various climate sensitivities.

11. The climate sensitivity pdf in this case is essentially the same as that shown in Figure 5.7b, but with the temperature scale multiplied by two.

the long-standing viewpoint that the traditional climate sensitivity (based on fast feedback processes only) is very likely to fall between 1.5 K and 4.5 K. No method indicates a climate sensitivity of less than 1.5 K, but only one method requires a climate sensitivity greater than 4.5 K. Three methods that include slow feedback processes related to changes in the distribution of vegetation and glacier ice caps, as well as other as yet unidentified processes, indicate a substantially larger climate sensitivity, with a consensus climate sensitivity range of 6–8 K.

5.3. SLOW FEEDBACK PROCESSES RELATED TO THE CARBON CYCLE

This section begins with background information on carbon cycle processes in the oceans, followed by an assessment of how the oceanic part of the carbon cycle responds to increases in atmospheric CO₂ concentration in the absence of any change in climate, and then an assessment of known and potential impacts of changes in climate on the oceanic part of the carbon cycle. The same three-step review is presented for the terrestrial part of the carbon cycle (see also Dickinson, 2012, this volume).

In this and subsequent sections, selected results from the simulations of the uptake of anthropogenic CO₂ by the oceanic and terrestrial parts of AOGCMs or other Earth system models are presented. These studies typically used one of the scenarios for emissions of GHGs that was developed by the Intergovernmental Panel on Climate Change (IPCC) in its *Special Report on Emission Scenarios* (Nakicenovic et al., 2000). These are referred to in the remainder of this chapter by the standard designators A1F1, A2, B1, and B2, having cumulative fossil fuel CO₂ emissions to 2100 of about 2300 GtC, 2000 GtC, 1200 GtC, and 1400 GtC, respectively¹².

5.3.1. Oceanic Carbon Cycle Processes

Carbon can occur in the oceans in the following forms:

- As dissolved inorganic carbon (CO₂, HCO₃⁻, and CO₃²⁻), referred to as DIC
- As organic carbon (fleshy material), both in particulate and dissolved form (POC and DOC)
- As CaCO₃ (calcium carbonate), which occurs in two mineral forms: aragonite, used as the structural material of corals, pteropods (high-latitude zooplankton) and some molluscs, and calcite, used as the structural material of the foraminifera (animals ranging in size

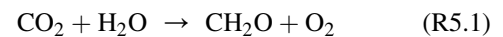
from less than 1 mm to several cm), coccolithophores (a group of phytoplankton), and many other organisms

Less than 1% of the DIC in the ocean surface layer (referred to as the *mixed layer*) is in the form of CO₂, the vast majority occurring as HCO₃⁻ (~90%) and CO₃²⁻ (~10%). Only the DIC in the form of CO₂ can be exchanged with the atmosphere. There will be a net flow of CO₂ from the atmosphere to the ocean if the partial pressure of CO₂ in the atmosphere exceeds the partial pressure of CO₂ in the ocean mixed layer, and vice versa. The mixed-layer CO₂ partial pressure pCO₂ depends on the mixed-layer CO₂ concentration [CO₂] and *solubility* α according to:

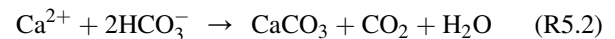
$$p\text{CO}_2 = \frac{[\text{CO}_2]}{\alpha} \quad (5.16)$$

Colder water has a larger solubility than warmer water, so for a given [CO₂], the pCO₂ will be smaller for colder water, which allows cold water to hold more CO₂ and thus more total DIC without exceeding the atmospheric pCO₂.

The production of organic tissue through photosynthesis removes CO₂ from the mixed layer through the reaction:



while the net reaction involving construction of construction of CaCO₃ releases CO₂ to the mixed layer:



The rate of photosynthesis minus respiration by photosynthetic organisms themselves is referred to as *net primary production* (NPP). Most marine organisms construct skeletal material out of silica (SiO₂) rather than CaCO₃, and the construction of SiO₂ has a negligible effect on the concentration of CO₂ in seawater. Much of the organic tissue and calcium carbonate that are produced in the mixed layer is recycled within the mixed layer when organisms die, but some of it sinks into the deeper ocean layers. This is referred to as *export production*. The organic matter largely decomposes within the top 1000 m of the ocean, adding CO₂ to the subsurface water that then slowly diffuses back to the surface. Calcium carbonate dissolves and removes CO₂ from seawater over a much greater depth range. This downward transfer of biogenic carbon (organic matter and CaCO₃) is referred to as the *biological pump* (see Sen Gupta and McNeil, 2012, this volume).

Thus, the main biological parameters affecting the concentration of CO₂ in surface water are: (i) the overall magnitude of the biological pump; (ii) the ratio of organic matter to CaCO₃ production in the mixed layer which, in turn, depends on the proportions of total primary production by calcareous and non-calcareous organisms and the ratio of

12. These sums include the historical cumulative emission of 214 GtC to 1989 plus the 1990–2100 cumulative emissions given in Nakicenovic et al. (2000).

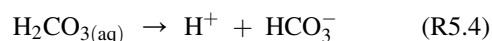
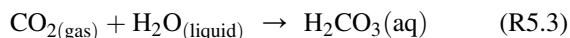
organic matter to CaCO_3 production by calcareous microorganisms; (iii) the proportion of organic matter and CaCO_3 production that sinks from the mixed layer into deeper water; and (iv) the depth intervals over which most of the sinking organic matter and CaCO_3 decomposes or dissolves.

Carbon is also transferred vertically through convective mixing at high latitudes, through the large-scale overturning circulation (which includes sinking of cold water at high latitudes), and through diffusive mixing. Convection and overturning cause a net downward transfer of carbon due to the fact that the DIC concentration is greater in the sinking water than in the rising water which, in turn, is related to the fact that sinking waters are cold and thus have a higher solubility for CO_2 . This downward transfer is therefore referred to as the *solubility pump*. Combined with the biological pump, this causes the DIC concentration to be much higher in the deep ocean than in the mixed layer. In steady state, the downward transfers are balanced by an upward transfer through diffusion.

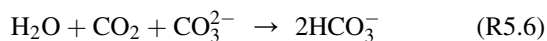
Over most of the ocean, photosynthesis is limited by the availability of nutrients, particularly nitrogen (N). Nutrient concentrations are greater in the deep ocean than in the mixed layer (due to their continuous release by the decay of falling organic matter and continuous consumption during photosynthesis in the mixed layer). However, convective mixing and the upwelling branches of vertical overturning cells add nutrients to the mixed layer, thereby facilitating greater NPP as long as light is not a limiting factor.

5.3.2. Ocean Carbon Cycle Feedback Processes

In response to anthropogenic emissions of CO_2 into the atmosphere, the atmospheric partial pressure rises above that of the ocean mixed layer, causing a net transfer of CO_2 into the surface water. The absorption of CO_2 by the mixed layer is rapidly followed by the chemical reactions:



To the extent that these reactions proceed to completion, the net reaction is:



Reaction (R5.4) would tend to increase the acidity of seawater as CO_2 is added, except that CO_3^{2-} consumes the H^+ that is released by Reaction (R5.4), so that there is no change of pH as long as the occurrence of Reaction (R5.4) is balanced by Reaction (R5.5). The carbonate ion thus acts as a buffer, inhibiting changes in pH to the extent that it is

available. However, the supply of CO_3^{2-} in the surface layer of the ocean is limited, so as more CO_2 is absorbed by the ocean, the H^+ concentration – and hence acidity – of ocean water increases (some of the added H^+ reacts with OH^- , so the OH^- concentration decreases). At the same time as ocean acidity increases, the concentration of CO_3^{2-} decreases, thereby reducing the degree of supersaturation of surface water with respect to aragonite and calcite and reducing the ability of the mixed layer to absorb additional CO_2 .

In sum, the direct response of the ocean to the addition of anthropogenic CO_2 to the atmosphere is to absorb some of the added CO_2 , thereby reducing the increase in CO_2 concentration. The oceanic part of the carbon cycle (like the terrestrial biosphere) thus acts as a negative feedback on the increase in atmospheric pCO_2 ¹³. This negative feedback will be altered in a variety of ways related to the increase in the dissolved CO_2 and H^+ concentrations and decrease in the OH^- and CO_3^{2-} concentrations, as discussed by Riebesell et al. (2009) and Sen Gupta and McNeil (2012, this volume).

5.3.3. Ocean Climate–Carbon Cycle Feedback Processes

Warming of the climate will affect the oceanic uptake of CO_2 through direct effects on the solubility of seawater, through direct effects on the biological pump, and through indirect effects on the biological pump related to changes in vertical mixing. These are briefly discussed here.

Riebesell et al. (2009) estimate that the reduction in mixed layer solubility, as climate warms over the next century under a business-as-usual emission scenario, will reduce the cumulative uptake of anthropogenic CO_2 by 9%–15% by 2100. Cao and Jain (2005) estimate that warming reduced the oceanic uptake of CO_2 by 7%–9% during the 1980s and by 6%–8% over the entire period 1765–1990.

Warmer temperatures will directly affect the biological pump through:

- Induced changes in rates of biological processes, including respiration in the mixed layer (López-Urrutia et al., 2006; Vázquez-Domínguez et al., 2007) and of falling organic carbon (Kwon et al., 2009)
- Induced changes in species composition (ecosystem structure), thereby affecting overall NPP (independently of changes in nutrient supply), the fraction of NPP that is exported from the mixed layer to the deep ocean, the depth over which falling organic particles decompose, the C:N ratio of falling organic carbon, and the ratio of

13. This is a carbon cycle feedback, rather than a climate–carbon cycle feedback, as it does not involve changes in temperature.

organic carbon to carbonate export (Bopp et al., 2005; Omta et al., 2006)

Warming is initially greater at the ocean surface than below the surface, thereby making the surface layer lighter relative to the underlying water and reducing the intensity of convective and diffusive mixing. This, in turn, has the following effects:

- Reduced upward transfer of nutrients, thereby reducing NPP and the strength of the biological pump in regions (such as tropical and middle latitudes) where the biological pump is limited by nutrients (this will affect the large background biopump flux as well as any change in the biological pump due to the direct effect of higher dissolved CO₂ and warmer temperatures)
- Reduced downward mixing of phytoplankton, resulting in a shallower average depth of phytoplankton and therefore a greater availability of light and, in regions (such as high latitudes) where light is a limiting factor, an increase in the strength of the biological pump
- Reduced upward transfer of DIC, thereby reducing the outgassing of natural CO₂
- Reduced downward mixing of anthropogenic CO₂

As well as reducing convective and diffusive mixing, global warming will alter the thermohaline overturning circulation by altering the large-scale density gradient (which depends on the spatial variation in temperature and salinity). In 18 out of 19 AOGCMs examined by Meehl et al. (2007), there is a transient weakening in the thermohaline overturning circulation in the Atlantic Ocean as the climate warms (see Latif and Park, 2012, this volume). Circulation changes are projected to reduce the uptake of anthropogenic CO₂ by 3%–20% through their effect on the solubility pump (Riebesell et al., 2009).

5.3.4. Observed Climate-Related Changes in Oceanic CO₂ Uptake and Related Variables

Various observations indicate that the warming climate has already started to alter the uptake of anthropogenic CO₂ by the oceans or to alter key processes related to the uptake of anthropogenic CO₂, as reviewed by Sen Gupta and McNeil (2012, this volume) and highlighted below.

5.3.4.1. Estimates of Recent Changes in CO₂ Uptake by the Oceans

As reviewed by Le Quéré et al. (2010), numerous studies over the past decade show that mixed layer pCO₂ has been increasing faster than atmospheric pCO₂ in many parts of the ocean, implying a decreasing oceanic CO₂ sink (in these regions) in spite of increasing atmospheric pCO₂. Among these studies is the analysis of Schuster and Watson (2007), who estimate that uptake of CO₂ by the North Atlantic

between 20°N and 65°N decreased by 0.25 GtC per year between 1994 and 1995 and 2002 and 2005. This is attributed to a decline in rates of wintertime mixing between surface and subsurface waters, which, in turn, is linked to a shift in the North Atlantic Oscillation (NAO). Inverse calculations with atmospheric models indicate that the net uptake of CO₂ in the Southern Ocean (the ocean south of 30°S) weakened by about 0.2 GtC per year over the period 1981–2004 compared to the increase in uptake that would be expected from the increase in atmospheric CO₂ concentration during this time period (Le Quéré et al., 2007). Le Quéré et al. (2010) estimate that climatic change and variability reduced the cumulative CO₂ oceanic uptake over the 1981–2007 time period by 12% compared to what it would have been otherwise (from 66.7 GtC to 59.4 GtC). The rise in atmospheric pCO₂ during this time period would have caused the oceanic sink to increase by 0.32 GtC per year per decade, but climatic change and variability are estimated to have decreased the sink by 0.20 GtC per year per decade – an offset of ~63%. Most of this decrease is estimated to be due to wind-induced changes in ocean circulation. Changes in wind caused increased upwelling of CO₂-rich deep water in the equatorial Pacific and Southern Ocean and, as a consequence, increased outgassing of CO₂. The increased wind and upwelling and reduced CO₂ uptake in the Southern Ocean, in turn, have been successfully simulated by a climate–carbon cycle AOGCM that accounts for the observed depletion of stratospheric ozone (Lenton et al., 2009).

Although the reduced North Atlantic uptake of CO₂ may be a temporary feature due to natural variability in the NAO, the observed changes indicate that changes in winds and ocean mixing do alter the net air–sea CO₂ flux. Similarly, although much of the observed increase in wind speeds over the Southern Ocean and the associated decrease in net CO₂ uptake is likely to be due to the temporary loss of polar stratospheric ozone, global warming is projected to intensify Southern Ocean winds throughout the twenty-first century (Shindell and Schmidt, 2004; Fyfe and Saenko, 2006).

5.3.4.2. Inter-annual and Longer Variations in NPP and Chlorophyll

On an annual to decadal timescale, a strong correlation between global oceanic NPP (as inferred from satellite-estimated chlorophyll mass) and climate variability has been observed. Behrenfeld et al. (2006) and Martinez et al. (2009) found that chlorophyll abundance and SST variations at annual to decadal timescales are inversely related over much of the oceans. This can be explained by enhanced stratification when surface waters are warming, thereby suppressing the upward flux of nutrients through mixing. Consistent with this, Polovina et al. (2008) report that the extent of low-chlorophyll regions in the Atlantic

and Pacific oceans increased by 15% between 1998 and 2006, but the increase is much larger than would be expected based on model projections of increasing ocean stratification.

Based on thousands of records of ocean surface water transparency made with Secchi disks since 1899, Boyce et al. (2010) estimate that the global abundance of phytoplankton has declined by an average of 0.9% per year over the period 1950–2003. A decrease in phytoplankton abundance over the 1980–2000 period in the North Atlantic is consistent with the analysis of seawater pCO₂ data by Lefèvre et al. (2004); they find that the seawater pCO₂ increased faster than atmospheric pCO₂ between 1982–1998, which would have led to a weakening CO₂ sink, and they suggest that decreasing biological activity is the explanation.

5.3.4.3. Observed Relationship between Temperature and the Size Distribution of Phytoplankton

It is a well-known principle in aquatic ecology that warmer temperatures favour smaller-sized species and, within a given species, result in smaller mean body size (Daufresne et al., 2009).

In agreement with this principle, Morán et al. (2010) find, based on data collected from research cruises from 1994 to 2005 in the northwest Atlantic, that the proportion of total phytoplankton biomass as picophytoplankton (unicellular organisms in the 0.2–2.0 μm size range) in different locations increases with increasing water temperature throughout the –0.6–22°C temperature range, while the mean picophytoplankton cell size decreases. Assuming that the adjustment of phytoplankton to changing temperature over time is the same as the adjustment over space, global warming should lead to a gradual decrease in phytoplankton size. This, in turn, would tend to reduce the export of carbon into the deep ocean, thereby slowing the oceanic absorption of anthropogenic CO₂.

There is evidence that recent warming has already altered species body size in marine ecosystems. Based on data from the Continuous Plankton Recorder (CPR) survey, which has operated monthly in the North Atlantic Ocean and North Sea since 1946, Beaugrand et al. (2008, 2010) find that the zone of higher copepod diversity south of 45–55°N in the North Atlantic Ocean has shifted northward over time as SST has warmed, but that mean copepod body size has decreased.

5.3.5. Climate–Ocean–Sink Feedbacks as Projected by Models

The oceanic part of the carbon cycle can be simulated using a variety of different models, the most complex being 3D

ocean general circulation models (OGCMs) in which the distribution of temperature, DIC, alkalinity, and other chemical properties is computed and the mixed layer pCO₂ and the atmosphere–ocean CO₂ flux is computed from these. The OGCMs contain subroutines that compute biological processes (NPP, respiration, and the export of carbon to the deep ocean) based on temperature, availability of light and nutrients, and on other factors.

Crueger et al. (2008) assessed the impact of climate feedbacks on the oceanic uptake of CO₂ as simulated by the Max Planck Institute Earth system model. The feedback processes in the model include:

- Temperature effects on solubility
- Reduction in the vertical mixing of CO₂ and nutrients
- Changes in the large-scale overturning circulation
- Reductions in the extent of sea-ice, which allow for air–sea gaseous CO₂ exchange in regions formerly covered with sea-ice, and allow greater absorption of solar radiation, thereby stimulating the biological pump
- Changes in wind speed, which influence the air–sea gaseous exchange in ice-free regions

The net result of these feedbacks is negligible until about 2050, after which the oceanic uptake for simulations with and without climatic effects on the oceanic uptake begins to diverge. By 2100, the oceanic uptake is 5.0 GtC per year without climatic feedbacks and 4.5 GtC per year with feedbacks for the A2 emission scenario – a reduction of about 10%. Averaged over 100 years, the difference would be about 25 GtC, which corresponds to a difference in atmospheric CO₂ concentration of about 12 ppmv, neglecting any response of the terrestrial biosphere to the reduced oceanic uptake.

Chuck et al. (2005), using the HadOCC model with an emission scenario that leads to 701 ppmv atmospheric CO₂ by 2100, find the following impacts on atmospheric CO₂:

- Increase surface temperature by 4 K: +22 ppmv
- Double the maximum growth rate of phytoplankton: –3.9 ppmv
- Change calcite production rate by ±50%: ±4.3 ppmv
- Decrease particle flux to deep ocean by 25%: +16 ppmv
- Increase particle flux to deep ocean by 25%: –8.4 ppmv

Steinacher et al. (2010) simulated changes in primary productivity and the export of particulate carbon to the deep ocean using four different ocean biogeochemistry models (IPSL, MPIM, CSM1.4, and CCSM3). Simulated NPP for present conditions ranges from 24 GtC per year to 49 GtC per year, with only one model falling within the observational estimate of 35–70 GtC per year. All four models show a decrease in NPP over the course of the next century under a high-emissions scenario, with the decrease ranging from 2% to 13% of current NPP. The decrease is driven by reduced overall delivery of nutrients to the surface due to

increased stratification and a slower thermohaline overturning circulation. However, as Chuck et al. (2005) find that decreasing the particle flux to the deep ocean by 25% increases atmospheric CO₂ by only 16 ppmv, a large effect is not expected from the changes in NPP.

In summary, feedbacks between climate and the oceanic part of the carbon cycle are not expected to be large, even in response to large (50%) changes in the rate of calcite production or large (25%) changes in the export of particulate organic carbon.

5.3.6. Terrestrial Carbon Cycle Processes

The key processes in the terrestrial part of the carbon cycle are gross photosynthesis (referred to as *gross primary production* or GPP), respiration by plants themselves (autotrophic respiration), and respiration by decomposers and higher animals (heterotrophic respiration). GPP minus autotrophic respiration gives NPP, while NPP minus heterotrophic respiration gives *net ecosystem production* (NEcP). Positive NEcP over a period of many decades is required in order to offset losses due to periodic forest fires or insect outbreaks, and so is not necessarily indicative of a long-term carbon sink (Dickinson, 2012, this volume). The net balance over a period of time spanning many fire and insect-outbreak cycles is referred to as *net biome productivity*.

Decomposition of soil organic matter is the process of: (i) ingestion of organic matter by soil micro-organisms

and their use as an energy source, leading to the release of CO₂ as the organic matter is respired by micro-organisms and secretion of unrespired organic matter in altered form (exudates); and (ii) breakdown of organic materials by enzymes that are secreted by micro-organisms. Soil organic matter is a mixture of thousands of different carbon compounds, each with its own inherent rates of reaction with enzymes. Organic compounds can be physically protected from enzymes if the compounds are inside soil aggregates, and they can be chemically protected if they are adsorbed onto mineral surfaces. The response of soil respiration rate to an increase in temperature can be much less or much greater than expected based on the inherent sensitivity of reaction rates to changes in temperature, depending on how other environmental constraints on decomposition change. These constraints include:

- Physical and chemical protection (discussed above)
- Availability of moisture (both drought and flooding reduce rates of decomposition, the latter by limiting the availability of oxygen, such that only the slower anaerobic decomposition can proceed)
- Freezing

Table 5.2 summarizes estimates of the size of various terrestrial carbon pools. The amount of carbon in soils and litter (>3500 Gt) is estimated to be many times that in living plants above the soil (500–600 GtC) and many times the current atmospheric CO₂ content (780 GtC). Very

TABLE 5.2 Estimated Distribution of Carbon in the Terrestrial Biosphere

Carbon Pool	Global Size (Gt)	Source
Living plants	450–650	Prentice et al. (2001)
Litter, fine (5-yr mean turnover time)	160	Matthews (1997)
Litter, coarse (13-yr mean turnover time)	150	Matthews (1997)
Upland mineral soils	2300	Davidson and Janssens (2006)
Tropical peatlands	70	Page et al. (2004)
NH Permafrost region		
Peatlands, 0–3 m depth	280	Tarnocai et al. (2009)
Other soils, 0–3 m depth	750	Tarnocai et al. (2009)
Yedoma soils, >3 m depth	400	Tarnocai et al. (2009)
Deltas, >3 m depth	240	Tarnocai et al. (2009)
Total	1670	
SH non-tropical peatlands	13–18	Yu et al. (2010)
Total	~4000–5000	

The reduced total assumes that 'other soils' in NH permafrost regions overlaps with 'upland mineral soils'. All estimates have large uncertainties, but serve to illustrate the likely relative importance of different carbon stores.

large pools are found in NH high-latitude wetlands and frozen in permafrost, with the latter susceptible to release when the permafrost thaws as the climate warms.

5.3.7. Terrestrial Carbon Cycle Feedback Processes

In this section the feedback between atmospheric CO₂ concentration and the fluxes between the atmosphere and terrestrial biosphere are briefly outlined. These constitute a carbon cycle feedback rather than a climate–carbon cycle feedback, but serve as a useful starting point for the discussion of climate–carbon cycle feedbacks.

Higher atmospheric CO₂ tends to stimulate rates of photosynthesis. Early experiments involved growing seedlings in glasshouses that were maintained at different atmospheric CO₂ concentrations. Beginning in the 1990s, outdoor experiments were conducted in which elevated CO₂ concentrations were maintained over an experimental plot by continuously releasing CO₂ from storage canisters. These are referred to as *Free Air Concentration Enhancement* or *FACE* experiments, some of which (at various sites in the USA, Europe, and New Zealand) have now been carried out for more than a decade (e.g., Seiler et al., 2009; Norby et al., 2010; van Kessel et al., 2006; Rütting et al., 2010). These studies confirm that higher CO₂ stimulates increased photosynthesis and storage of carbon, but saturation of the photosynthesis response occurs at a CO₂ concentration of around 500–600 ppmv, which is much lower than expected based on leaf-level physiology (Canadell et al., 2007). In addition, carbon–nitrogen (C–N) interactions can substantially reduce the stimulation of photosynthesis due to higher atmospheric CO₂ concentration after a few years (Norby et al., 2010). More detailed information can be found in Dickinson (2012, this volume).

Higher atmospheric CO₂ has been observed to increase rates of soil respiration in various grassland ecosystems (Wan et al., 2007). This could be due to an increase in plant photosynthesis and the availability of soil carbon, or due to an increase in soil moisture due to reduced stomatal conductance, both a direct result of higher atmospheric CO₂ concentration and leading to enhanced microbial activity. Evidence that the increase in respiration is due to reduced soil moisture loss is provided by the fact that Pendall et al. (2003) report an increase in soil respiration by 25% under elevated CO₂ during the moist season (when water would be less limiting) and by 85% during the dry season in a short-grass prairie in North America. Wan et al. (2007) found that CO₂ enhancement of soil respiration is greater under elevated temperature than ambient temperature. They speculate that this may be due to warmer conditions having a greater drying effect, so that the impact

of higher CO₂ in reducing water loss and hence in stimulating respiration is greater. In experiments with tree seedlings, Tingey et al. (2006) report no effect of higher CO₂ on soil respiration, but they do find that elevated CO₂ increases the sensitivity of soil respiration to increases in temperature¹⁴.

Higher CO₂ is expected to initially increase rates of N fixation, followed by down-regulation after a few years (Hungate et al., 2004). The initial increase in N fixation is related to the fact that N fixation is energetically expensive and limited by carbon, as discussed by Dickinson (2012, this volume).

In summary, a higher atmospheric CO₂ concentration usually stimulates higher rates of photosynthesis in the short term, and may stimulate greater rates of N fixation, although both effects generally decrease over time. Higher CO₂ also sometimes increases the rate of soil respiration by increasing the soil moisture content. Warmer temperatures sometimes increase the effect of higher atmospheric pCO₂ on soil respiration and, conversely, higher atmospheric pCO₂ increases the effect of temperature on soil respiration.

5.3.8. Terrestrial Climate–Carbon Cycle Feedback Processes

Climate–carbon cycle feedbacks through the terrestrial biosphere involve changes in the rate of photosynthesis and respiration due to changes in temperature and soil moisture, in the rate of N fixation (which ultimately affects the rate of photosynthesis), in the production of CH₄ from wetlands, and in the release of CO₂ and CH₄ from thawing permafrost soils. Other potential feedbacks involve an increase in the frequency and severity of fires and insect outbreaks.

5.3.8.1. Feedbacks Involving GPP, NPP, and Foliar Respiration

Where temperatures are currently below the optimum for GPP and water and nutrients are not limiting factors, warming will increase GPP but, where temperatures are already above the optimum temperature, further warming will reduce GPP. Warmer temperatures tend to increase both autotrophic and heterotrophic respiration but, in both cases, there is a tendency for the respiration rates to decrease back towards the initial respiration rates over time – a process called *acclimation*. The degree of acclimation of foliar respiration to temperature increases varies widely between species, but can approach 100% (such that there is no increase in respiration with temperature) (Ow et al., 2010).

14. That is, Q_{10} (defined later) is larger at higher CO₂.

5.3.8.2. Increased Respiration of Soil Carbon

Warmer temperatures will tend to directly increase the rate of soil respiration by accelerating the rates of chemical reactions, and will indirectly affect respiration through changes in soil moisture and through thawing of permafrost in permafrost regions. The effect of temperature on biological processes is commonly expressed as a Q_{10} factor – the factorial increase in the rate of a process for each 10 K increase in temperature. That is, the rate of some process as a function of the warming ΔT is given by:

$$R(\Delta T) = R_o(Q_{10})^{\Delta T/10} \quad (5.17)$$

where R_o is the initial rate. Observed Q_{10} values are typically 2.0–3.0. As discussed by Davidson and Janssens (2006), the Arrhenius equation¹⁵ implies that the sensitivity of decomposition to increasing temperature will be larger the more resistant the material in question is to decomposition, and will decrease as temperature increases (a saturation effect). Many studies, reviewed by and including Craine et al. (2010), confirm that respiration rates are generally more sensitive to temperature changes the more resistant the material (and hence the lower the initial respiration rate). Accurate projection of future soil respiration rates at a given location requires correct partitioning of the soil carbon into fractions that are and are not resistant to decomposition, choosing the correct initial respiration rates, and choosing the correct temperature dependencies.

Addition of fresh carbon (from increased NPP) can provoke the decomposition of old, resistant carbon by providing readily available energy for soil microbes. This is referred to as a *priming* effect of fresh carbon on respiration of old carbon (Kuzyakov, 2002).

In many experiments in which soils are heated over a period of months or years so as to mimic the effect of global warming, soil respiration rates have been observed to initially increase, but then to decrease over time. That is, there is an *acclimation of soil respiration* to higher temperature, similar to that observed for foliar respiration. With 100% acclimation, there would be no long-term change in respiration rates in response to warmer temperatures. On the other hand, in some experiments (e.g., Malcolm et al., 2008; Dorrepaal et al., 2009; Reth et al., 2009), no acclimation has been observed after periods of 8–10 years.

Acclimation of decomposers, where observed, could be the result of: (i) a decrease in the availability of substrates; or (ii) genuine acclimation of decomposers, fungi, or roots.

In experiments by Reth et al. (2009) over a period of 8–10 years, an apparent acclimation is due to reduced availability of easily decomposed substrates in the warmed soils, rather than a genuine acclimation.

5.3.8.3. Dieback of Middle- and High-Latitude Forests

Dieback of forests could occur as a result of climatic changes (particularly decreases in precipitation) that render any forest ecosystem unviable, or as a result of climate changes that require the transition from one forest type to another, with dieback of the existing forest occurring before the new forest has established itself. As an example of the former, parts of the existing boreal forest in western Canada may revert to grassland ecosystems, whereas the existing boreal forest in eastern Canada will probably be replaced with temperate broadleaf forests (Notaro et al., 2007). The ability for the boreal forest to re-establish itself north of the existing boreal forests will in many places be limited by poor soils. Insect damage will most likely interact with the direct effects of climatic change in provoking forest dieback.

Black spruce is the dominant species in the vast boreal forest, and is exceptionally sensitive to changes in temperature. Way and Sage (2008) grew black spruce seedlings from seeds that were taken from southern Ontario (at the southern limit of the boreal forest) and placed in 3.8 litre pots that were filled with peat moss, watered as needed to maintain a moist growing medium, and fertilized weekly. Twelve days after germination, half of the seedlings were moved to a greenhouse with day/night temperatures of 30°C/24°C (HT, high temperature, corresponding to summer temperatures expected by 2100) and the other half were maintained at 22°C/16°C (LT, low temperature, representative of current summer conditions). The HT seedlings, were 20% shorter, 58% lighter, and had a 58% lower root:shoot ratio than the LT seedlings. Mortality at the end of the growing season was negligible for LT seedlings but reached 14% for HT seedlings. Net photosynthesis at growth temperature was 19%–35% lower in HT than in LT trees. Note that these impacts do not include possible effects of drought associated with warmer temperatures, as the growing medium was maintained in a moist state for both temperature treatments.

The incidence of forest fires in boreal forests is projected to increase strongly as the region warms. For example, Balshi et al. (2009) project an increase in CO₂ emissions from fires in the North American boreal forest by a factor of about 2.5–4.5 during the twenty-first century, using the TEM ecosystem model driven by climate changes from the Canadian AOCGM (CGCM2). The net effect of increasing incidence of fires (taking into account regrowth after fires) is a decrease in C storage by 2100 by about

15. The Arrhenius equation for reaction rate constant, k , as a function of activation energy, E_a , and temperature, T , is $k = Ae^{-E_a/RT}$. Here, R is the gas constant and A is the number of collisions that may or may not result in a reaction.

19 Gt. Harrison and Bartlein, (2012, this volume) review palaeo-evidence for the relationship between large-scale fires and climate change.

5.3.8.4. Amazon Ecosystem Collapse

Modelling studies indicate that the Amazon rainforest might be close to a tipping point (threshold) whereby increased occurrence and severity of drought could lead to widespread collapse of the forest, which would revert to savanna or grassland (Phillips et al., 2009; Malhi et al., 2009). Reduced growth and increased tree mortality were associated with a single severe drought in 2005, which caused the emission of 1.2–1.6 GtC (Phillips et al., 2009). Satellite data indicate a 33% increase in the extent of forest fires in 2005 compared to the 1999–2005 mean (Aragão et al., 2007). Even though we might be close to a threshold temperature change, with a strong decrease in the equilibrium forest cover with further warming, the lag in the rainforest ecosystem response is such that very little change might occur until long after the tipping point has been passed (cf. Lenton, 2012, this volume). This is illustrated in Figure 5.13, which shows the simulated variation in

Amazon forest cover over time and the dieback as a function of the global mean temperature change, along with the committed reduction in forest cover for each year, for the HadCM3LC model driven by the A2 emission scenario. According to this model, if the climate were stabilized at 2 K global mean warming by 2050, there would be very little change in Amazon forest cover at that point in time, but significant dieback would occur over the next 100–200 years.

The major source of uncertainty concerning the fate of the Amazon lies in the projected change in climate, particularly rainfall, rather than in the ecosystem models (Poulter et al., 2010).

Throughfall exclusion experiments, in which up to 60% of the rainfall is prevented from entering the soil using plastic panels that are installed beneath the understorey, indicate negligible impacts from 3–4 years of rainfall deprivation (due to the ability of deep tap roots to access deep soil moisture), but increasingly severe impacts thereafter (Nepstad et al., 2007; da Costa et al., 2010). Salazar et al. (2007) used monthly temperature and precipitation changes over the next century as projected by 15 different AOGCMs to project changes in South American biomes using the LPJ (Lund–Potsdam–Jena) dynamic global vegetation model (DGVM) (Figure 5.14)¹⁶. For the A2 emission scenario, 75% of the models project that at least 50% of the Amazon remains by the end of the century, 75% of the models show that 20% is converted to savanna, while there is no consensus on the fate of the remaining 32%. These simulations all neglect the continuing impact of human-induced land use and land-cover changes (Pitman and de Noblet-Ducoudré, 2012, this volume).

Not included in current projections of the impact of climatic change in the Amazon are likely increases in the incidence of fire, the impacts of which could be worse than those of drought stress (Barlow and Peres, 2008). Fragmentation of intact forests through the construction of roads and logging operations increases the susceptibility of forests to fire by creating dry, fire-prone forest edges, and introduces humans that can start fires (Laurance, 2000). Conversely, with limits on human encroachment and vigorous efforts to contain fires when they are started, it is possible – given the inertia of the ecosystem – that large-scale collapse could be deferred until after 2200 (Malhi et al., 2009), by which time it might have been possible to reduce GHG heating sufficiently to avoid collapse (by creating negative emissions in various ways).

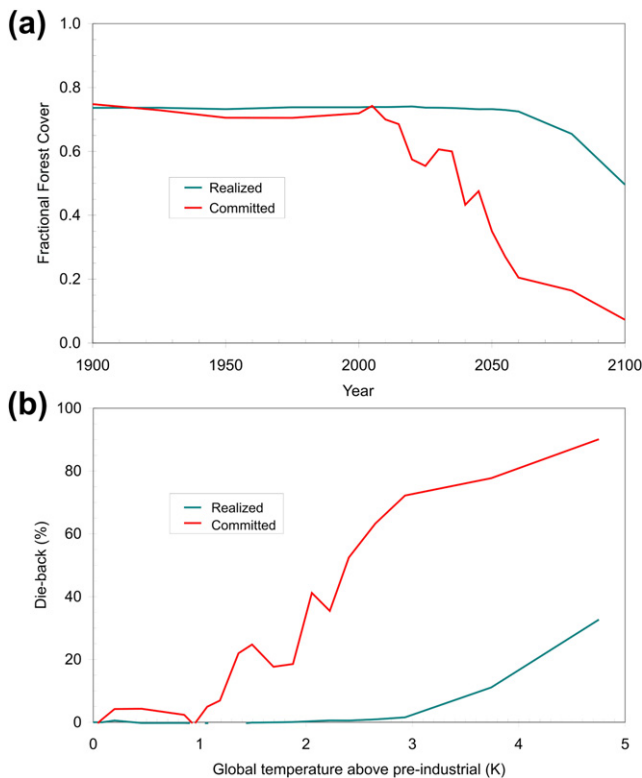


FIGURE 5.13 (a) Fractional tree cover in the current Amazon rainforest that remains as climate changes under the A2 emissions scenario according to the HadCM3LC model, and the committed state corresponding to each year. (b) The same as in (a) but plotted as the dieback as a function of the global mean warming. (Source: Jones et al., 2009. Reprinted by permission from Macmillan Publishers Ltd.)

16. A DGVM is a model that simulates the spatial distribution of different plant functional types, as well as the cycling of carbon within each plant functional type together with exchanges of energy and moisture with the atmosphere.

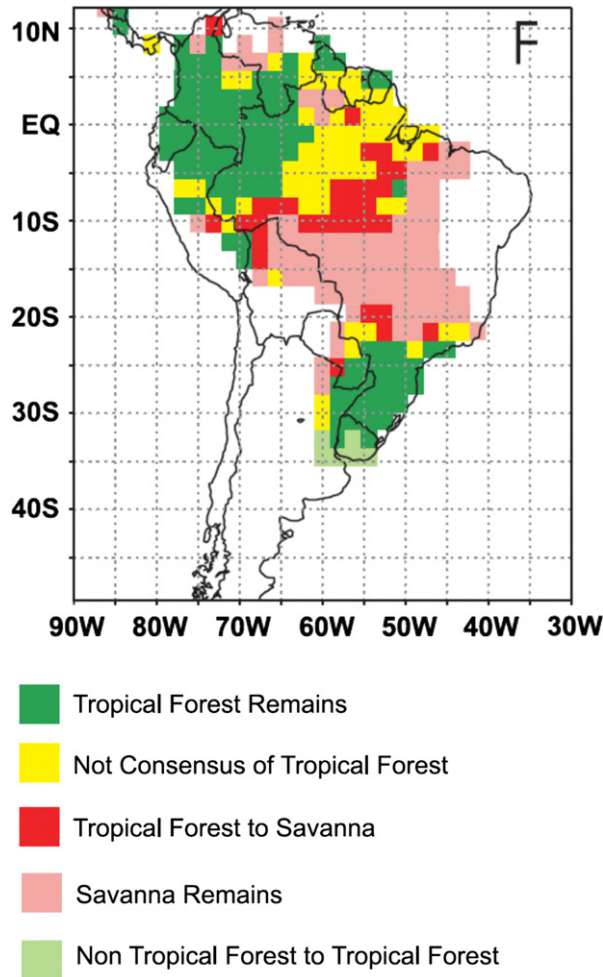


FIGURE 5.14 Fraction of 15 AOGCM climate change simulations that provoke various transitions in the type of biome at various grid cells in South America by 2100 for the A2 emissions scenario. (Source: Salazar *et al.*, 2007 © Copyright 2007 American Geophysical Union. Reproduced/modified by permission of American Geophysical Union.)

5.3.8.5. Methane Emissions from Wetlands

CH₄ is produced in wetlands through anaerobic decomposition of organic matter. The rate of production of CH₄ depends on the availability of decomposable organic matter (and so may increase as NPP increases), the water level (which determines the extent of anaerobic conditions), and temperature. Shindell *et al.* (2004) ran a detailed process-based model on a 1° × 1° (latitude–longitude) grid to calculate present-day wetland emissions of CH₄ as a function of water-table level, soil temperature, and NPP. Local correlations between monthly mean emissions and monthly mean soil temperature and moisture were then used in combination with soil temperature and moisture output from the GISS (Goddard Institute for Space Studies) AGCM to calculate CH₄ emissions for present conditions and for the climate in equilibrium with a doubling of atmospheric CO₂

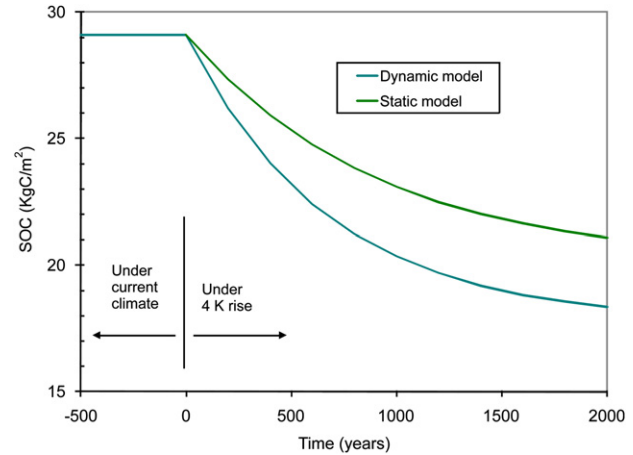


FIGURE 5.15 Simulated decrease in peatland carbon (SOC, soil organic carbon) for a site in northern Manitoba following a sudden 4 K surface warming. (Source: Ise *et al.*, 2008 © Reprinted by permission from Macmillan Publishers Ltd.)

(given a global mean warming of 3.4 K). Global wetland emissions increase by 78%, from 156 Tg per year to 277 Tg per year. Most of the increase is due to emissions from tropical wetlands, although emissions from high northern latitude wetlands nearly triple during the summer.

The feedback factor associated with the calculated increase in wetland emissions can be computed as follows: using formulae for the lifespan and radiative forcing due to CH₄ given in Harvey (2011), the steady-state CH₄ concentration assuming fixed natural and anthropogenic emissions of 185 TgC per year and 196 TgC per year, respectively, is 1860 ppbv¹⁷. The steady-state concentration with an additional CH₄ emission of 120 TgC per year is 2600 ppbv, which produces an additional radiative forcing of 0.375 W m⁻² (this accounts for the overlap with N₂O and includes an extra forcing of 0.130 W m⁻² due to extra tropospheric ozone and stratospheric water vapour). This extra forcing gives a feedback parameter λ_{wetland} of $-0.110 \text{ W m}^{-2} \text{ K}^{-1}$. This, in turn, would increase a climate sensitivity of 1.50 K to 1.57 K (a 5% enhancement) or a climate sensitivity of 4.5 K to 5.18 K (a 15% enhancement).

Ise *et al.* (2008) used a detailed process-based model of the biogeochemistry, hydrology, and temperature of a peatland in northern Manitoba to study the impact of warming. Figure 5.15 shows the change in the carbon content over time when a 4 K warming is suddenly imposed at year zero. About 63% (1/e) of the final response occurs over a period of about 350 years, with the full response to the warming perturbation requiring about 1000 years. Two cases are shown in Figure 5.15: one (static) where the soil depth is held fixed even as organic matter decays, and one

17. In transient calculations performed in the Excel spreadsheets that accompany Harvey (2011), the transient CH₄ concentration reaches 1730 ppbv by 2000, in line with observations.

(dynamic) in which it is allowed to change. In the latter case, decreasing the soil depth reduces the water-holding capacity, which provokes further drying and loss of carbon. The inherent temperature sensitivity of respiration in the model is a Q_{10} of 2.0, but the effective Q_{10} (taking into account losses due to drier conditions) is 2.5 for the static model and 3.6 for the dynamic model.

5.3.8.6. Feedbacks Involving Permafrost Soils

Simulations of climate change using an AOGCM indicate that the majority of the world's permafrost could be lost this century under business-as-usual emission scenarios: the global extent of permafrost (excluding Greenland and Antarctica) decreases from around 10 million km² in 2000 to about 4 million km² in 2100 under the B1 emission scenario and to about 1 million km² under the A2 emission scenario (Lawrence and Slater, 2005) (see also Lenton, 2012, this volume). Permafrost regions are estimated to contain in excess of 1600 GtC (Table 5.2), much of which could potentially be released to the atmosphere once the permafrost thaws.

Of particular concern are the organic-rich soils in Siberia — known as *yedoma* in the Russian literature and as loess in the English-language literature — which contain carbon that accumulated during the glacial periods of the Pleistocene and which decomposes quickly when the soils are thawed. Khvorostyanov et al. (2008a) used a detailed permafrost model to simulate the impact of local warming on yedoma soils to a depth of 12 m. They estimate that intense mobilization of carbon would begin when the regional warming reaches about 9 K and continue for several hundred years. Based on an estimated initial total carbon stock for the yedoma region of 375 Gt and using the regionally-averaged soil temperature, they find:

- Assuming normal hydrological conditions, the soil carbon stock decreases to about 340 Gt by the time the warming reaches 9 K, then drops to 130 GtC over the next 100 years (an average loss of 2.1 GtC per year) and to 60 GtC over the following 100 years (an average loss of 0.7 GtC per year), with 12% of the total lost carbon (about 40 Gt) emitted as CH₄.
- Assuming the upper metre of the soil to be always saturated, the soil carbon stock decreases to about 360 Gt by the time the warming reaches 9 K, then drops to 180 GtC over the next 100 years (an average loss of 1.8 GtC per year) and to 140 GtC over the following 100 years (an average loss of 0.4 GtC per year), with all of the lost carbon emitted as CH₄¹⁸.

Inasmuch as the mean annual warming over land at the latitudes (60°N to 70°N) where yedoma soils occur is about

twice the global mean warming (see figure 10.6 of Meehl et al., 2007), this implies that significant carbon release would occur in association with a global mean warming of about 4.5 K. Mobilization and release of soil carbon begins with much less warming, but is initially quite slow. Intense carbon release is triggered by internal heat generation by decomposers, and is irreversible once it starts (see also Lenton, 2012, this volume).

Thaw lakes are another source of CH₄ from permafrost regions. They are produced when the water along the edges of the lakes causes massive subsurface ice wedges to melt, in turn causing the ground surface to subside in a self-perpetuating cycle (this is referred to as thermokarst erosion). Walter et al. (2006) conclude that the CH₄ flux from the lakes in their study region in Siberia is 5 times greater than previously estimated, and increased by about 60% between 1974 and 2000.

Schaefer et al. (2011) used a detailed 1D permafrost model, placed at each grid point in a global grid covering permafrost regions, to estimate the potential CO₂ fluxes associated with the A1B emission scenario. They simulate cumulative emissions of 70–140 GtC by 2100 (0.7–1.4 GtC per year) and 150–250 GtC by 2200. These are global emissions, but are based on only the top 3 m of permafrost soils and do not account for the positive feedback on C release through internal heat generation by the decomposition process nor for releases from regions with discontinuous permafrost or from thaw lakes. Khvorostyanov et al. (2008a,b) simulate a larger flux (1.8–2.1 GtC per year averaged over the first 100 years of active release) from only one (admittedly carbon intense) region, but the vast majority of the C released in their simulations is from below the 3 m depth (see their Figure 5.4c). Given the estimated size of the yedoma soil C pool and widespread observations (summarized by Schaefer et al., 2011) of warming by 1–3 K at depths of 10–20 m over that past few decades, the large fluxes simulated by Khvorostyanov et al. (2008a,b) are plausible.

5.3.8.7. Summary

There is the potential for large positive feedbacks between the climate and the terrestrial part of the carbon cycle. Warmer conditions will tend to increase GPP and soil respiration, although the former might be limited by lack of moisture or nutrients, or reversed when temperatures exceed optimal conditions, while decreasing availability of easily respirable soil carbon will limit the long-term increase in soil respiration. However, significant dieback of mid-latitude and tropical forests could occur, with large transient emissions of CO₂. Increased CH₄ emissions from wetlands could increase climate sensitivity by 5%–15%. The largest potential fluxes involve release of carbon from thawing permafrost, much of which could be in the form of CH₄.

18. By comparison, the fossil fuel CO₂ emission in 2007 was 8.0 GtC (Boden and Marland, 2010).

5.3.9. Terrestrial Climate—Carbon Cycle Feedback: Local and Large-Scale Observations

The previous section summarized laboratory and field experiments and modelling studies. In this section, observations concerning recent changes in photosynthesis, NPP, drought, fires, and insect outbreaks in natural ecosystems and their links to recent changes in climate or climate variability are summarized. The feedback between climate and the terrestrial component of the carbon cycle is likely to have been negative up to the present; that is, changes in climate so far have probably stimulated net absorption of CO₂ from the atmosphere by the terrestrial biosphere. However, there is evidence of an emerging positive feedback consistent with the expectations that were reviewed in the previous section.

5.3.9.1. Trends in Photosynthesis and Net Primary Productivity

The global rate of photosynthesis and global net biome productivity have clearly increased over the past half century or more. This is evident from satellite and ground-based data, as reviewed by Boisvenue and Running (2006), from the need for a terrestrial biosphere sink in order to account for all of the CO₂ emitted by humans (Bopp et al., 2002), from vertical CO₂ profiles (Stephens et al., 2007), and from inversion modelling (Gurney et al., 2008).

However, in spite of the overall stimulation of photosynthesis, there is observational evidence that the trend may slow down or even reverse:

- Model analysis of the satellite-based observed greening north of 25°N over the period 1980–2000 indicates that increasing atmospheric CO₂, temperature, and precipitation accounted for 49%, 31%, and 13% of the greening, but that the greening trend will weaken or disappear with continued warming (Piao et al., 2006)¹⁹.
- More recent satellite observations indicate a reversal or at least a stabilization of the upward trend between 2000–2009, due largely to decreasing NPP in the SH that is linked to a widespread SH drying trend (Zhao and Running, 2010).
- Carnicer et al. (2011) report a doubling in the percentage of tree crown defoliation (from about 12% to 25%) in southern Europe over the period 1990–2007 in parallel with increasing mean annual temperatures and decreasing rainfall.
- Based on detailed repeated censuses between 1981 and 2005 on 50-ha forest plots in Panama and Malaysia (where pronounced warming has occurred), Feeley et al.

(2007) report that stem growth rates within distinct size categories decreased over time (with community level rates of decrease in stem growth of 1.2% per year in the Panamanian plots and 6.2% per year in the Malaysian plots).

- The warm and dry climate of the early 1980s in Alaska caused the Arctic tundra there to switch from a carbon sink to a carbon source. During the 1990s, summer sink activity resumed, indicating a previously undemonstrated capacity of this ecosystem to acclimatize to decadal (and longer) warming (Oechel et al., 2000). However, the tundra ecosystem studied is still a net source of CO₂ to the atmosphere on an annual basis due to winter release of CO₂.
- In a large (>1500) sample of white spruce trees in Alaska, over 40% displayed decreased growth with warmer temperatures over the last few decades and less than 40% displayed increased growth, the differences being due to differences in water stress at different sites (Juday et al., 2005).
- A divergence of populations, which used to vary in unison prior to the twentieth century, similar to that noted above for Alaska, has also been observed in the Mackenzie delta and other subarctic locations (Pisaric et al., 2007).

5.3.9.2. Response of NPP to Inter-annual Variability

The extreme heatwave in Europe in the summer of 2003 led to a strong reduction in both photosynthesis and respiration due to drought stress, with a net source of 0.5 GtC that year (Ciais et al., 2005; Reichstein et al., 2007). Conversely, there was an exceptional uptake of CO₂ at six monitored forest sites in Europe (spanning 44°N to 62°N) in the spring of 2007 in response to an exceptionally warm spring. However, as discussed by Delpierre et al. (2009), when a warm spring is followed by a summer drought, the two effects cancel each other out, but if the warm spring hastens the drought (through the earlier resumption of transpiration after the winter), there would be a tendency towards net carbon release. Warmer and drier conditions in the tropics during recent El Niño events are calculated to have suppressed NPP by 1.21 GtC per year and enhanced heterotrophic respiration by 0.56 GtC per year (Qian et al., 2008).

5.3.9.3. Tree Mortality and Insect Outbreaks

Allen et al. (2010) present tables summarizing 88 instances of drought and heat-induced tree mortality that have been reported in the scientific literature during the last two decades or so. The portion of the literature with the keyword ‘forest’ that also has the keywords ‘forests

19. Land-use change, N deposition, and ozone were not included in the analysis.

AND mortality AND drought' increased from 0.1% in the mid-1980s to 0.3% by 2008–2009, although this may not be indicative of a real trend in tree mortality. Rates of tree mortality in old forests across a broad region of the western USA have doubled to tripled during the past four decades, while the rate of establishment of new trees has increased by only about 50% (van Mantgem et al., 2009). This has been accompanied by warming at rates of 0.3–0.5 K per decade at the elevational range of the forests, which caused an increase in summer drought.

Widespread losses in forests have occurred in recent years due to insect outbreaks that are related at least in part to warmer temperatures. Examples include:

- Mountain pine beetle outbreaks in western Canada, killing millions of trees over an area of 130,000 km² in 6 years, including areas at higher elevations and more northern latitudes than in the past (Kurz et al., 2008)
- Drought and insect-driven mortality affecting 12,000 km² of piñon pine, killing 40%–97% of trees at some sites in less than 3 years (Breshears et al., 2005; McDowell et al., 2008)
- Other insect outbreaks from Mexico to Alaska (Raffa et al., 2008)

More frequent outbreaks of insects are expected in tropical forests under warmer and drier conditions (Coley, 1998). Boreal forests are observed to be more susceptible to insect pests than other forests, perhaps because of their low genetic diversity.

5.3.9.4. Increased Incidence and Severity of Forest Fires

Temperature variations have been a driving factor behind variations in the area of forest burning per decade over the past century. In Canada, both temperature and area burned decreased modestly from 1920 to 1970, then increased sharply from 1970 to 2000, while, in Alaska, decadal burned area decreased from the 1940s to the 1980s, then rose to over 150% that of the 1940s by the 2000s. Gillett et al. (2004) examined the statistical relationship between forest area burned (in 5-year blocks) and temperature in Canada since 1920 and found that temperature variations can explain 59% of the variation in five-year totals. Kasischke et al. (2010) find temperature and precipitation variations to be the main factor behind Alaskan trends, although a decrease in fire suppression activities in the 1990s and 2000s was a contributing factor to the recent increase in decadal burn area.

Figure 5.16 shows data on the variation in forest fire extent or frequency during the past few decades in selected regions. The area of forest burned per decade increased by a factor of 4 in Canada and Alaska combined from the

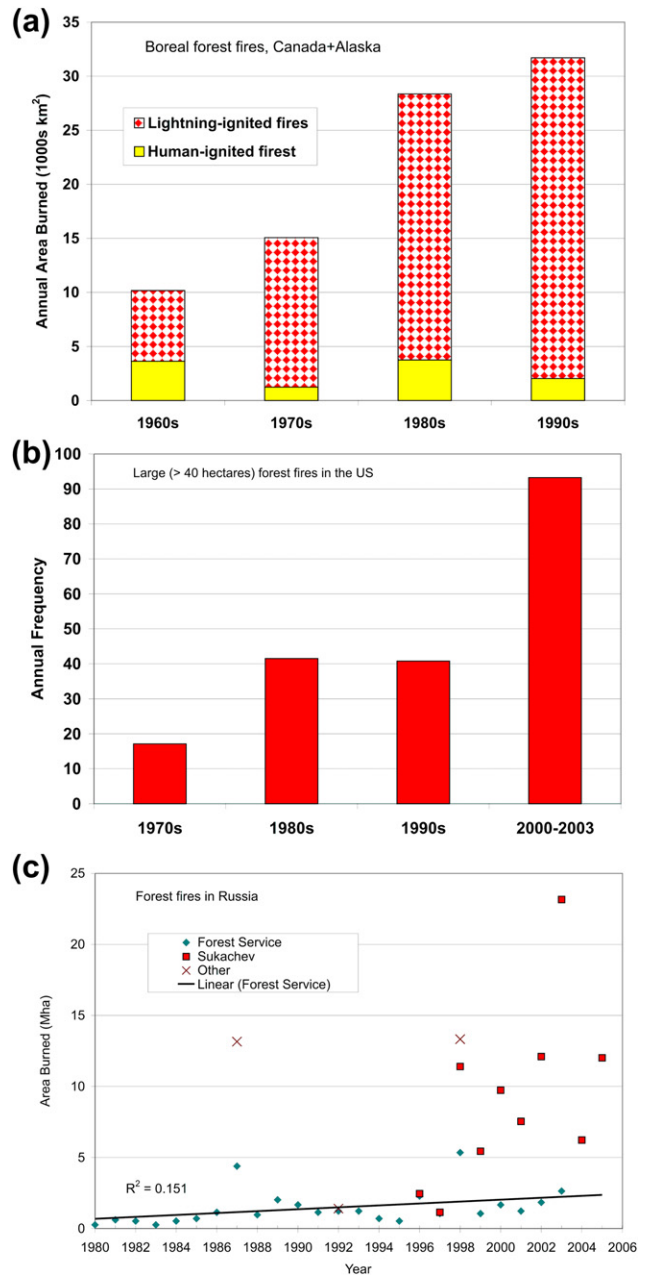


FIGURE 5.16 Trends in: (a) the area of boreal forest burned annually in Canada + Alaska; (b) in the annual frequency of large (>40 ha) forest fires in the lower 48 US states; and (c) the annual area of forest burned in Russia. (Sources: (a) Data from Kasischke and Turetsky, 2006; (b) data from Westerling et al., 2006; and (c) Soja et al., 2007. Reprinted from Soja et al., 2007; with permission from Elsevier)

1960s to the 1990s (Stocks et al., 2003; Kasischke and Turetsky, 2006), while the number of large (>400 ha) fires per year in the lower 48 states of the USA increased by more than a factor of 6 after the 1980s (Running, 2006; Westerling et al., 2006). There has also been a dramatic increase in recent years in the frequency and severity of fires in Russia (Soja et al., 2007).

5.3.9.5. Fires in Peatlands

Turetsky et al. (2002) crudely estimate that there has been a 2.5-fold increase in the annual area of peatlands burning in Canada in recent decades compared to the long-term average since the last glaciation. In Indonesia, peat fires triggered by dry conditions associated with a strong El Niño released 0.4–2.2 GtC in 1997 (Page et al., 2002). An increase in lightning strikes could also increase the incidence of fire. The frequency of lightning strikes on the tundra of the North Slope in Alaska has apparently increased by a factor of 10 in the last 10 years and, of 26 recorded fires since 1950, close to one third took place over the 3 years preceding 2009 (Qui, 2009). Based on the record of varying charcoal abundance in lake sediments, Hu et al. (2010) conclude that the large fires in 2007 in central Alaska were unprecedented within the last 5000 years (and see also Harrison and Bartlein, 2012, this volume).

5.3.9.6. Empirical Estimate of the Global-Scale Climate–Soil Carbon Feedback

Given estimates of anthropogenic CO₂ emissions during the past century (the only significant uncertainty pertaining to land-use emissions; see Pitman and de Noblet-Ducoudré, 2012, this volume) and observed yearly CO₂ concentrations, the CO₂ airborne fraction (defined as the annual mass increase in atmospheric CO₂ divided by the annual emission) can be computed and compared with what would be expected from a carbon cycle model with no climate–carbon cycle feedback. Rafelski et al. (2009) did just this, using a model with separate fast and slow soil carbon pools. The rate of growth of fossil fuel emissions fell from 4.3% per year before 1980 to 1.5% per year after 1980, which should have caused a decrease in the airborne fraction. Instead, the airborne fraction has been nearly constant since 1958. For a wide variety of assumptions concerning land-use emissions and N fertilization, Rafelski et al. (2009) find that this can be explained by a warming-related increase in natural CO₂ emissions that can be obtained assuming a Q_{10} for respiration of fast soil carbon of 1.5–5.0 (depending on assumptions concerning land use emissions, N fertilization, and oceanic CO₂ uptake)²⁰.

5.3.9.7. Summary

There is widespread evidence that the terrestrial biosphere sink is beginning to weaken in regions where warmer temperatures and/or reduced rainfall have led to drought

stress. Growth rates have slowed in water-stressed northern boreal sites and in some tropical forest sites, and there is an increasing incidence of crown defoliation, insect outbreaks related to heat and drought, forest dieback, and forest and peatland fires. The combination of a slowing in the rate of growth of anthropogenic emissions after 1980, combined with a near-constant airborne fraction indicate that the overall effect of warmer temperatures has been to cause a net emission of CO₂ from the terrestrial biosphere.

5.3.10. Destabilization of Methane Clathrate

CH₄ clathrate (or CH₄ hydrate) is an ice-like compound formed when water freezes in the presence of sufficient CH₄ and other gases, such that these gases become trapped within the water molecule lattice. The temperature and pressure combinations found at the sea floor are such that CH₄ clathrate is stable there, although the sediment temperature increases with depth, such that below a certain depth any clathrate would melt. The amount of CH₄ in clathrate at a given location depends on the thickness of the stability zone, the sediment porosity and the fraction of the pore space occupied by clathrate. The possible origins, geology, properties, past destabilization events, and other characteristics of CH₄ clathrate are reviewed in Archer (2007).

Estimates of the global inventory of CH₄ in clathrates range from 700 to over 10,000 GtC. As the ocean seafloor warms in response to the warming climate, heat will diffuse into the sea floor, raising temperatures and destabilizing clathrates from the bottom of the stability zone upward (Harvey and Huang, 1995). Upwardly migrating CH₄ could reform clathrates within the overlying stability zone and, once this zone becomes impermeable or if it is already impermeable, gas would build up below the stability zone. Thawing of clathrates at the base of the stability zone would initially be slow and would continue for centuries. However, if pressure builds up between the thinning stability zone, a point may be reached where large amounts of CH₄ are released abruptly due to fracturing of the overlying clathrate layer, or due to sliding of sloping sediments. Nevertheless, due to the fact that the warming would need to penetrate to the base of the stable zone before thawing of CH₄ clathrates would begin, and that the released CH₄ would then re-enter the stable zone, Harvey and Huang (1995) concluded that destabilization of CH₄ clathrates would not significantly enhance the global mean warming until several centuries into the future, and that significant effects on climate would occur only if the global mean warming had already reached 3–5 K.

More recently, Archer et al. (2009) estimated that a warming of 3 K would be sufficient to eventually

20. A $Q_{10} > 1.0$ for the slow soil carbon reservoir is likely but cannot be determined by this analysis because of the much smaller respiration flux (and correspondingly, the much longer turnover time) for the slow carbon reservoir.

release half of the CH₄ in marine clathrates. The major unknown is the fraction of CH₄ that would escape to the atmosphere; much of it could be oxidized to CO₂ in the water column before reaching the atmosphere if it is released slowly enough. Archer et al. (2009) estimate the releasable CH₄ from a 3 K global mean warming to be 35–940 GtC, released over a period of several thousand years. The effect of CH₄ clathrates in this case would be to slow the decline of atmospheric CO₂ from its peak, rather than causing a larger peak concentration. However, Reagan and Moridis (2007) conclude that, although deep hydrate deposits are resistant to rapid destabilization, shallow deposits, such as those found in Arctic regions and in the Gulf of Mexico, can rapidly dissociate, producing significant fluxes within the next 100 years in response to a seafloor warming of 3 K over the next 100 years.

Indeed, destabilization of shallow marine clathrates may have already started on the continental slope west of Spitsbergen, where sediments apparently warmed by 3 K over the past century (Reagan and Moridis, 2009). Westbrook et al. (2009) report observations of more than 250 plumes of gas bubbles emanating from the seabed of the West Spitsbergen continental margin. While at least some of this is from natural seepage of pre-existing CH₄, not from dissociation of CH₄ clathrate, some is due to dissociation. Low-level (~8 TgC per year) release of CH₄ from sediments to the atmosphere is occurring from the East Siberian Arctic shelf²¹, but it is unknown whether this is entirely a natural background flux or partly the beginning of temperature-induced CH₄ release (Shakhova et al., 2010a,b). The total of all natural emissions from various geological sources (including clathrates) is estimated to be about 35 TgC per year (Kvenvolden and Rogers, 2005), which would have contributed to the background (prehuman) atmospheric CH₄ concentration.

Release of CH₄ from clathrates is suspected of being a major factor in several dramatic warmings in the geological past, including at the transition between the Palaeocene and Eocene time periods – the so-called Palaeocene–Eocene Thermal Maximum (PETM; see Belcher and Mander, 2012, this volume) – at 55 Ma (Sluijs et al., 2007), during the mid-Jurassic at 183 Ma, (Hesselbo et al., 2000) and a massive release at 635 Ma that may have ended the last ‘snowball Earth’ period (Kennedy et al., 2008). Periodic minor and occasional large CH₄ releases are thought to have occurred during warm periods that interspersed glaciations during the last two million years (Kennett et al., 2000). Evidence from the PETM indicates that the

suspected release of CH₄ was preceded by a slow warming that reached 5 K in what is now Wyoming (Secord et al., 2010).

5.4. COUPLED CLIMATE–CARBON CYCLE MODEL RESULTS AND LINEAR FEEDBACK ANALYSIS

In Section 5.2.1, a linear feedback analysis was presented of climate sensitivity, showing how to quantify the inherent strength of individual feedback processes. A key conclusion was that the impact on climate sensitivity of adding a given feedback process depends on the strength of the pre-existing feedback processes. We now extend this analysis to incorporate carbon cycle processes, following closely the presentation in Gregory et al. (2009). The incorporation of climate–carbon cycle feedback in the analysis presented below, however, pertains only to feedbacks that vary in proportion to the change in global mean temperature. Thus, non-linear responses such as an abrupt increase in the emissions of CH₄ from thawing permafrost or clathrates are not included.

5.4.1. Effect of the Oceans in Limiting the Transient Temperature Response

As the climate warms in response to a positive radiative forcing, the emission of infrared radiation to space increases, serving as a break on subsequent warming. During the initial part of the transient response, a net heat flux to the deep ocean arises that also serves as a break on subsequent surface warming. In the equilibrium climate state that is reached many centuries after the radiative forcing has been stabilized, the net heat flux to the ocean will be zero because the deep ocean will have finished warming. However, during the early period of rapidly and continuously increasing radiative forcing, minimal deep ocean warming will have occurred, so the heat flux F_D to the deep ocean will be approximately proportional to the surface warming. Due to the very small heat capacity of the atmosphere and minimal heat flow into the land surface (because of the small thermal conductivity of the subsurface), the net radiation N is almost exactly equal to the net heat flux into the deep ocean. Thus:

$$N \approx F_D \approx \kappa \Delta T \quad (5.18)$$

where κ is a proportionality constant (equivalent to a damping coefficient) that applies only during a period of steadily increasing ΔT . From Equations (5.15) and (5.18) it follows that the transient temperature change is:

$$\Delta T(t) \approx \frac{\Delta R(t)}{\lambda + \kappa} = \frac{\Delta R(t)}{\rho} \quad (5.19)$$

21. By comparison, the total (natural + anthropogenic) CH₄ emission over the period 2000–2004 is estimated to have been 582 TgC per year (Denman et al., 2007).

TABLE 5.3 Radiative Feedback Parameter (λ) and Ocean Heat Flux Parameter (κ) for 19 AOGCMs as Deduced by Gregory and Forster (2008), the Sum of the Two (ρ), and the Ratio $\lambda/(\lambda + \kappa)$

Model	λ	κ	ρ	$\lambda/(\lambda + \kappa)$
CCSM3	1.84	0.67	2.51	0.73
CGCM3.1(T47)	1.28	0.55	1.83	0.70
CNRM-CM3	1.6	0.58	2.18	0.73
CSIRO-Mk3.0	1.6	0.83	2.43	0.66
ECHAM/MPI-OM	1.01	0.66	1.67	0.60
GFDL-CM2.0	1.96	0.64	2.6	0.75
GFDL-CM2.1	1.74	0.73	2.47	0.70
GISS-EH	1.46	0.77	2.23	0.65
INM-CM3.0	1.77	0.48	2.25	0.79
IPSL-CM4	1.03	0.7	1.73	0.60
MIROC3.2(hires)	0.87	0.56	1.43	0.61
MIROC3.2(medres)	0.97	0.81	1.78	0.54
MRI-CGCM2.3.2	1.23	0.41	1.64	0.75
PCM	2.08	0.45	2.53	0.82
UKMO-HadCM3	1.09	0.53	1.62	0.67
UKMO-HadGEM1	1.27	0.56	1.83	0.69
Ensemble	1.4 ± 0.6	0.6 ± 0.2	2.0 ± 0.7	0.70

The ensemble uncertainties are the 5%–95% probability range assuming that the model results are normally distributed. Units for λ , κ , and ρ : $\text{W m}^{-2} \text{K}^{-1}$

where $\rho = \lambda + \kappa$. Thus, the effect of mixing of heat into the oceans in delaying the temperature response to radiative forcing can be represented in two ways: either through incorporation of $N(T)$ into Equation (5.15) or through the incorporation of κ in Equation (5.19).

Table 5.3 gives values of λ and κ as deduced by Gregory and Forster (2008) for 19 AOGCMs that were forced with a scenario of CO_2 increasing by 1% per year for 70 years, where λ was estimated from a regression of $\Delta R - N(T)$ against ΔT and κ was estimated from a regression of $N(T)$ against ΔT . Their results are plotted in Figure 5.17. The ratio of the realized change in global mean temperature to the equilibrium change (for which $\kappa = 0$) is equal to $\lambda/(\lambda + \kappa)$, and this ratio is given for each model as the final column of Table 5.3. On average, the global mean temperature at the end of 70 years of a 1% per year CO_2 increase is equal to 70% of the response that would occur with the same radiative forcing in the absence of the deep ocean, with most models giving a response of 60%–75% of the equilibrium response. However, by reducing the transient temperature response, the oceans also reduce the effect of the climate–carbon cycle feedback, so that (as illustrated later) the impact of the oceans in limiting

transient warming is much greater than implied by the $\lambda/(\lambda + \kappa)$ ratio when the net climate–carbon cycle feedback is strongly positive.

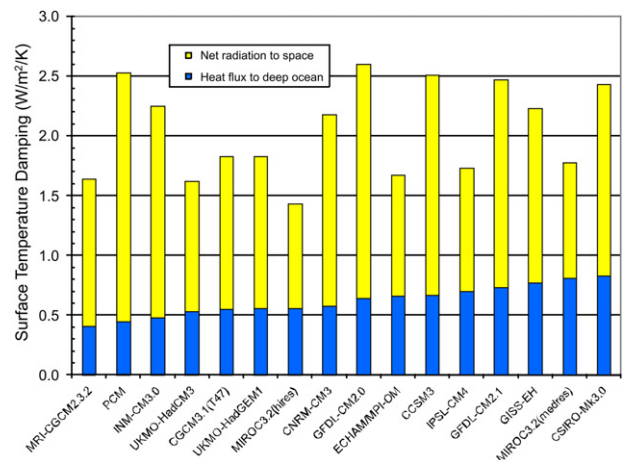


FIGURE 5.17 Overall radiative and ocean heat flux damping parameters, λ and κ , as deduced by Gregory and Forster (2008) for 19 AOGCMs. (Source: Copyright 2008 American Geophysical Union. Reproduced/modified by permission of American Geophysical Union.)

5.4.2. Climatic Change As a Feedback on the Carbon Cycle

The cumulative CO₂ emission, C_E , can be written as the sum of the CO₂ that resides in the atmosphere (C_A) and is taken up by the land (C_L) and oceans (C_O). That is:

$$C_E = C_A + C_L + C_O \quad (5.20)$$

The uptake of carbon by the land and ocean can be broken down into components that depend on the increase in atmospheric CO₂ and those that depend on the change in temperature. Thus, $C_L = C_{L\beta} + C_{L\gamma}$ and $C_O = C_{O\beta} + C_{O\gamma}$, where the subscripts β and γ denote these two components. Combining the terrestrial and marine portions, we can write:

$$C_E = C_A + C_\beta + C_\gamma \quad (5.21)$$

where $C_\beta = C_{L\beta} + C_{O\beta}$ and $C_\gamma = C_{L\gamma} + C_{O\gamma}$. Higher atmospheric CO₂ stimulates uptake by the land and oceans. Thus, $C_\beta > 0$, while warming stimulates release of CO₂, so that $C_\gamma < 0$, but $C_\beta + C_\gamma > 0$, so that $C_A < C_E$. Following Gregory et al. (2009) and Friedlingstein et al. (2006), we assume that C_β is proportional to the atmospheric CO₂ increase and that C_γ is proportional to the change in global mean surface air temperature, and that the adjustments in $C_\beta + C_\gamma$ to changing C_A and ΔT are instantaneous. That is, $C_\beta = \beta C_A$ and $C_\gamma = \gamma \Delta T$, where β is dimensionless (GtC uptake per GtC atmospheric CO₂ increase) and γ has units of GtC K⁻¹ ($\beta > 0$ and $\gamma < 0$). Then:

$$C_E = C_A + \beta C_A + \gamma \Delta T \quad (5.22)$$

$\gamma < 0$ means that carbon is released from the land-plus-oceans as the climate warms, which (intuitively and according to Equation 5.22), requires a larger C_A for a given C_E . The radiative forcing can be written as the sum of components due to CO₂ (R_C) and due to all other forcings together (R_N), so from Equation (5.19), we obtain:

$$R_C(C_A) + R_N = \rho \Delta T \quad (5.23)$$

From Equations (5.22) and (5.23):

$$R_C(C_A) + R_N = \rho \frac{C_E - (1 + \beta)C_A}{\gamma} \quad (5.24)$$

R_C varies with the logarithm of CO₂ concentration according to:

$$R_C(C_A) = F_{2x} \frac{\ln[(C_1 + C_A)/C_1]}{\ln 2} \approx \phi C_A \quad (5.25)$$

where F_{2x} is the forcing for a CO₂ doubling, C_1 is the pre-industrial CO₂ concentration, and ϕ is the average forcing (W m⁻² (GtC)⁻¹). From Equations (5.24) and (5.25), and neglecting R_N , it follows that:

$$C_E = C_A \left(1 + \beta + \frac{\phi \gamma}{\rho} \right) = C_A (1 + \beta + u_\gamma) = u C_A \quad (5.26)$$

where $u_\gamma = \phi \gamma / \rho$. As discussed by Gregory et al. (2009), Equation (5.26) is analogous to Equation (5.4) in the form:

$$\Delta R = \Delta T (\lambda_o + \lambda_{wv} + \lambda_{lr} + \lambda_c + \lambda_a) = \lambda \Delta T \quad (5.27)$$

In Equation (5.26), C_E is the forcing, C_A is the response, and u is a carbon cycle response parameter that is analogous to the climate feedback parameter λ . It is the sum of contributions related to increasing storage in the atmosphere ($u_o = 1$), a concentration–carbon cycle feedback parameter β , and a climate–carbon cycle feedback parameter u_γ . Negative contributions to λ constitute a positive feedback since they result in a larger ΔT being required to balance ΔR , and, similarly, a negative contribution to u (namely, u_γ) constitutes a positive feedback. Equations (5.4), (5.26), and (5.27) are resistance representations of the temperature or carbon cycle response, in that the components of λ and u add linearly but the larger the total λ or u , the smaller the response.

An expression analogous to the gain representation of the temperature response (Equation 5.13) can be derived for the carbon cycle response. A commonly considered quantity is the cumulative airborne fraction, A , which is the fraction of cumulative emission that resides in the atmosphere at any given time, that is, C_A/C_E . From Equation (5.26):

$$A = \frac{C_A}{C_E} = \frac{1}{1 + \beta + u_\gamma} \quad (5.28)$$

If there is no concentration–carbon cycle or climate–carbon cycle feedback, then $A = A_o = 1$ and $C_A = C_E$. By analogy to Equation (5.13), we can write:

$$C_A = A C_E = \left(\frac{A_o}{1 - f_c} \right) C_E = \left(\frac{1}{1 - f_c} \right) C_E \quad (5.29)$$

where $f_c = -\beta - u_\gamma$. When $f_c = 0$, $C_A = A_o C_E$, in the same way that when $f_\lambda = 0$, $\Delta T = G_o \Delta R$.

The upper portion of Table 5.4 gives separate land and ocean β and γ values as determined by Friedlingstein et al. (2006) from transient simulations with 11 coupled climate–carbon cycle models that were involved in the initial *Coupled Climate Carbon Cycle Model Intercomparison Project* (C4MIP). The β and γ values are applicable to the A2 emissions scenario in the year 2100. For this scenario and timeframe, β_L is on average about 20% larger than β_O (that is, the terrestrial biosphere takes up 20% more CO₂ than the oceans). On the other hand, γ_L is over twice γ_O , meaning that over two-thirds of the positive climate–carbon cycle feedback involves the terrestrial biosphere. For both carbon-cycle and climate–carbon cycle feedbacks, the uncertainty (as represented by the standard deviations of the model β and γ values) is over twice as large for the terrestrial as for the oceanic component of the carbon cycle. The impact of increased emissions of CH₄ is

TABLE 5.4 Land, Ocean, and Overall Carbon Cycle Feedback Parameters (β , GtC/GtC) and Climate–Carbon Cycle Feedback Parameters (γ , GtC K⁻¹) Based on the Response by 2100 of 11 Coupled Climate–Carbon Cycle Models to the A2 Emissions Scenario without C–N Coupling (First 11 Data Rows) and of 3 Models with C–N Coupling (Lower)

Model	Land-Surface Biosphere Scheme	Feedback Parameters					
		β_L	β_O	β	γ_L	γ_O	γ
Terrestrial biosphere modules without C–N coupling							
HadCM3LC	TRIFFID	0.61	0.37	0.99	–177	–24	–201
IPSL-CM2C	SLAVE	0.75	0.75	1.50	–98	–30	–128
IPSL-CM4-LOOP	ORCHIDEE	0.61	0.51	1.13	–20	–16	–36
CSM-1	CASA	0.51	0.42	0.94	–23	–17	–40
MPI	JSBACH	0.66	0.51	1.17	–65	–22	–87
LLNL	IBIS	1.31	0.42	1.74	–70	–14	–84
FRCGC	Sim-CYCLE	0.56	0.56	1.13	–112	–46	–158
UMD	VEGAS	0.09	0.70	0.80	–40	–67	–107
UVic-2.7	TRIFFID	0.56	0.51	1.08	–98	–43	–141
CLIMBER	LPJ	0.51	0.42	0.94	–57	–22	–79
BERN-CC	LPJ	0.75	0.61	1.36	–105	–39	–144
Mean		0.63	0.53	1.16	–79	–31	–110
Standard deviation		0.29	0.12	0.27	46	16	51
Terrestrial biosphere modules with C–N coupling							
MIT-IGSM2.3	TEM	0.26	0.63	0.89	13	–14	–1
CCSM3.0	CLM3-CN	0.19	0.38	0.56	20	–10	10
IPSL-CM4-LOOP	ORCHIDEE	0.30	0.51	0.81	–51	–16	–67
Mean		0.25	0.50	0.75	–6	–13	–19
Standard deviation		0.05	0.13	0.17	39	3	42

(Source: Friedlingstein et al., 2006 except for MIT-IGSM2.3 (from Plattner et al., 2008), CCSM3.0 (from Thornton et al., 2009) and second IPSL-CM4-LOOP line (from Zaehle et al., 2010). Definitions of model and land-surface scheme acronyms and original references are given in Friedlingstein et al., 2006.)

not included in this analysis, but would have the effect of increasing γ_L . At the end of a period of increasing emissions, the value of β should be smaller the greater the cumulative emission due to partial saturation of the terrestrial and oceanic CO₂ sinks but, once CO₂ emissions cease, β_O and the overall β will increase over time as more CO₂ is taken up by the deep ocean²². The first expectation has been confirmed by Plattner et al. (2008) for the BERN model, for which both β_L and β_O in 2100 are about 40% smaller for the A2 emissions scenario (2000 GtC cumulative CO₂ emission to 2100) than for the B1 emissions scenario (1200 GtC cumulative emissions).

22. Recall that $\beta = (\text{uptake by the biosphere and oceans})/(\text{atmospheric increase, } C_A)$, so as $C_A \rightarrow 0$, $\beta \rightarrow \infty$.

5.4.3. The Carbon Cycle As a Climate Feedback

The preceding analysis presented climatic change as a feedback on the carbon cycle by eliminating ΔT from Equations (5.22) and (5.23), with C_E the forcing and C_A the response. Alternatively, we can eliminate C_A . From Equations (5.22), (5.23), and (5.25), we get:

$$\begin{aligned} R_C(C_E) &= \phi C_E = \phi(C_A + \beta C_A + \gamma \Delta T) \\ &= \rho \Delta T(1 + \beta) + \phi \gamma \Delta T \end{aligned} \quad (5.30)$$

or

$$\phi C_E = \Delta T(\rho + r_\beta + r_\gamma) \quad (5.31)$$

TABLE 5.5 Climate, Carbon Cycle, and Climate–Carbon Cycle Feedback Parameters and Cumulative Airborne Fraction Based on the Response of Various Coupled Climate–Carbon Cycle Models by 2100 to the A2 Emissions Scenario

Model	DGVM?	ρ W m ⁻² K ⁻¹	β GtC/GtC	γ GtC K	u_γ -	r_β W m ⁻² K ⁻¹	r_γ W m ⁻² K ⁻¹	A -	f_c -
Terrestrial biosphere modules without C–N coupling									
HadCM3LC	Yes	1.56	0.99	-201	-0.62	1.54	-0.98	0.73	-0.37
IPSL-CM2C	No	1.59	1.50	-128	-0.39	2.39	-0.62	0.47	-1.11
IPSL-CM4-LOOP	Yes	1.43	1.13	-36	-0.12	1.62	-0.17	0.50	-1.01
CMS-1	?	2.72	0.94	-40	-0.07	2.55	-0.19	0.54	-0.87
MPI	?	1.26	1.17	-87	-0.34	1.48	-0.42	0.54	-0.83
LLNL	Yes	1.52	1.74	-84	-0.27	2.64	-0.41	0.40	-1.47
FRCGC	No	1.75	1.13	-158	-0.44	1.97	-0.77	0.59	-0.69
UMD	Yes	1.84	0.80	-107	-0.28	1.47	-0.52	0.66	-0.52
UVic-2.7	Yes	1.64	1.08	-141	-0.42	1.77	-0.68	0.60	-0.66
CLIMBER	Yes	1.95	0.94	-79	-0.20	1.83	-0.38	0.57	-0.74
BERN-CC	Yes	2.24	1.36	-144	-0.31	3.06	-0.70	0.49	-1.05
Mean		1.77	1.16	-110	-0.31	2.03	-0.53	0.55	
Standard Deviation		0.41	0.27	51	0.16	0.54	0.25	0.09	-
Terrestrial biosphere modules with C–N coupling									
MIT-IGSM2.3			0.89	13	0.04	1.57	0.06	0.52	-0.92
CCSM3.0			0.56	20	0.06	1.00	0.10	0.62	-0.62
IPSL-CM4-LOOP	Yes	1.43	0.81	-51	-0.17	1.15	-0.25	0.61	-0.63

A 'Yes' in the column 'DGVM' indicates that the distribution of vegetation types can shift in response to changing CO₂ concentration and climate, so that the related changes in surface albedo are included in the climate radiative feedback factor λ (which is contained in ρ). (Source: Gregory et al., 2009 for models where the terrestrial biosphere component has C–N coupling, and sources as given in Table 5.4 for the other models.) A ϕ value of 0.0049 W m⁻²GtC⁻¹ was used in computing u_γ and r_γ . The mean value of ϕ from the first 11 models was used here in computing u_γ and r_β for the MIT-IGSM2.3 and CCSM3.0 models.

where $r_\beta = \rho\beta$ and $r_\gamma = \phi\gamma$. Now, C_E is the ultimate forcing and ΔT is the response. ϕC_E is the radiative forcing that would occur with no carbon cycle or climate–carbon cycle feedbacks; $r_\beta\Delta T = \phi\beta C_A$ is the reduction in radiative forcing due to carbon cycle feedback and $-r_\gamma\Delta T = -\phi\gamma\Delta T$ is the increase in radiative forcing due to climate–carbon cycle feedback. The net forcing is offset by an increased heat flux to space or the deep ocean, $\rho\Delta T$. The beauty of this formulation is that the heat flux damping, carbon cycle feedback, and climate–carbon cycle feedback are now represented with metrics (ρ , r_β , and r_γ) having the same units (W m⁻² K⁻¹), so that they can be directly compared with one another.

Table 5.5 gives the overall values for β and γ (from Table 5.4), along with ρ values and the corresponding values of u_β , u_γ , and A as computed by Gregory et al. (2009), and f_c as computed here. The models that allow the vegetation distribution to shift in response to changing atmospheric CO₂ concentration and climate are indicated in Table 5.5 as, in these models, λ and hence ρ includes the contribution from surface albedo changes due to changes in the distribution of different biomes. The negative carbon cycle feedback (represented by r_β) is on average slightly stronger than the combined radiative and ocean heat flux damping (represented by ρ) and, on average, is about four times stronger than the positive climate–carbon cycle feedback

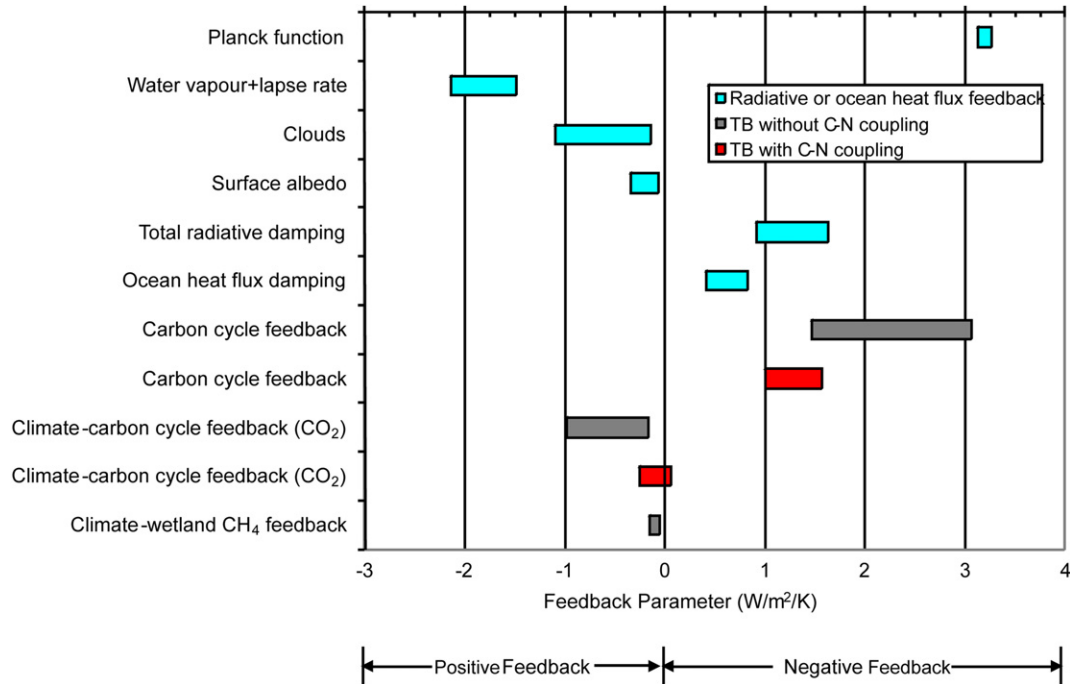


FIGURE 5.18 Range of radiative feedback or damping parameters (λ_i , from Soden and Held (2006) and shown in Figure 5.4a), heat flux damping to the deep ocean (κ , from Gregory and Forster (2008)), and carbon cycle and climate–carbon cycle feedback parameters (r_β and r_γ , as computed by Gregory et al. (2009) for models without C–N coupling in the terrestrial biosphere (TB) component, and from their table 10 for models with C–N coupling).

(represented by r_γ), but the uncertainty in the carbon cycle feedback (as represented by the standard deviation of the model r_β values) is almost twice as large as the uncertainty in the climate–carbon cycle feedback (as represented by the standard deviation of the model r_γ values) in spite of the very large variation in γ among the models.

Figure 5.18 compares the climate feedbacks (λ_i , from Figure 5.4a) and heat-flux damping to the deep ocean (κ , from Gregory and Forster, 2008) with r_β and r_γ as computed by Gregory et al. (2009). As seen from Figure 5.18 and noted above, carbon-cycle feedback is a fourfold stronger feedback than the climate–carbon cycle feedback, although the latter feedback could be as strong as the combined surface-albedo, water-vapour, and lapse-rate feedbacks. The midrange climate–carbon cycle feedback is comparable to the midrange cloud feedback (both being positive). The negative carbon cycle feedback ranges from 1/3 to 100% as strong as the negative Planck function feedback (λ_o). The coefficient for heat flux damping to the deep ocean (κ) ranges from 0.4–0.8 $\text{W m}^{-2} \text{K}^{-1}$.

5.4.4. Role of Carbon–Nitrogen (C–N) Coupling

The quantitative feedback factors discussed above are based on terrestrial biosphere models that neglect C–N

interactions. However, the stimulation of photosynthesis by higher CO_2 is likely to be restrained at some point by limitations in the supply of N. Conversely, accelerated decomposition of soil carbon due to warming will lead to a greater release of N and other nutrients back to the soil, thereby stimulating photosynthesis and, in so doing, offsetting some or all of the reduction in soil carbon. The last three data rows of Tables 5.4 and 5.5 give the feedback parameters for three models that use a terrestrial biosphere submodule that allows C–N interactions. These models are TEM (Terrestrial Ecosystem Model), the Community Land Model version 3.0 (CLM3.0), which is embedded in the NCAR (National Center for Atmospheric Research) AGCM, and the CM4 land model that is coupled to the IPSL AGCM. The average β_L value for the three models with C–N coupling is less than half that of the models without C–N coupling, while the average γ_L value is less than one tenth that of the models without C–N coupling.

In TEM, the total N content in the simulated ecosystem is constant as CO_2 and temperature increase. CLM3.0 has prognostic N inputs, including biological N fixation and losses due to wildfires, while IPSL-CM4 has variable N losses by leaching and through trace gas emissions. In the steady state, N losses (from forest fires, for example) will be balanced by N inputs (largely N fixation, with some atmospheric deposition). An increased incidence of fires

would lead to net N loss, but an increase in CO₂ tends to increase the rate of N fixation (which in turn stimulates NPP) by providing more energy to the roots (where N fixers reside). However, N fixation also requires various trace elements, particularly iron, vanadium, and molybdenum (see Dickinson, 2012, this volume). Thus, the initial increase in N fixation in CO₂ enhancement experiments is followed by down-regulation after a few years (Hungate et al., 2004).

Temperature also affects the rate of N fixation. Current surface air temperatures in the tropics are close to the optimum for N fixation but substantially below the optimum in the extra-tropics. Thus, warming will reduce N availability in the tropics and increase it in the extra-tropics (Wang and Houlton, 2009). When: (i) changes in N availability due to changes in the rate of N fixation caused by the warming climate; and (ii) increases in N deposition due to the increase fossil fuel use that ultimately drives the change in climate in the C4MIP models are taken into account, Wang and Houlton (2009) found that the increase in carbon storage on land simulated by 9 out of 11 C4MIP models (which, as already noted, do not account for N limitations) is greater than what is feasible based on an upper-bound estimate of the amount of available N. The carbon that is absorbed in the models in excess of the available N would in fact be distributed between the atmosphere and oceans. The additional warming due to non-absorption of the excess carbon is estimated by Wang and Houlton (2009) to be 0.18–0.52 K by 2050 and 0.15–0.65 K by 2100 for these models.

In summary, accounting for C–N interactions dramatically alters the response of carbon storage to both increasing atmospheric pCO₂ and temperature, but a proper accounting must include the effects of additional N losses due to fires and changes in the rate of N fixation induced by changes in atmospheric pCO₂ and temperature, as well as the effect of extra N that is released to the soil solution from increased decomposition of organic matter. Thus, it is too early to conclude that γ_L is close to zero, although it is likely to be in the lower half of the range for the models in Table 5.4 without C–N interactions.

5.4.5. Combination of Climate Sensitivity and Carbon Feedback Gain Formulation

This subsection is an extension of the analysis presented in Gregory et al. (2009). Re-introducing R_N , Equations (5.24) and (5.25) give:

$$C_E = C_A \left(1 + \beta + \frac{\phi\gamma}{\rho} \right) + \frac{\gamma}{\rho} R_N \quad (5.32)$$

instead of Equation (5.26), from which we obtain:

$$C_A = \frac{C_E - \frac{\gamma}{\rho} R_N}{1 + \beta + \frac{\phi\gamma}{\rho}} \quad (5.33)$$

Because $\gamma < 0$, R_N increases C_A for a given C_E , while γ in both the numerator and denominator of Equation (5.33) increases C_A (i.e., climate–carbon cycle feedback increases C_A through the warming that is induced by the initial emission of CO₂ and through the warming induced by the non-CO₂ forcing). Equation (5.13) becomes:

$$\Delta T = \left(\frac{G_o}{1 - f_\lambda} \right) (R_C + R_N) \quad (5.34)$$

where, now, $f_\lambda = -G_o(\lambda_{wv} + \lambda_{lr} + \lambda_c + \lambda_a + \kappa) = -G_o(\rho - \lambda_o)^{23}$. From Equations (5.25), (5.33), and (5.34) we obtain:

$$\Delta T = \left(\frac{G_o}{1 - f_\lambda} \right) \left(\phi C_E \left(\frac{1 - \left(\frac{\gamma}{\rho} \right) \left(\frac{R_N}{C_E} \right)}{1 + \beta + \frac{\phi\gamma}{\rho}} \right) + R_N \right) \quad (5.35)$$

which can be rewritten as:

$$\Delta T = \left(\frac{G_o}{1 - f_\lambda} \right) \left(\phi C_E \left(\frac{1 - (\gamma/\rho)(R_N/C_E)}{1 - f_c} \right) + R_N \right) \quad (5.36)$$

where $f_c = -\beta - u_\lambda = -\beta - \phi\gamma/(\lambda + \kappa)^{24}$. For the case where $R_N = 0$, Equation (5.36) simplifies to:

$$\Delta T = \phi \left(\frac{G_o}{1 - f_\lambda} \right) \left(\frac{1}{1 - f_c} \right) C_E \quad (5.37)$$

Over a period of time, κ decreases as the deep ocean warms (increasing f_λ and tending to increase ΔT because there is a smaller heat flux into the deep ocean), while β increases as an increasing amount of the emitted CO₂ is absorbed by the oceans (decreasing f_c and tending to decrease ΔT). Over a period on the order of 100,000 years, $\beta \rightarrow \infty$ (the airborne fraction goes to zero because all of the emitted CO₂ is eventually absorbed by the oceans or consumed through enhanced rock weathering), which drives ΔT to zero.

The ratio of the temperature response with climate–carbon cycle feedback to the response without this feedback is equal to:

$$R = \frac{1 + \beta}{1 + \beta + \phi\gamma/\rho} \quad (5.38)$$

23. As f_λ now includes the transient heat flux to the ocean, Equation (5.34) gives the instantaneous, rather than the equilibrium, ΔT .

24. Recall that $\lambda_i < 0$ and $\gamma < 0$ are positive feedbacks.

This ratio is >1 because $\gamma < 0$. From Equation (5.38), it can be seen that the impact of a given climate–carbon cycle feedback (represented by γ) is greater the larger the climate sensitivity (i.e., the smaller ρ).

5.4.6. Applying Climate Sensitivity to Future Climate Policy Strategies

Taplin (2012, this volume) reviews the current situation regarding international negotiations on fossil fuel emissions reduction. All policy decisions have climate consequences, which can be quantitatively assessed using climate sensitivity analysis. We illustrate the application of the preceding analysis to scenarios with cumulative fossil fuel emissions by 2100 of 680 GtC, 1100 GtC, and 1640 GtC (corresponding to the most stringent climate policy scenario, the least stringent climate policy scenario, and the high business-as-usual scenario of Harvey (2010b), respectively), plus 120 GtC cumulative emission from land-use changes in each case²⁵. The feedback parameters depend, to some extent, on the specific emission scenario, but we will use lower and upper bounds from the estimates reviewed here (Table 5.5). It is assumed that the carbon cycle and climate–carbon cycle feedbacks combine linearly (that is, they do not interfere with each other), which is only approximately true. In spite of these limitations, a number of useful insights can be gained through the application of the linear feedback analysis.

Figure 5.19 shows the (peak) temperature response for the three emissions scenarios as computed from Equation (5.35) for λ chosen to give fast-feedback climate sensitivities of 2 or 4 K, for $\beta = 0.9$ or 1.7, and for $\gamma = -40$ GtC K or -200 GtC K. These temperatures are computed iteratively, since ΔT depends on ϕ and C_E through Equation (5.35), ϕ depends on C_A through Equation (5.25), and C_A depends on ϕ through Equation (5.33). A non-CO₂ radiative forcing R_N of 1.0 W m^{-2} is assumed in all cases. Also given in Figure 5.19 for each (γ, β) combination are the ratios of the temperature change with climate–carbon cycle feedback to the corresponding case without climate–carbon cycle feedback.

The lowest part of each bar in Figure 5.19 gives the temperature response when $\kappa = 0.8 \text{ W m}^{-2} \text{ K}^{-1}$ (the upper limit of the uncertainty range given in Table 5.3), the next segment of each bar gives the additional temperature response if $\kappa = 0.4 \text{ W m}^{-2} \text{ K}^{-1}$ (the lower limit of the

uncertainty range in Table 5.3) instead of $\kappa = 0.8 \text{ W m}^{-2} \text{ K}^{-1}$, and the top segment gives the additional temperature response if there is no heat flux to the deep ocean. The last case is unrealistic but serves to illustrate the overall importance of heat absorption by the oceans in limiting the warming. Figure 5.20 gives the corresponding peak atmospheric CO₂ concentrations. The ratio of temperature response with and without the ocean heat flux is smaller than $\lambda/(\lambda + \kappa)$, especially for cases with a strong positive climate–carbon cycle feedback (large negative γ). This is because the CO₂ concentration itself is smaller the larger the heat flux to the ocean (as can be seen from Figure 5.20), due to weaker climate–carbon cycle feedback the more that the transient warming is limited.

As seen from Figure 5.19, the relative impact of climate–carbon cycle feedback is largest for the scenario with the lowest cumulative emission (because the CO₂ radiative forcing varies with the logarithm of CO₂ concentration), for smaller negative carbon cycle feedback, and for larger climate sensitivity (as expected from Equation 5.38).

The parameter values and the peak CO₂ concentration for the business-as-usual emissions scenario with high climate sensitivity, weak carbon cycle feedback, and strong climate–carbon cycle feedback correspond closely to those of the Hadley Centre model reported by Cox et al. (2000, 2004), whereby atmospheric CO₂ reaches a concentration of about 750 ppmv by 2100 without climate–carbon cycle feedback and about 1000 ppmv with climate–carbon cycle feedback.

The climate–carbon cycle feedback parameter used in the above calculations does not include the effect of CH₄ or CO₂ release from thawing permafrost or melting of clathrates. The impact of potential GHG releases from thawing yedoma soils was assessed by Harvey (2010b) using the coupled climate–carbon cycle model of Harvey (2001) and is presented here in Figure 5.21. In line with the simulations by Khvorostyanov et al. (2008a) and observational evidence cited earlier, it is assumed that the rate of carbon release increases linearly from 0 GtC per year at 0.8 K global mean warming (i.e., starting from the present) to 0.3 GtC per year at 3.3 K global mean warming, then increases to 3 GtC per year at 4.3 K global mean warming and continues until the cumulative emission reaches 300 GtC, then abruptly stops. It is further assumed that 25% of the released C is emitted to the atmospheric in the form of CH₄, and the balance as CO₂. Figure 5.21a shows the variation in global mean temperature for an emissions scenario that gives a peak global mean warming of 3.38 K with a climate sensitivity of 3 K and in the absence of yedoma feedback. However, assuming that carbon release from yedoma soils begins slowly, it unleashes a positive feedback sufficient to push the peak warming to 5.6 K. This, in turn, is large enough to unleash a CH₄–clathrate feedback sufficient to cause an additional

25. The cumulative fossil fuel emissions to 2100 in the business-as-usual scenarios of Harvey (2010b) range from 820–1640 GtC. These are much less than typical business-as-usual scenarios, which see cumulative emissions (beyond 2100) of about 5000 GtC, but are based on recent evidence that the useable coal resource is far less than is traditionally assumed and that the global coal supply will probably peak within the next few decades (see Harvey 2010a, section 2.5.3; Patzek and Croft, 2010). The cumulative fossil fuel CO₂ emission to 2010 is about 375 GtC.

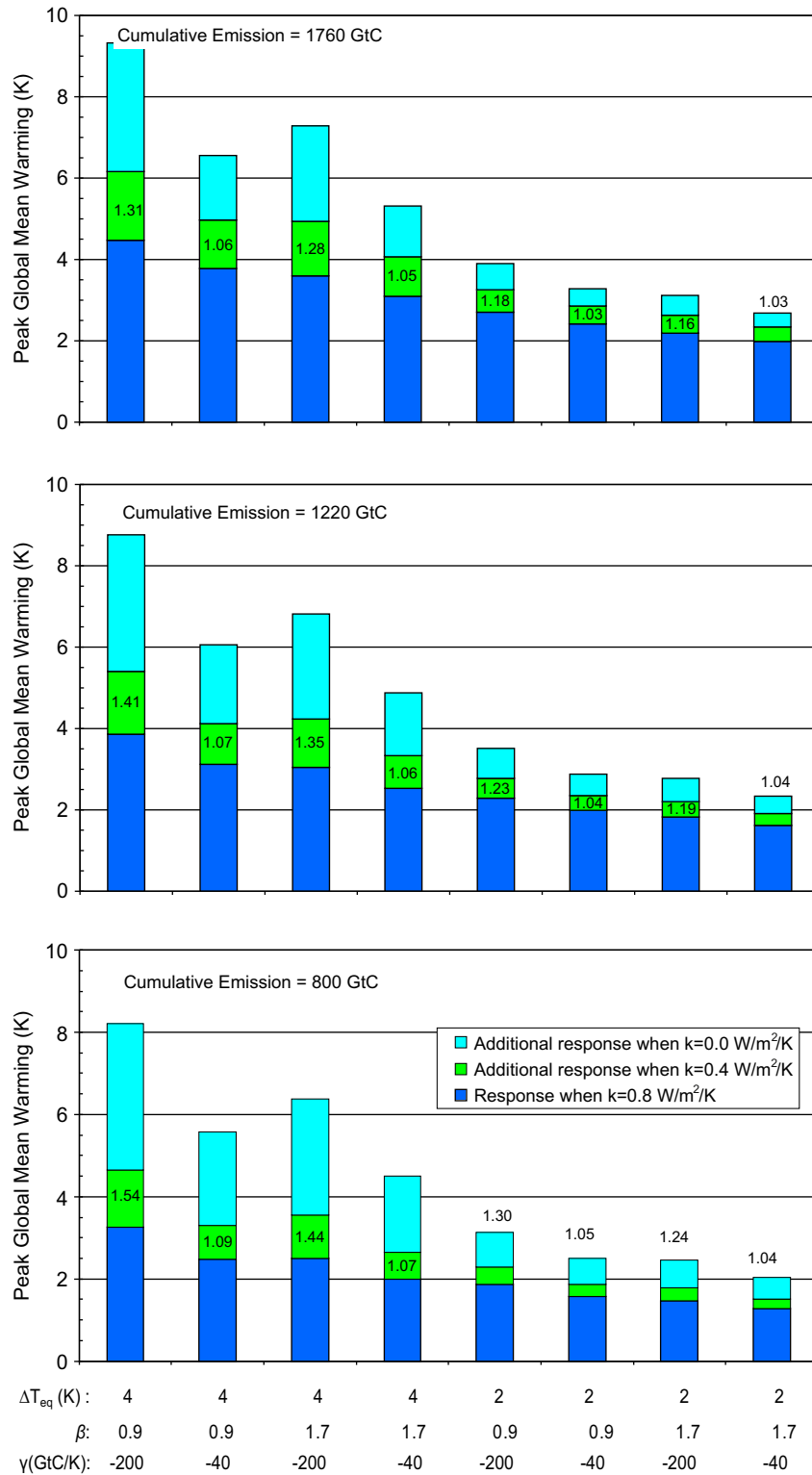


FIGURE 5.19 Peak global mean warming as estimated from Equation (5.33) for cumulative anthropogenic CO₂ emissions of 800 GtC, 1220 GtC, and 1760 GtC for various climate sensitivities (ΔT_{2x}), carbon cycle feedback parameters (β), and climate–carbon cycle feedback parameters (γ). Shown is the warming when $\kappa = 0.8 \text{ W m}^{-2} \text{ K}^{-1}$, the additional warming when $\kappa = 0.4 \text{ W m}^{-2} \text{ K}^{-1}$ instead of $\kappa = 0.8 \text{ W m}^{-2} \text{ K}^{-1}$, and the additional hypothetical warming with no oceanic uptake of heat.

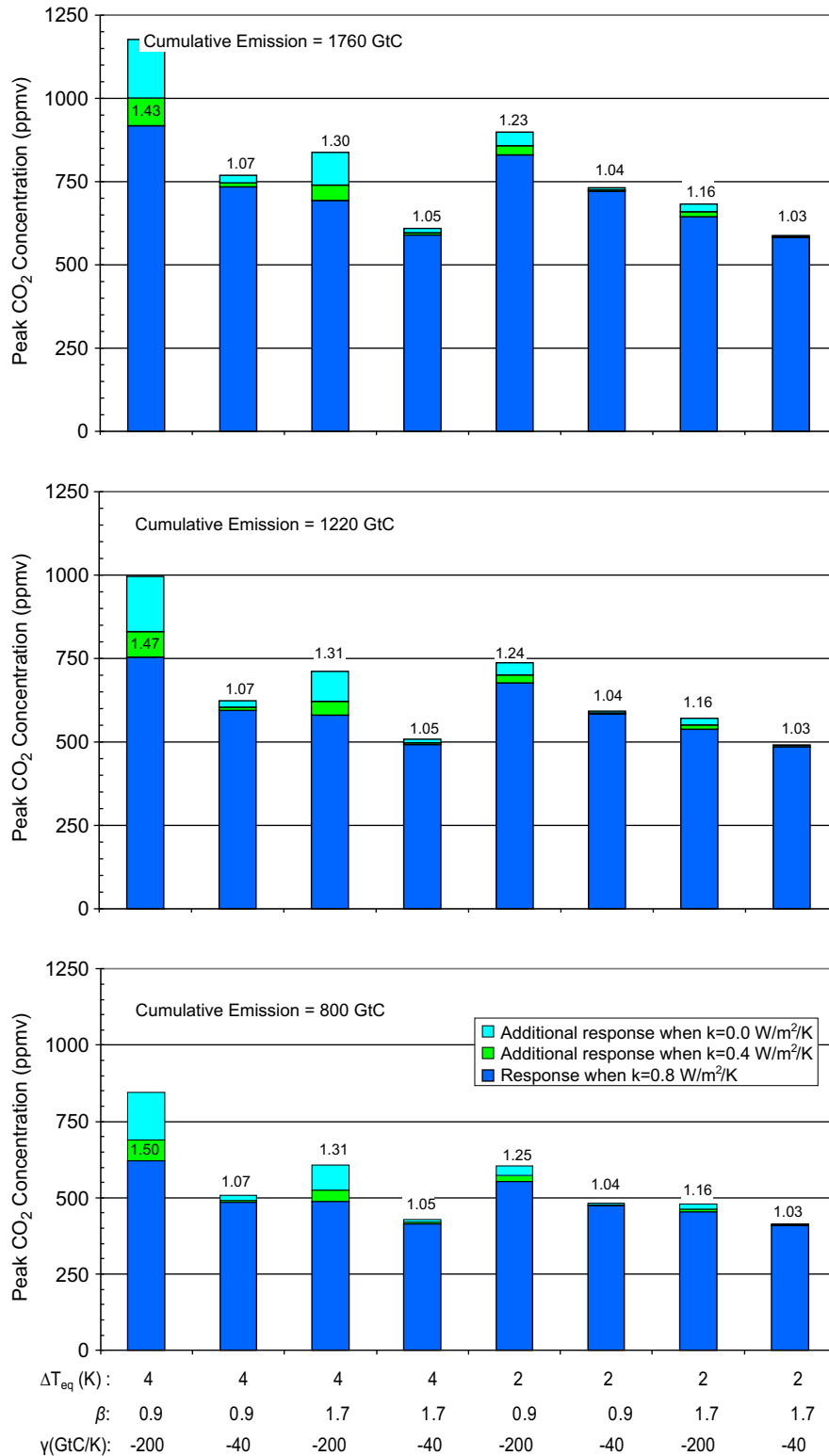


FIGURE 5.20 As for Figure 5.19 except showing peak atmospheric CO₂ concentrations based on C_A as estimated from Equation (5.31).

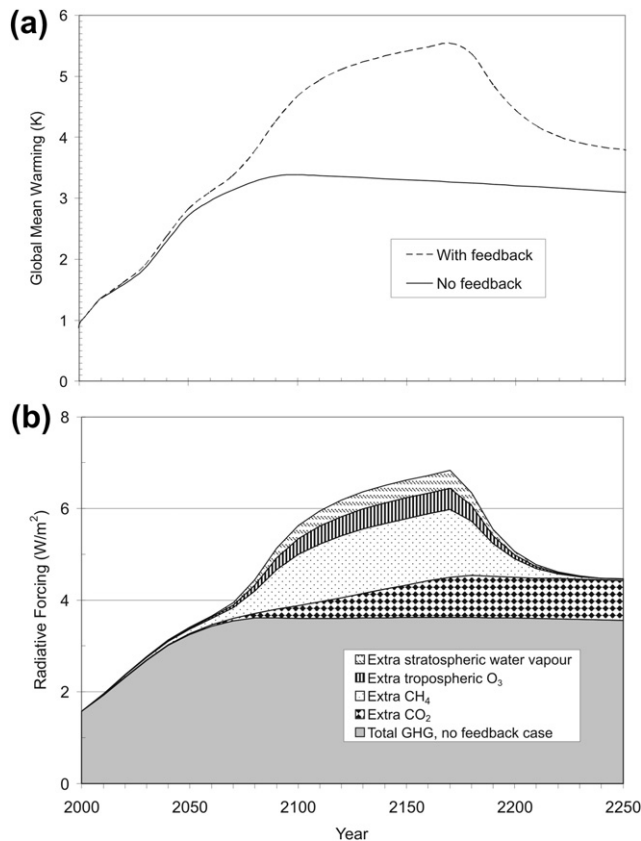


FIGURE 5.21 (a) Variation in global mean temperature for an emissions scenario—climate sensitivity combination that produces a peak warming of 3.3 K in the absence of carbon release from yedoma soils ('No feedback') and the result when a gradual release begins at 0.8 K warming, as explained in the text ('With feedback'). (b) Contributions to the total radiative forcing for the case with yedoma feedback.

1–2 K warming over the course of 300–500 years (Harvey and Huang, 1995). Figure 5.21b shows the different contributions to the extra radiative forcing caused by emissions of CO_2 and CH_4 from thawing yedoma soils. The total radiative forcing is more than doubled by the end of the carbon emissions, but the temperature response does not quite double due to the delay in warming caused by oceans combined with the rapid decline in those forcings related to CH_4 release once emissions cease.

5.5. OTHER SLOW AND LESS-CONSIDERED FEEDBACKS

Other feedbacks that may alter the long-term sensitivity to GHG increases are less frequently considered in the literature. These include biological effects (physiological and plant-type distribution changes), oceanic and marine biospheric changes, and Greenland ice-cap melting (Lenton, 2012, this volume).

5.5.1. Enhanced Land Surface Warming Due to the Physiological Effect of Higher CO_2

The increase in atmospheric CO_2 leads to a restriction in stomatal opening, reducing evaporative cooling and thereby increasing the local warming of the land surface compared to the case without physiological effects of higher CO_2 (Sellers et al., 1996; Betts et al., 1997). The reduction in evapotranspiration also triggers changes in the atmospheric water vapour content and cloudiness, which alters the radiative energy fluxes and thereby alters the final global-scale temperature change.

According to a simulation with the HadCM3LC model, the resulting decrease in evapotranspiration following an instantaneous doubling or quadrupling of atmospheric CO_2 rapidly leads to a decrease in low cloud cover that adds about 15% to the original CO_2 forcing (that is, a 15% increase in ΔR_{eff}) with no statistically significant change in the radiative feedback parameter λ (Doutriaux-Boucher et al., 2009). Thus, ΔT also increases by about 15%, irrespective of the overall feedback strength — unlike the case where there is a perturbation in λ itself, in which case the impact on temperature depends on the pre-existing feedback strength (as seen in Figure 5.2). In simulations using the NCAR Community Atmospheric Model and Community Land Model, Cao et al. (2010) find that partial stomatal closure increases the average surface air warming over land from 2.86 K to 3.33 K (a 16% increase). This is due to reduced evaporative cooling and reduced low-level cloud cover.

5.5.2. Shifts in the Distribution of Plant Functional Types

Several different models have been developed that simulate both the distribution of vegetation types and the amount of carbon stored as biomass and in the soil, as well as the physical coupling with the atmosphere through exchanges of heat, moisture, and momentum. These models are referred to as dynamic global vegetation models (DGVMs). Experiments with DGVMs indicate that eventual shifts in vegetation in response to the initial warming enhance the global mean temperature response to increasing CO_2 by about 10%–13% (O'ishi and Abe-Ouchi, 2009; O'ishi et al., 2009; Gregory et al., 2009).

Matthews et al. (2007) carried out experiments with a coupled AOGCM-DGVM in which an increase in atmospheric CO_2 to 770–926 ppmv but with no CO_2 radiative effects induced a global mean surface warming of about 0.2 K, solely as a result of changes in the distribution of different vegetation types. Matthews and Keith (2007) state that the warming caused by vegetation shifts induced by higher CO_2 largely offsets the cooling effect from the uptake of CO_2 induced by higher atmospheric CO_2 in the fully-coupled version of their model. This effect is

equivalent to changing f_c from $-(\beta_L + \beta_O + u_\lambda)$ to $-(\beta_O + u_\lambda)$; that is, increasing the magnitude of the positive f_c .

5.5.3. Decrease in the Extent of the Greenland Ice Cap

On a timescale of many centuries to a few thousand years, complete melting of the Greenland ice sheet could occur in association with global mean warming of as little as $1-2 \text{ K}^{26}$. This would replace a high albedo (0.7) surface with a low-albedo (0.25) surface over an area of 1.7 million km^2 . The average solar irradiance on the Greenland ice sheet is about 100 W m^{-2} , so the change in the global mean absorption of solar radiation resulting from complete disappearance of the Greenland ice sheet would be about 0.15 W m^{-2} ²⁷. However, this feedback would not increase the peak warming in response to anthropogenic emissions of CO_2 because significant retreat of the Greenland ice cap would not have occurred until long after atmospheric CO_2 concentration had peaked and then begun to decline (Lenton, 2012, this volume).

5.5.4. Delayed Ocean Circulation Changes and Cloud Feedback

As noted earlier (Section 5.2.6.2), a rather large climate sensitivity (6–10 K) has been deduced for the early Pliocene (3–5 Ma). Prior to 3 Ma, there was a permanent El Niño condition, with greater warming in the eastern equatorial Pacific than in the western equatorial Pacific relative to today (Fedorov et al., 2006). This would have resulted in less low-level cloud prior to 3 Ma and hence a lower planetary albedo, and might explain the relatively warm conditions of the early Pliocene with almost the same external forcing factors as today (Barreiro et al., 2006). The critical question is, would initial warming due to anthropogenic emissions of GHGs provoke a flip to a permanent El Niño condition that would trigger a jump in the climate sensitivity? The answer to this question depends on the reason for the permanent El Niño condition during the early Pliocene. Fedorov et al. (2006) rule out closure of the Panamanian seaway as a trigger for the

transition away from the permanent El Niño condition, since it occurred too early (between 4.0 and 4.5 Ma). Rather, the loss of the permanent El Niño condition seems to be related to high latitude cooling, which would have produced a shallower thermocline at low latitudes, thereby permitting tropical winds to bring cold waters to the surface in the eastern equatorial Pacific and other upwelling regions (Fedorov et al., 2004).

The reverse process could occur if extra-tropical waters become less saline as the climate warms, since sufficiently large freshening in the extra-tropics can induce a permanent El Niño. In simulations with an idealized OCGM, Fedorov et al. (2004) find that a gradual increase in the surplus of precipitation over evaporation in the northern Pacific Ocean induces an abrupt transition to a permanent El Niño state once a critical threshold is passed. The transition occurs on a timescale of decades. Alternatively, a reduction in the rate of heat loss from the oceans to the atmosphere could deepen the tropical thermocline, thereby reducing the near-surface upwelling of cold water (Fedorov et al., 2006). After GHG concentrations are stabilized, it is possible that the climate could at first appear to be adjusting to a relatively low (1.5–4.5 K) climate sensitivity, only to make a rapid transition to a higher sensitivity once a critical threshold involving the subsurface ocean temperature structure is passed. However, to the extent that the higher sensitivity is the result of a one-time threshold crossing, it would not be applicable to the radiative forcing in excess of that needed to cross the threshold.

5.5.5. Collapse of Marine Bioproductivity and Cloud Feedback

One of the unsolved mysteries concerning past climates is the cause of exceptionally warm conditions (35°C tropical SST, 10°C polar temperatures) during the middle Cretaceous (about 100 Ma), particularly if CO_2 concentration never exceeded about $5 \times$ pre-industrial (1500 ppmv). At 35°C , marine bioproductivity would have been greatly reduced compared to at present, leading to greatly reduced emission of dimethylsulfide, a key precursor to cloud condensation nuclei (CCN). This in turn would have lowered cloud reflectivity, constituting a strong positive feedback. Kump and Pollard (2008) tested the impact of a tenfold to 100-fold decrease in CCN amounts in combination with $4 \times \text{CO}_2$ in an AGCM that explicitly computes cloud optical properties. They find that there are fewer and optically thinner clouds, reducing global mean planetary albedo from 0.30 to 0.24. With today's solar luminosity, this would produce an increase in global mean absorption of solar radiation by about 20 W m^{-2} , which is three times the radiative forcing due to a quadrupling of atmospheric CO_2 .

26. Evidence supporting this possibility is twofold: (i) sea level during the last interglacial, when global mean temperature was $1-2 \text{ K}$ warmer, is estimated to have been 6–9 m above present sea level (Kopp et al., 2009), an amount that requires a substantial or total loss of Greenland ice, depending on the concurrent loss of West Antarctic ice; and (ii) the trend line for the area of the Greenland ice sheet subject to at least one day of melting per year is a 45% increase from 1979–2005 (Fettweis et al., 2007) in association with only 0.8 K global mean warming since the late nineteenth century, while the ice sheet made the transition in the early 2000s from annually increasing to annually decreasing ice mass (Velicogna, 2009).

27. This rough estimate neglects changes in the atmospheric masking of surface albedo changes due, for example, to a change in cloudiness.

5.6. CLIMATE FEEDBACKS AND THE FUTURE CLIMATE

The climate response to anthropogenic emissions of CO₂ involves negative feedbacks between atmospheric CO₂ concentration and the absorption of CO₂ by the oceans and terrestrial biosphere (carbon cycle feedbacks), a variety of fast (days to months) radiative feedbacks (climate feedbacks), coupled climate–carbon cycle feedbacks that unfold over a period of decades to centuries, and other slow feedbacks involving the response of the Greenland and Antarctic ice sheets and slow changes in the ocean circulation and subsurface temperature field (which can alter surface temperature patterns and cloud feedbacks).

There is comprehensive and widespread evidence that the traditional climate sensitivity, based on fast feedback processes only, is very likely (90% probability) to fall between the long-held consensus limits of 1.5 K and 4.5 K. In scenarios where the effective CO₂ concentration increases exponentially by 1% per year until it doubles, the realized global mean temperature change at the time of a CO₂ doubling is typically 60%–75% of the equilibrium warming, with an average over 16 AOGCMs of 70%. Extremely stringent scenarios for reductions in emissions of all GHGs (with CO₂ emission reaching zero by 2085) still result in peak GHG concentrations close to the equivalent of a CO₂ doubling; anything less will result in an even greater equivalent CO₂ concentration. As these scenarios require reducing CO₂ emissions from fossil fuel use and biomass burning to near zero, they would also lead to the elimination of the current cooling effect of aerosols. Thus, the minimum expected peak warming – excluding the effects of positive climate–carbon cycle feedbacks – can be estimated based on the minimum peak equivalent CO₂ concentration, the fast feedback climate sensitivity, and the ratio of realized to equilibrium warming. This gives a minimum peak warming of 1.0 K to 3.5 K.

Climate–carbon cycle feedbacks involving the ocean sink are likely to be small. Feedbacks involving photosynthesis, respiration, and the dieback of maladapted terrestrial ecosystems, as estimated from various models, have ranged from small (sufficient to amplify the temperature response by 4%–9%) to very large (sufficient to amplify the temperature response by about 15%–50%), with greater amplification if the negative carbon cycle feedback is small and the climate sensitivity large. Inclusion of soil C–N interactions greatly reduces the strength of both the stimulation of carbon uptake by higher CO₂ and the positive climate–carbon cycle feedback, but there are still many uncertainties concerning most processes involved in both carbon cycle and climate–carbon cycle feedbacks.

Much greater amplification of the future warming could occur through release of CO₂ and CH₄ from thawing

yedoma soils (where significant fluxes could arise within 100 years and then be sustained for another 100 years) and from destabilization of marine CH₄ clathrates (where non-negligible fluxes could begin within 100 years and potentially catastrophic fluxes could arise within a few centuries). If global mean warming reaches 3–4 K, yedoma feedback could push the warming a further 2 K, at which point CH₄ releases from marine clathrates could be large enough to add another 2 K. Some time during this process, a threshold involving the temperature of upwelling water in the eastern equatorial Pacific could be crossed, leading to an abrupt (within decades) transition to a permanent El Niño state and a potentially large positive cloud feedback that might add another 1–2 K global mean warming²⁸. Yet further warming could occur through collapse of the marine biosphere (which would be likely at this point) and concomitant reductions in cloud albedo leading to a reduction in global mean planetary albedo from 0.30 to 0.24.

A global mean warming of 10–12 K beyond AD 2100 is a distinct possibility if the fast-feedback climate sensitivity is near the upper end of the 1.5–4.5 K uncertainty range, if the slow positive feedbacks are near the high end of the possible range that has been identified here, and if the recoverable fossil fuel resource is as large as 4000–5000 GtC (as is commonly assumed) and most of it is used. As shown by Sherwood and Huber (2010), global mean warming of this magnitude would render portions of the world currently occupied by over half of the human population to be uninhabitable by humans (in the absence of access to 100% reliable air-conditioning by the entire populations in the affected regions) due to the periodic occurrence of 6-hour mean wet-bulb temperatures in excess of the practical physiological limit of 33°C. Very serious social and political upheaval that could provoke military conflict (Dyer, 2008) would occur long before this point is reached, and could be an outcome of more moderate fossil fuel emissions (1000–2000 GtC cumulative emission) and less than worst-case fast and slow feedback climate sensitivities. Further research could perhaps provide a better assessment of the likelihood of catastrophic climate–carbon cycle and other slow feedbacks as a function of the cumulative fossil fuel CO₂ emission and of the underlying fast-feedback climate sensitivity.

ACKNOWLEDGEMENTS

This paper benefited from comments by Josep Canadell and three anonymous reviewers.

28. This is the temperature response associated with 350–450 ppmv CO₂ during the early Pliocene beyond that expected based on the fast-feedback climate sensitivity, and is assumed to be a one-time increment in temperature response as GHG concentrations continue to increase.

References

- Allen, C.D., A.K. Macalady, H. Chenchouni, D. Bachelet, N. McDowell, M. Vennetier, T. Kitzberger, A. Rigling, D. D. Breshears, E. H. Hogg, P. Gonzalez, R. Fensham, Z. Zhang, J. Castro, N. Demidova, J.-H. Lim, G. Allard, S. W. Running, A. Semerci and N. Cobb (2010), A global overview of drought and heat-induced tree mortality reveals emerging climate change risks for forests, *For. Ecol. Manage.*, 259, 660-684.
- Annan, J. D. and J. C. Hargreaves (2006), Using multiple observationally-based constraints to estimate climate sensitivity, *Geophys. Res. Lett.*, 33, L06704.
- Aragão, L. E., Y. Malhi, R. M. Roman-Cuesta, S. Saatchi, L. O. Anderson, and Y. E. Shimabukuro (2007), Spatial patterns and fire response of recent Amazonian droughts, *Geophys. Res. Lett.*, 34, L07701, doi:10.1029/2006GL028946.
- Archer, D. (2007) Methane hydrate stability and anthropogenic climate change, *Biogeosciences*, 4, 521-544.
- Archer, D., B. Buffett, and V. Brovkin (2009), Ocean methane hydrates as a slow tipping point in the global carbon cycle, *Proc. Nat. Acad. Sci.*, 106, 20596-20601.
- Balshi, M. S., A. D. McGuire, P. Duffy, M. Flannigan, D. W. Kicklighter, and J. Melillo (2009), Vulnerability of carbon storage in North American boreal forests to wildfires during the 21st century, *Global Change Biology*, 15, 1491-1510.
- Barlow, J. and C. A. Peres (2008), Fire-mediated dieback and compositional cascade in an Amazonian forest, *Phil. Trans. R. Soc. B*, 363, 1787-1794.
- Barreiro, M., G. Philander, R. Pacanowski, and A. Fedorov (2006), Simulations of warm tropical conditions with application to middle Pliocene atmospheres, *Clim. Dyn.*, 26, 349-365.
- Beaugrand, G., M. Edwards, K. Brander, C. Luczak, and F. Ibañez (2008), Causes and projections of abrupt climate-driven ecosystem shifts in the North Atlantic, *Ecology Letters*, 11, 1157-1168.
- Beaugrand, G., M. Edwards, and L. Legendre (2010), Marine biodiversity, ecosystem functioning, and carbon cycles, *Proc. Nat. Acad. Sci.*, 107, 10120-10124.
- Behrenfeld, M. J., R. T. O'Malley, D. A. Siegel, C. R. McClain, J. L. Sarmiento, G. C. Feldman, A. J. Milligan, P. G. Falkowski, R. M. Letelier, and E. S. Boss (2006), Climate-driven trends in contemporary ocean productivity, *Nature*, 444, 752-755.
- Bender, F. A. -M., A. M. L. Ekman, and H. Rodhe (2010), Response to the eruption of Mount Pinatubo in relation to climate sensitivity in the CMIP3 models, *Clim. Dyn.*, 35, 875-886.
- Betts, R. A., P. M. Cox, S. E. Lee, and F. I. Woodward (1997), Contrasting physiological and structural vegetation feedbacks in climate change simulations, *Nature*, 387, 796-799.

- Bijl, P. K., A. J. P. Houben, S. Schouten, S. M. Bohaty, A. Sluijs, G. -J. Reichart, J. S. S. Damsté, and H. Brinkhuis (2010), Transient middle Eocene atmospheric CO₂ and temperature variations, *Science*, 330, 819-821.
- Boisvenue, C. and S. W. Running (2006), Impacts of climate change on natural forest productivity – evidence since the middle of the 20th century, *Global Change Biology*, 12, 862-882.
- Bony, S., R. Colman, V. M. Kattsov, R. P. Allan, C. S. Bretherton, J.-L. Dufresne, A. Hall, S. Hallegatte, M. M. Holland, W. Ingram, D. A. Randall, B. J. Soden, G. Tselioudis, and M. J. Webb (2006), How well do we understand and evaluate climate change feedback processes? *J. Clim.*, 19, 3445-3482.
- Bopp, L., C. Le Quéré, M. Heimann, and A. C. Manning (2002), Climate-induced oceanic oxygen fluxes : Implications for the contemporary carbon budget, *Glob. Biogeochem. Cycles*, 16, 10.1029/2001GB001445.
- Bopp, L., O. Aumont, P. Cadule, S. Alvain, and M. Gehlen (2005), Response of diatoms distribution to global warming and potential implications: A global model study, *Geophys. Res. Lett.*, 32, L19606, doi:10.1029/2005GL02653.
- Boyce, D. G., M. R. Lewis, and B. Worm (2010), Global phytoplankton decline over the past century, *Nature*, 466, 591-596.
- Breecker, D. O., Z. D. Sharp, and L. D. McFadden (2010), Atmospheric CO₂ concentrations during ancient greenhouse climates were similar to those predicted for A.D. 2100, *Proc. Nat. Acad. Sci.*, 107, 576-580.
- Breshears, D. D., N. S. Cobb, P. M. Rich, K. P. Price, C. D. Allen, R. G. Balice, W. H. Romme, J. H. Kastens, M. L. Floyd, J. Belnap, J. J. Anderson, O. B. Myers, and C. W. Meyer (2005), Regional vegetation die-off in response to global-change-type drought, *Proc. Nat. Acad. Sci.*, 102, 15144-15148.
- Brohan, P., J.J. Kennedy, I. Harris, S. F. B. Tett and P. D. Jones (2006), Uncertainty estimates in regional and global observed temperature changes: a new dataset from 1850, *J. Geophys. Res.*, 111, D12106, doi:10.1029/2005JD006548.
- Came, R. E., J. M. Eiler, J. Veizer, K. Azmy, U. Brand, and C. R. Weidman (2007), Coupling of surface temperatures and atmospheric CO₂ concentrations during the Palaeozoic era, *Nature*, 449, 198-201.
- Canadell, J. G., D. E. Pataki, R. Gifford, R. A. Houghton, Y. Luo, M. R. Raupach, P. Smith and W. Steffen (2007), Saturation of the terrestrial carbon sink, in J. G. Canadell, D. Pataki and L. Pitelka (eds.), *Terrestrial Ecosystems in a Changing World*, The IGBP Series, Springer-Verlag, Berlin and Heidelberg, 59-78.
- Cao, L. and A. Jain (2005), An Earth system model of intermediate complexity: Simulation of the role of ocean mixing parameterizations and climate change in estimated uptake for natural and bomb radiocarbon and anthropogenic CO₂, *J. Geophys. Res.*, 110, C09002, doi:10.1029/2005JC002919.

- Cao, L., G. Bala, K. Caldeira, R. Nemani, and G. Ban-Weiss (2010), Importance of carbon dioxide physiological forcing to future climate change, *Proc. Nat. Acad. Sci.*, 107, 9513-9518.
- Carnicer, J., M. Coll, M. Ninyerola, X. Pons, G. Sánchez and J. Peñuelas (2011), Widespread crown condition decline, food web disruption, and amplified tree mortality with increased climate change-type drought, *Proc. Nat. Acad. Sci.*, 108, 1474-1478.
- Chuck, A., T. Tyrrell, I. J. Totterdell, and P. M. Holligan (2005), The oceanic response to carbon emissions over the next century: investigations using three ocean carbon cycle models, *Tellus*, 57B, 70-86.
- Chylek, P., U. Lohmann, M. Dubey, M. Mishchenko, R. Kahn, and A. Ohmura (2007), Limits on climate sensitivity derived from recent satellite and surface observations, *J. Geophys. Res.*, 112, D24S04, doi:10.1029/2007JD008740.
- Ciais, Ph., M. Reichstein, N. Viovy, A. Granier, J. Ogée, V. Allard, M. Aubinet, N. Buchmann, Chr. Bernhofer, A. Carrara, F. Chevallier, N. De Noblet, A. D. Friend, P. Friedlingstein, T. Grünwald, B. Heinesch, P. Keronen, A. Knohl, G. Krinner, D. Loustau, G. Manca, G. Matteucci, F. Miglietta, J. M. Ourcival, D. Papale, K. Pilegaard, S. Rambal, G. Seufert, J. F. Soussana, M. J. Sanz, E. D. Schulze, T. Vesala and R. Valentini (2005), Europe-wide reduction in primary productivity caused by the heat and drought in 2003, *Nature*, 437, 529-533.
- Coley, P. D. (1998), Possible effects of climate change on plant/herbivore interactions in moist tropical forests, *Clim. Change*, 39, 455-472.
- Cox, P. M., R. A. Betts, C. D. Jones, S. A. Spall, and I. J. Totterdell (2000), Acceleration of global warming due to carbon-cycle feedbacks in a coupled climate model, *Nature*, 408, 184-187.
- Cox, P. M., R. A. Betts, M. Collins, P. P. Harris, C. Huntingford, and C. D. Jones (2004), Amazonian forest dieback under climate-carbon cycle projections for the 21st century, *Theor. Appl. Climatol.*, 78, 137-156.
- Craine, J. M., N. Fierer, and K. K. McLauchlan (2010), Widespread coupling between the rate and temperature sensitivity of organic matter decay, *Nature Geoscience*, 3, 854-857.
- Crueger, T., E. Roeckner, T. Raddatz, R. Schnur, and P. Wetzell (2008), Ocean dynamics determine the response of oceanic CO₂ uptake to climate change, *Clim. Dyn.*, 31, 151-168.
- da Costa, A. C. L., A. C. L., D. Galbraith, S. Almeida, B. T. T. Portela, M. da Costa, J. de A. Silva, A. P. Braga, P. H. L. de Gonçalves; A. A. de Oliveira, R. Fisher, O. L. Phillips, D. B. Metcalfe, P. Levy, and P. Meir (2010), Effect of 7 yr of experimental drought on vegetation dynamics and biomass storage of an eastern Amazonian rainforest, *New Phytologist*, 187, 579-591.
- Dai, A. (2006), Recent climatology, variability, and trends in global surface humidity, *J. Clim.*, 19, 3589-3606.

- Daufresne, M., K. Lengfellner, and U. Sommer (2009), Global warming benefits the small in aquatic ecosystems, *Proc. Nat. Acad. Sci.*, 106, 12788-12793.
- Davidson, E. A. and I. A. Janssens (2006), Temperature sensitivity of soil carbon decomposition and feedbacks to climate change, *Nature*, 440, 165-173.
- Delpierre, N., K. Soudani, C. François, B. Köstner, J.-Y. Pontailler, E. Nikinmaa, L. Misson, M. Aubinet, C. Bernhofer, A. Granier, T. Grünwald, B. Heinesch, B. Longdoz, J.-M. Ourcival, S. Rambal, T. Vesala, and E. Dufrêne (2009), Exceptional carbon uptake in European forests during the warm spring of 2007: a data-model analysis, *Global Change Biology*, 15, 1455-1474.
- Denman, K. L., G. Brasseur, et al. (2007), Couplings between changes in the climate system and biogeochemistry, in *Climate Change 2007: The Physical Science Basis*, Contribution of Working Group I to the Fourth Assessment Report of the Intergovernmental Panel on Climate Change, edited by S. Solomon, D. Qin, M. Manning, M. Marquis, K. Averyt, M. M. B. Tignor, H. L. Miller, and Z. Chen, Cambridge University Press, Cambridge (UK), 499-587.
- Dessler, A. E. and S. Wong (2009), Estimates of the water vapour climate feedback during El Niño-Southern Oscillation, *J. Clim.*, 22, 6404-6412.
- Dickinson, R. E. (2011) Interaction between future climate and terrestrial carbon and nitrogen, in A. Henderson-Sellers (editor), *The Future of the World's Climate*, Elsevier Climate.
- Dorrepaal, E., S. Toet, R. S. P. van Logstestijn, E. Swart, M. J. van de Weg, T. V. Callaghan, and R. Aerts (2009), Carbon respiration from subsurface peat accelerated by climate warming in the subarctic, *Nature*, 460, 616-620.
- Doutriaux-Boucher, M., M. J. Webb, J. M. Gregory, and O. Boucher (2009), Carbon dioxide induced stomatal closure increases radiative forcing via a rapid reduction in low cloud, *Geophys. Res. Lett.*, 36, L02703, doi:10.1029/2008GL036273.
- Dyer, G. (2008) *Climate Wars*, Random House Canada, 267 pages.
- Fedorov, A. V., R. C. Pacanowski, S. G. Philander, G. Boccaletti (2004), The Effect of Salinity on the Wind-Driven Circulation and the Thermal Structure of the Upper Ocean. *J. Phys. Oceanogr.*, 34, 1949-1966.
- Fedorov, A.V., P. S. Dekens, M. McCarthy, A. C. Ravelo, P. B. deMenocal, M. Barreiro, R. C. Pacanowski and S. G. Philander (2006), The Pliocene paradox (mechanisms for a permanent El Niño), *Science*, 312, 1485-1489.
- Feeley, K., S. J. Wright, M. N. N. Supardi, A. R. Kassim and S. J. Davies (2007), Decelerating growth in tropical forest trees, *Ecol. Lett.*, 10, 461-469.
- Fettweis, X., J.-P. van Ypersele, H. Gallée, H. Lefebvre and W. Lefebvre (2007), The 1979-2005 Greenland ice melt extent from passive microwave data using an improved version of the melt retrieval XPRG algorithm, *Geophys. Res. Lett.* 34, L05502.

- Forest, C. E., P. H. Stone, and A. P. Sokolov (2008), Constraining climate model parameters from observed 20th century changes, *Tellus*, 60A, 911-920.
- Forster, P., V. Ramaswamy, et al. (2007), Changes in atmospheric constituents and in radiative forcing, in *Climate Change 2007: The Physical Science Basis*, Contribution of Working Group I to the Fourth Assessment Report of the Intergovernmental Panel on Climate Change, edited by S. Solomon, D. Qin, M. Manning, M. Marquis, K. Averyt, M. M. B. Tignor, H. L. Miller, and Z. Chen, Cambridge University Press, Cambridge (UK), 129-234.
- Friedlingstein, P., P. Cox, R. Betts, L. Bopp, W. von Bloh, V. Brovkin, P. Cadule, S. Doney, M. Eby, I. Fung, G. Bala, J. John, C. Jones, F. Joos, T. Kato, M. Kawamiya, W. Knorr, K. Lindsay, H. D. Matthews, T. Raddatz, P. Rayner, C. Reick, E. Roeckner, K.-G. Schnitzler, R. Schnur, K. Strassmann, A. J. Weaver, C. Yoshikawa, and N. Zeng (2006), Climate-carbon cycle feedback analysis: results from the C⁴MIP model intercomparison, *J. Clim.*, 19, 3337-3353.
- Fyfe, J. C. and O. A. Saenko (2006), Simulated changes in the extratropical Southern hemisphere winds and currents, *Geophys. Res. Lett.*, 33, L06701, doi:10.1029/2005GL025332.
- Gettelman, A. and Q. Fu (2008), Observed and simulated upper-tropospheric water vapor feedback, *J. Clim.*, 21, 3282-3289.
- Gillett, N. P., A. J. Weaver, F. W. Zwiers, and M. D. Flannigan (2004), Detecting the effect of climate change on Canadian forest fires, *Geophys. Res. Lett.*, 31, L18211, doi:10.1029/2004GL020876.
- Gregory, J. M., W. J. Ingram, M. A. Palmer, G. S. Jones, P. A. Stott, R. B. Thorpe, J. A. Lowe, T. C. Johns, and K. D. Williams (2004), A new method for diagnosing radiative forcing and climate sensitivity, *Geophys. Res. Lett.*, 31, L03205, doi:10.1029/2003GL018747.
- Gregory, J. M. and P. M. Forster (2008), Transient climate response estimated from radiative forcing and observed temperature change, *J. Geophys. Res.*, 113, D23105, doi:10.1029/2008JD010405.
- Gregory, J. M., C. D. Jones, P. Cadule, and P. Friedlingstein (2009), Quantifying carbon cycle feedbacks, *J. Clim.*, 22, 5232-5250.
- Gregory, J. and M. Webb (2008), Tropospheric adjustment induces a cloud component to CO₂ forcing, *J. Clim.*, 21, 58-71.
- Gurney, K. R., D. Baker, and S. Denning (2008), Interannual variations in continental-scale net carbon exchange and sensitivity to observing networks estimated from atmospheric CO₂ inversions for the period 1980 to 2005, *Glob. Biogeochem. Cycles*, 22, GB3025, doi:10.1029/2007GB003082.
- Harvey, L. D. D. (2001), A quasi-one-dimensional coupled climate-carbon cycle model, Part II: The carbon cycle component, *J. Geophys. Res.*, 106, 22355-22372.
- Harvey, L. D. D. (2010a), *Energy and the New Reality, Volume 1: Energy Efficiency and the Demand for Energy Services*, Earthscan, London, UK.

- Harvey, L. D. D. (2010b), *Energy and the New Reality, Volume 2: Carbon-free Energy Supply*, Earthscan, London, UK.
- Harvey, L. D. D. (2011) Climate and Climate-System Modelling, in J. Wainwright and M. Mulligan (editors), *Environmental Modelling: Finding Simplicity in Complexity*, 2nd Edition, Wiley-Blackwell (in press).
- Harvey, L. D. D., J. Gregory, M. Hoffert, A. Jain, M. Lal, R. Leemans, S. Raper, T. Wigley and J. de Wolde (1997), *An Introduction to Simple Climate Models used in the IPCC Second Assessment Report, Intergovernmental Panel on Climate Change, Technical Paper No. 2*, Intergovernmental Panel on Climate Change, World Meteorological Organization, Geneva.
- Harvey, L. D. D. and Z. Huang (1995), Evaluation of the potential impact of methane clathrate destabilization on future global warming, *J. Geophys. Res.*, 100, 2905-2926.
- Harvey, L. D. D. and Z. Huang (2001), A quasi-one-dimensional coupled climate-carbon cycle model, Part I: Description and behaviour of the climate component, *J. Geophys. Res.*, 106, 22339-22353.
- Harvey, L. D. D. and R. K. Kaufmann (2002), Simultaneously constraining climate sensitivity and aerosol radiative forcing, *J. Clim.*, 15, 2837-2861.
- Herrmann, A. D., M. E. Patzkowsky, and D. Pollard (2004), The impact of paleogeography, pCO₂, poleward ocean heat transport and sea level change on global cooling during the late Ordovician, *Palaeogeogr. Palaeoclimat. Palaeoecol.*, 206, 59-74.
- Hesselbo, S. P., D. R. Gröcke, H. C. Jenkyns, C. J. Bjerrum, P. Farrimond, H. S. M. Bell, and O. R. Green (2000), Massive dissociation of gas hydrate during a Jurassic oceanic anoxic event, *Nature*, 406, 392-395.
- Hoffert, M. I. and C. Covey (1992), Deriving global climate sensitivity from paleoclimate reconstructions, *Nature*, 360, 573-576.
- Hu, F. S., P. E. Higuera, J. E. Walsh, W. L. Chapman, P. A. Duffy, L. B. Brubaker, and M. L. Chipman (2010), Tundra burning in Alaska: Linkage to climatic change and sea ice retreat, *J. Geophys. Res.*, 115, G04002, doi:10.1029/2009/JG001270.
- Hungate, B. A., P. D. Stiling, P. Dijkstra, D. W. Johnson, M. E. Ketterer, G. J. Hymus, C. R. Hinkle, and B. G. Drake (2004), CO₂ elicits long-term decline in nitrogen fixation, *Science*, 304, 1291, doi:10.1126/science.1095549.
- Ise, T., A. L. Dunn, S. C. Wofsy, and P. R. Moorcroft (2008), High sensitivity of peat decomposition to climate change through water-table feedback, *Nature Geoscience*, 1, 763-766.
- Jones, C., J. Lowe, S. Liddicoat, and B. Richard (2009), Committed terrestrial ecosystem changes due to climate change, *Nature Geoscience*, 2, 484-487.
- Juday, G. P., V. Barber, P. Duffy, H. Linderholm, S. Rupp, S. Sparrow, E. Vaganov and J. Yarie (2005), Forests, land management, and agriculture, in *Arctic Climate Impact Assessment*,

Scientific Report, Cambridge University Press, Cambridge UK and New York, NY, USA, pp781-862.

- Kasischke, E. S. and M. R. Turetsky (2006), Recent changes in the fire regime across the North American boreal region – spatial and temporal patterns of burning across Canada and Alaska, *Geophys. Res. Lett.*, 33, L09703, doi:10.1029/2006GL025677.
- Kasischke, E. S., D. L. Verbyla, T. S. Rupp, A. D. McGuire, K. A. Murphy, R. Jandt, J. L. Barnes, E. E. Hoy, P. A. Duffy, M. Calef and M. R. Turetsky (2010), Alaska's changing fire regime – implications for the vulnerability of its boreal forests, *Can. J. For. Res.*, 40, 1313-1324.
- Kennedy, M., D. Mrofka and C. von der Borch (2008), Snowball Earth termination by destabilization of equatorial permafrost methane clathrate, *Nature*, 453, 642-645.
- Kennett, J. P., K. G. Cannariato, I. L. Hendy, and R. J. Behl (2000), Carbon isotope evidence for methane hydrate instability during Quaternary interstadials, *Science*, 288, 128-133.
- Khvorostyanov, D. V., P. Ciais, G. Krinner, and S. A. Zimov (2008a), Vulnerability of east Siberia's frozen carbon stores to future warming, *Geophys. Res. Lett.*, 35, L10703, doi:10.1029/2008GL033639.
- Khvorostyanov, D. V., P. Ciais, G. Krinner, S. A. Zimov, Ch. Corrado, and G. Guggenberger (2008b), Vulnerability of permafrost carbon to global warming. Part II: sensitivity of permafrost carbon stock to global warming, *Tellus*, 60B, 265-275.
- Knutti, R., G. A. Meehl, M. R. Allen, and D. A. Stainforth (2006), Constraining climate sensitivity from the seasonal cycle in surface temperature, *J. Clim.*, 19, 4224-4233.
- Kopp, R.E., F. J. Simons, J. X. Mitrovica, A. C. Maloof, and M. Oppenheimer (2009) Probabilistic assessment of sea level during the last interglacial stage, *Nature* **462**, 863-868
- Kump, L. R. and D. Pollard (2008), Amplification of Cretaceous warmth by biological cloud feedbacks, *Science*, 320, 195.
- Kuzyakov, Y. (2002), Review: factors affecting rhizosphere priming effects, *J. Plant Nutri. Soil Sci.*, 165, 382-396.
- Kurz, W. A., C. C. Dymond, G. Stinson, G. J. Rampley, E. T. Neilson, A. L. Carroll, T. Ebata and L. Safranyik (2008), Mountain pine beetle and forest carbon feedback to climate change, *Nature*, 452, 987-990.
- Kvenvolden, K. A. and B. W. Rogers (2005), Gaia's breath – global methane exhalations, *Mar. Petro. Geol.*, 22, 579-590.
- Kwon, E. Y., F. Primeau, and J. L. Sarmiento (2009), The impact of remineralization depth on the air-sea carbon balance, *Nature Geoscience*, 2, 630-635.
- Lambert, F., B. Delmonte, J. R. Petit, M. Bigler, P. R. Kaufmann, M. A. Hutterli, T. F. Stocker, U. Ruth, J. P. Steffensen, and V. Maggi (2008), Dust-climate couplings over the past 800,000 years from the EPICA Dome C ice core, *Nature*, 452, 616-619.

- Laurance, W. F. (2000) Mega-development trends in the Amazon: Implications for global change, *Env. Monit. Assess.*, 61, 113-122.
- Lawrence, D. M. and A. G. Slater (2005), A projection of severe near-surface permafrost degradation during the 21st century, *Geophys. Res. Lett.*, 32, L24401, doi:10.1029/2005GL025080.
- Lenton, A., F. Codron, L. Bopp, N. Metzl, P. Cadule, A. Tagliabue and J. Le Sommer (2009), Stratospheric ozone depletion reduces ocean carbon uptake and enhances ocean acidification, *Geophys. Res. Lett.*, 36, L12606, doi:10.1029/2009GL038227.
- Le Quéré, C., C. Rödenbeck, E. T. Buitenhuis, T. J. Conway, R. Langenfelds, A. Gomez, C. Labuschagne, M. Ramonet, T. Nakazawa, N. Metzl, N. Gillett, and M. Heimann (2007), Saturation of the Southern Ocean CO₂ sink due to recent climate change, *Science*, 316, 1735-1738.
- Le Quéré, C., T. Takahashi, E. T. Buitenhuis, C. Rödenbeck, and S. C. Sutherland (2010), Impact of climate change and variability on the global oceanic sink of CO₂, *Glob. Biogeochem. Cycles*, 24, GB4007, doi:10.1029/2009GB003599.
- Lea, D. W. (2004), The 100000-yr cycle in tropical SST, greenhouse forcing, and climate sensitivity, *J. Clim.*, 17, 2170-2179.
- Lefèvre, N., A. J. Watson, A. Olsen, A. F. Ríos, F. F. Pérez, and T. Johannessen (2004), A decrease in the sink for atmospheric CO₂ in the North Atlantic, *Geophys. Res. Lett.*, 31, L07306, doi:10.1029/2003GL018957.
- López-Urrutia, Á., E. San Martín, R. P. Harris, and X. Irigoien (2006) Scaling the metabolic balance of the oceans, *Proc. Nat. Acad. Sci.*, 103, 8739-8744.
- Malcolm, G. M., J. C. López-Gutiérrez, R. T. Koide, and D. M. Eissenstat (2008), Acclimation to temperature and temperature sensitivity of metabolism by ectomycorrhizal fungi, *Global Change Biology*, 14, 1169-1180.
- Malhi, Y., L. E. O. Aragão, D. Galbraith, C. Huntingford, R. Fisher, P. Zelazowski, S. Sitch, C. McSweeney, and P. Meir (2009), Exploring the likelihood and mechanism of a climate-change-induced dieback of the Amazon rainforest, *Proc. Nat. Acad. Sci.*, 106, 20610-20615.
- Martinez, E., D. Antoine, F. D'Ortenzio, and B. Gentili (2009), Climate-driven basin-scale decadal oscillations of oceanic phytoplankton, *Science*, 326, 1253-1256.
- Matthews, E. (1997), Global litter production, pools, and turnover times: Estimates from measurement data and regression models, *J. Geophys. Res.*, 102, 18771-18800.
- Matthews, H. D., M. Eby, T. Ewen, P. Friedlingstein, and B. J. Hawkins (2007), What determines the magnitude of carbon-cycle climate feedbacks? *Glob. Biogeochem. Cycles*, 21, GB2012, doi:10.1029/2006GB002733.

- Matthews, H. D. and D. W. Keith (2007), Carbon-cycle feedbacks increase the likelihood of a warmer future, *Geophys. Res. Lett.*, 34, L09702, doi:10.1029/2006GL028685.
- McCarthy, M. P., P. W. Thorne and H. A. Titchner (2009), An analysis of tropospheric humidity trends from radiosondes, *J. Clim.*, 22, 5820-5838.
- McDowell, N., W. T. Pockman, C. D. Allen, D. D. Breshears, N. Cobb, T. Kolb, J. Plaut, J. Sperry, A. West, D. G. Williams, and E. A. Yezzer (2008), Mechanisms of plant survival and mortality during drought: why do some plants survive while others succumb to drought? *New Phytologist*, 178, 719-739.
- Meehl, G. A., T. F. Stocker, W. D. Collins, P. Friedlingstein, A. T. Gaye, J. M. Gregory, A. Kitoh, J. M. Murphy, A. Noda, S. C. B. Raper, I. G. Watterson, A. J. Weaver and Z.-C. Zhao (2007), Global climate projections, in *Climate Change 2007: The Physical Science Basis*, Contribution of Working Group I to the Fourth Assessment Report of the Intergovernmental Panel on Climate Change, edited by S. Solomon, D. Qin, M. Manning, M. Marquis, K. Averyt, M. M. B. Tignor, H. L. Miller, and Z. Chen, Cambridge University Press, Cambridge (UK), 747-845.
- Minschwaner, K. and A. E. Dessler (2004), Water vapor feedback in the tropical upper troposphere: Model results and observations, *J. Clim.*, 17, 1272-1282.
- Minschwaner, K., A. E. Dessler, and P. Sawaengphokhai (2006), Multimodel analysis of the water vapor feedback in the tropical upper troposphere, *J. Clim.*, 19, 5455-5463.
- Morán, X. A. G., Á. López-Urrutia, A. Calvo-Díaz, and W. K. W. Li (2010), Increasing importance of small phytoplankton in a warmer ocean, *Global Change Biology* 16, 1137-1144.
- Nakicenovic, N., J. Alcamo, G. Davis, B. de Vries, J. Fenhann, S. Gaffin, K. Gregory, A. Grübler, T. Y. Jung, T. Kram, E. L. La Rovere, L. Michaelis, S. Mori, T. Morita, W. Pepper, H. Pitcher, L. Price, K. Raihi, A. Roehrl, H.-H. Rogner, A. Sankovski, M. Schlesinger, P. Shukla, S. Smith, R. Swart, S. van Rooijen, N. Victor and Z. Dadi (2000), *Emission Scenarios*, Special Report of the Intergovernmental Panel on Climate Change, edited by N. Nakicenovic and S. Swart, Cambridge University Press, Cambridge.
- Nepstad, D. C., I. M. Tohver, D. Ray, P. Moutinho, and G. Cardinot (2007), Mortality of large trees and lianas following experimental drought in an Amazon forest, *Ecology*, 88, 2259-2269.
- Norby, R. J., J. M. Warren, C. M. Iversen, B. E. Medlyn, and R. E. McMurtrie (2010), CO₂ enhancement of forest productivity constrained by limited nitrogen availability, *Proc. Nat. Acad. Sci.*, 107, 19368-19373.
- Notaro, M., S. Vavrus, and Z. Liu (2007) Global vegetation and climate change due to future increases in CO₂ as projected by a fully coupled model with dynamic vegetation, *J. Clim.*, 20, 70-90.
- O'ishi, R. and A. Abe-Ouchi, (2009) Influence of dynamic vegetation on climate change arising from increasing CO₂, *Clim. Dyn.*, 33, 645-663.

- O'ishi, R., A. Abe-Ouchi, I. C. Prentice, and S. Sitch, (2009) Vegetation dynamics and plant CO₂ responses as positive feedbacks in a greenhouse world, *Geophys.Res. Lett.*, 36, L11706, doi:10.1029/2009GL038217.
- Oechel, W. C., G. L. Vourlitis, S. J. Hastings, R. C. Zulueta, L. Hinzman, and D. Kane (2000), Acclimation of ecosystem CO₂ exchange in the Alaskan Arctic in response to decadal climate warming, *Nature*, 406, 978-981.
- Omta, A. W., J. Bruggeman, S. A. L. M. Kooijman, and H. A. Dijkstra (2006), Biological carbon pump revisited: Feedback mechanisms between climate and the Redfield ratio, *Geophys. Res. Lett.*, 33, L14613, doi:10.1029/2006GL026213.
- Ow, L. F., D. Whitehead, A. S. Walcroft, and M. H. Turnbull (2010), Seasonal variation in foliar carbon exchange in *Pinus radiata* and *Populus deltoides*: respiration acclimates fully to changes in temperature but photosynthesis does not, *Global Change Biology*, 16, 288-302.
- Pagani, M., K. Caldeira, D. Archer, and J. C. Zachos (2006), An ancient carbon mystery, *Science*, 314, 1556-1557.
- Pagani, M., Z. Liu, J. LaRiviere, and A. C. Ravelo (2010), High Earth-system climate sensitivity determined from Pliocene carbon dioxide concentrations, *Nature Geoscience*, 3, 27-30.
- Page, S. E., F. Siegert, J. O. Rieley, H. -D. V. Boehm, A. Jaya, and S. Limin (2002), The amount of carbon released from peat and forest fires in Indonesia during 1997, *Nature*, 420, 61-65.
- Page, S. E., R. A. J. Wüst, D. Weiss, J. O. Rieley, W. Shotyk and S. H. Limin (2004) A record of Late Pleistocene and Holocene carbon accumulation and climate change from an equatorial peat bog (Kalimantan, Indonesia): implications for past, present and future carbon dynamics, *J. Quat. Sci.*, 19, 625-635.
- Park, J. and D. L. Royer (2011), Geologic constraints on the glacial amplification of Phanerozoic climate sensitivity, *J. Geophys. Res.*, **VOL, XXXX**, doi:10.1029/YYYYY.
- Patzek, T. W. and G. D. Croft (2010) A global coal production forecast with multi-Hubbert cycle analysis, *Energy Policy*, 35, 3109-3122.
- Pearson, P. N., G. L. Foster, and B. S. Wade (2009), Atmospheric carbon dioxide through the Eocene-Oligocene climate transition, *Nature*, 461, 1110-1113.
- Pendall, E., S. del Grosso, J. Y. King, D. R. LeCain, D. G. Milchunas, J. A. Morgan, A. R. Mosier, D. S. Ojima, W. A. Parton, P. P. Tans, and J. W. C. White (2003), Elevated atmospheric CO₂ effects and soil water feedbacks on soil respiration components in a Colorado grassland, *Glob. Biogeochem. Cycles*, 17, 1046, doi:10.1029/2001GB001821.
- Phillips, O. L., L. E. O. C. Aragão, S. L. Lewis, J. B. Fisher, J. Lloyd, G. López-González, Y. Malhi, A. Monteagudo, J. Peacock, Carlos A. Quesada, G. van der Heijden, S. Almeida, I. Amaral, L. Arroyo, G. Aymard, T. R. Baker, O. Bánki, L. Blanc, D. Bonal, P. Brando, J. Chave, Á. C. A. de Oliveira, N. D. Cardozo, C. I. Czimczik, T. R. Feldpausch, M. A. Freitas, E. Gloor, N. Higuchi, E. Jiménez, G. Lloyd, P. Meir, C. Mendoza, A. Morel, D. A. Neill, D. Nepstad, S. Patiño, M. C. Peñuela, A. Prieto, F. Ramírez, M. Schwarz, J. Silva, M. Silveira, A. S. Thomas, H. ter Steege, J. Stropp, R. Vásquez, P. Zelazowski, E. A. Dávila, S.

- Andelman, A. Andrade, K.-J. Chao, T. Erwin, A. Di Fiore, E. Honorio C., H. Keeling, T. J. Killeen, W. F. Laurance, A. Peña Cruz, N. C. A. Pitman, P. Núñez Vargas, H. Ramírez-Angulo, A. Rudas, R. Salamão, N. Silva, J. Terborgh, and A. Torres-Lezama (2009), Drought sensitivity of the Amazon rainforest, *Science*, 323, 1344-1347.
- Piao, S., P. Friedlingstein, P. Ciais, L. Zhou, and A. Chen (2006), Effect of climate and CO₂ changes on the greening of the Northern Hemisphere over the past two decades, *Geophys. Res. Lett.*, 33, L23402, doi:10.1029/2006GL028205.
- Pisaric, M. F. J., S. K. Carye, S. V. Kokelj, and D. Youngblut (2007), Anomalous 20th century tree growth, Mackenzie Delta, Northwest Territories, Canada, *Geophys. Res. Lett.*, 34, L05714, doi:10.1029/2006GL029139.
- Plattner, G. -K., R. Knutti, F. Joos, T. F. Stocker, W. von Bloh, V. Brovkin, D. Cameron, E. Driesschaert, S. Dutkiewicz, M. Eby, N. R. Edwards, T. Fichefet, J. C. Hargreaves, C. D. Jones, M. F. Loutre, H. D. Matthews, A. Mouchet, S. A. Müller, S. Nawrath, A. Price, A. Sokolov, K. M. Strassmann, and A. J. Weaver (2008), Long-term climate commitments projected with climate-carbon cycle models, *J. Clim.*, 21, 2721-2751.
- Polovina, J. J., E. A. Howell and M. Abecassis (2008), Ocean's least productive waters are expanding, *Geophys. Res. Lett.*, 35, L03618, doi:10.1029/2007GL031745.
- Poulter, B., F. Hattermann, E. Hawkins, S. Zaehles, S. Sitch, N. Restrepo-Coupe, U. Heyder, and W. Cramer (2010), Robust dynamics of Amazon dieback to climate change with perturbed ecosystem model parameters, *Global Change Biology*, 16, 2476-2495.
- Prentice, I. C., G. D. Farquhar, M. J. R. Fasham, M. L. Goulden, M. Heimann, V. J. Jaramillo, H. S. Khesghi, C. Le Quéré, R. J. Sholes, and D. W. R. Wallace (2001) The carbon cycle and atmospheric carbon dioxide, in J. T. Houghton, Y. Ding, D. J. Griggs, M. Noguer, P. J. van der Linden, X. Dai, K. Maskell and C. A. Johnson (editors), *Climate Change 2001: The Scientific Basis*, Contribution of Working Group I to the Third Assessment Report of the Intergovernmental Panel on Climate Change. Cambridge University Press, Cambridge (UK), 183-237.
- Qian, H., R. Joseph, and N. Zing (2008), Response of the terrestrial carbon cycle to the El Niño-Southern Oscillation, *Tellus*, 60B, 537-550.
- Qui, J. (2009), Tundra's burning, *Nature*, 461, 34-36.
- Rafelski, L. E., S. C. Piper, and R. F. Kelling (2009), Climate effects on atmospheric carbon dioxide over the last century, *Tellus*, 61B, 718-731.
- Raffa, K.F., B. H. Aukema, B. J. Bentz, A. L. Carroll, J. A. Hicke, M. G. Turner and W. H. Romme (2008) Cross-scale drivers of natural disturbances prone to anthropogenic amplification: the dynamics of bark beetle eruptions, *BioScience*, 58, 501-517.
- Reagan, M. T. and G. J. Moridis (2007), Oceanic gas hydrate instability and dissociation under climate change scenarios, *Geophys. Res. Lett.*, 34, L22709, doi:10.1029/2007GL031671.

- Reagan, M. T. and G. J. Moridis (2009), Large-scale simulation of methane hydrate dissociation along the West Spitsbergen margin, *Geophys. Res. Lett.*, 36, L23612, doi:10.1029/2009GL041332.
- Reichstein, M., P. Ciais, D. Papale, R. Valentini, S. Running, N. Viovy, W. Cramer, A. Granier, J. Ogée, V. Allard, M. Aubinet, Chr. Bernhofer, N. Buchmann, A. Carrara, T. Grünwald, M. Heimann, B. Heinesch, A. Knohl, W. Kutsch, D. Loustau, G. Manca, G. Matteucci, F. Miglietta, J. M. Ourcival, K. Pilegaard, J. Pumpanen, S. Rambal, S. Schaphoff, G. Seufert, J.-F. Soussana, M.-J. Sanz, T. Vesala, and M. Zhao (2007), Reduction of ecosystem productivity and respiration during the European summer 2003 climate anomaly: a joint flux tower, remote sensing and modelling analysis, *Global Change Biology*, 13, 634-651.
- Reth, S., W. Graf, M. Reichstein, and J. C. Munch (2009), Sustained stimulation of soil respiration after 10 years of experimental warming, *Environ. Res. Lett.*, 4(024005), doi:10.1088/1748-9326/4/2/024005.
- Riebesell, U., A. Körtzinger and A. Oschlies (2009), Sensitivities of marine carbon fluxes to ocean change. *Proc. Nat. Academy Sciences*, 106, 20602-20609.
- Royer, D. L. (2006), CO₂-forced climate thresholds during the Phanerozoic, *Geochemica Cosmochimica Acta*, 70, 5665-5675.
- Royer, D. L., R. A. Berner, and J. Park (2007), Climate sensitivity constrained by CO₂ concentrations over the past 420 million years, *Nature*, 446, 530-532.
- Running, S. W. (2006) Is global warming causing more, larger wildfires? *Science*, 313, 927-928.
- Rütting, T., T. J. Clough, C. Müller, M. Lieffering and P. C. D. Newton (2010), Ten years of elevated atmospheric carbon dioxide alters soil nitrogen transformations in a sheep-grazed pasture, *Global Change Biology*, 16, 2530-2542.
- Salazar, L. F., C. A. Nobre, and M. D. Oyama (2007), Climate change consequences on the biome distribution in tropical South America, *Geophys. Res. Lett.* 34, L09708, doi:10.1029/2007GL029695.
- Schaefer, K., T. Zhang, L. Bruhwiler and A. P. Barrett (2011), Amount and timing of permafrost carbon release in response to climate warming, *Tellus*, 63B, 1-16.
- Schlesinger, M. E. (1985), Appendix A: Analysis of results from energy balance and radiative convective models, in *Projecting the Climatic Effects of Increasing Carbon Dioxide*, edited by M. C. MacCracken and F. M. Luther, US Department of Energy, DOE/ER-0237, 281-319.
- Schneider, B. and R. Schneider (2010), Global warmth with little extra CO₂, *Nature Geoscience*, 3, 6-7.
- Schneider von Deimling, T., H. Held, A. Ganopolski, and S. Rahmstorf (2006), Climate sensitivity estimated from ensemble simulations of glacial climate, *Clim. Dyn.*, 27, 149-163.

- Schuster, U. and A. J. Watson (2007), A variable and decreasing sink for atmospheric CO₂ in the North and Atlantic, *J. Geophys. Res.*, 112, C11006, doi:10.1029/2006JC003941.
- Secord, R., P. D. Gingerich, K. C. Lohmann, and K. G. Macleod (2010), Continental warming preceding the Palaeocene-Eocene thermal maximum, *Nature*, 467, 955-958.
- Seiler, T.J., D. P. Rasse, J. Li, P. Dijkstra, H. P. Anderson, D. P. Johnson, T. L. Powell, B. A. Hungate, C. R. Hinkle and B. G. Drake (2009) Disturbance, rainfall and contrasting species responses mediated aboveground biomass response to 11 years of CO₂ enrichment in a Florida scrub-oak ecosystem, *Global. Change Biology*, 15, 356-367.
- Sellers, P.J., L. Bounoua, G. J. Collatz, D. A. Randall, D. A. Dazlich, S. O. Los, J. A. Berry, I. Fung, C. J. Tucker, C. B. Field, and T. G. Jensen (1996), Comparison of radiative and physiological effects of doubled atmospheric CO₂ on climate, *Science*, 271, 1402-1406.
- Shakhova, N., I. Semiletov, I. Leifer, A. Salyuk, P. Rekant, and D. Kosmach (2010a), Geochemical and geophysical evidence of methane release over the East Siberian Arctic Shelf, *J. Geophys. Res.*, 115, C08007, doi:10.1029/2009JC005602.
- Shakhova, N., I. Semiletov, A. Salyuk, V. Yusupov, D. Mosmach, and Ö. Gustafsson (2010b), Extensive methane venting to the atmosphere from sediments of the East Siberian Arctic shelf, *Science*, 327, 1246-1250.
- Sherwood, S. C. and M. Huber (2010), An adaptability limit to climate change due to heat stress, *Proc. Nat. Acad. Sci.*, 107, 9522-9555.
- Shindell, D. T. and G. A. Schmidt (2004), Southern Hemisphere climate response to ozone changes and greenhouse gas increases, *Geophys. Res. Lett.*, 31, 31, L18209, doi:10.1029/2004GL020724.
- Shindell, D. T., B. P. Walter, and G. Faluvegi (2004), Impacts of climate change on methane emissions from wetlands, *Geophys. Res. Lett.*, 31, L21202, doi:10.1029/2004GL021009.
- Sluijs, A., H. Brinkhuis, S. Schouten, S. M. Bohaty, C. M. John, J. C. Zachos, G. -J. Reichert, J. S. S. Damsté, E. M. Crouch, and G. R. Dickens (2007), Environmental precursors to rapid light carbon injection at the Paleocene/Eocene boundary, *Nature*, 450, 1218-1221.
- Sluijs, A., S. Schouten, M. Pagani, M. Woltering, H. Brinkhuis, J. S. S. Damsté, G. R. Dickens, M. Huber, G.-J. Reichert, R. Stein, J. Matthiessen, L. J. Lourens, N. Pedentchouk, J. Backman, K. Moran & the Expedition 302 Scientists (2006), Subtropical Arctic Ocean temperatures during the Palaeocene/Eocene thermal maximum, *Nature*, 441, 610-613.
- Soden, B. J. and I. M. Held (2006), An assessment of climate feedbacks in coupled ocean-atmosphere models, *J. Clim.*, 19, 3354-3363 and 6263.
- Soden, B. J., I. M. Held, R. Colman, K. M. Shell, J. T. Kiehl, and C. A. Shields (2008), Quantifying climate feedbacks using radiative kernels, *J. Clim.*, 21, 3504-3520.
- Soden, B. J., R. T. Wetherald, G. L. Stenchikov, and A. Robock (2002), Global cooling after the eruption of Mount Pinatubo: A test of climate feedback by water vapor, *Science*, 296, 727-730.

- Soja, A. J., N. M. Tchebakova, N. H. F. French, M. D. Flannigan, H. H. Shugart, B. J. Stocks, A. I. Shukhinin, E. I. Parfenova, F. S. Chapin III and P. W. Stackhouse Jr. (2007), Climate-induced boreal forest change: Predictions versus current observations, *Glob. Planet. Change*, 56, 274-296.
- Steinacher, M., F. Joos, T. L. Frölicher, L. Bopp, P. Cadule, V. Cocco, S. C. Doney, M. Gehlen, K. Lindsay, J. K. Moore, B. Schneider, and J. Segschneider (2010), Projected 21st century decrease in marine productivity: a multi-model analysis, *Biogeosciences*, 7, 979-1005.
- Stephens, B. B., K. R. Gurney, P. P. Tans, C. Sweeney, W. Peters, L. Bruhwiler, P. Ciais, M. Ramonet, P. Bousquet, T. Nakazawa, S. Aoki, T. Machida, G. Inoue, N. Vinnichenko, J. Lloyd, A. Jordan, M. Heimann, O. Shibistova, R. L. Langenfelds, L. P. Steele, R. J. Francey, and A. S. Denning (2007), Weak northern and strong tropical land carbon uptake from vertical profiles of atmospheric CO₂, *Science*, 316, 1732-1735.
- Stocks, B. J., J. A. Mason, J. B. Todd, E. M. Bosch, B. M. Wotton, B. D. Amiro, M. D. Flannigan, K. G. Hirsch, K. A. Logan, D. L. Martell, and W. R. Skinner (2003), Large forest fires in Canada, 1959-1997, *Journal of Geophysical Research*, 108(D1), 8149, doi:10.1029/2001JD000484.
- Tarnocai, C., J. G. Canadell, E. A. G. Schuur, G. Mazhitova, and S. Zimov (2009), Soil organic carbon pools in the northern circumpolar permafrost region, *Glob. Biogeochem. Cyc.*, 23, GB2023, doi:10.1029/2008GB003327.
- Thornton, P. E., S. C. Doney, K. Lindsay, J. K. Moore, N. Mahowald, J. T. Randerson, I. Fung, J. -F. Lamarque, J. J. Feddema and Y. -H. Lee (2009), Carbon-nitrogen interactions regulate climate-carbon cycle feedbacks: results from an atmosphere-ocean general circulation model, *Biogeosciences*, 6, 2099-2120.
- Tingey, D. T., E. H. Lee, R. Waschmann, M. G. Johnson, and P. T. Rygielwicz (2006), Does soil CO₂ efflux acclimatize to elevated temperature and CO₂ during long-term treatment of Douglas-fir seedlings? *New Phytologist*, 170, 107-118.
- Tripathi, A. K., C. D. Roberts, and R. A. Eagle (2009), Coupling of CO₂ and ice sheet stability over major climate transitions of the last 20 million years, *Science*, 326, 1394.
- Turetsky, M., K. Wieder, L. Halsey, and D. Vitt (2002), Current disturbance and the diminishing peatland carbon sink, *Geophys. Res. Lett.*, 29, 1526, doi:10.1029/2001GL014000.
- van Kessel, C., B. Boots, M.-A. de Graaff, D. Harris, H. Blum and J. Six (2006), Total soil C and N sequestration in a grassland following 10 years of free air CO₂ enrichment, *Global Change Biology*, 12, 2187-2199.
- Van Mantgem, P.J., N. L. Stephenson, J. C. Byrne, L. D. Daniels, J. F. Franklin, P. Z. Fulé, M. E. Harmon, A. J. Larson, J. M. Smith, A. H. Taylor, and T. T. Veblen (2009), Widespread increase in tree mortality rates in the western United States, *Science*, 323, 521-524.
- Vázquez-Domínguez, E., D. Vaqué, and J. M. Gasol (2007), Ocean warming enhances respiration and carbon demand of coastal microbial plankton, *Global Change Biology*, 13, 1327-1334.

- Velicogna, I. (2009) Increasing rates of ice mass loss from the Greenland and Antarctic ice sheets revealed by GRACE, *Geophys. Res. Lett.*, **36**, L19503, doi:10.1029/2009GL040222
- Wagner, T., S. Beirle, M. Grzegorski, and U. Platt (2006), Global trends (1996-2003) of total column precipitable water observed by Global Ozone Monitoring Experiment (GOME) on ERS-2 and their relation to near-surface temperature, *J. Geophys. Res.*, **111**, D12102, doi:10.1029/2005JD006523.
- Walter, K. M., S. A. Zimov, J. P. Chanton, D. Verbyla, and F. S. Chapin III (2006), Methane bubbling from Siberian thaw lakes as a positive feedback to climate warming, *Nature*, **443**, 71-75.
- Wan, S., R. J. Norby, J. Ledford, and J. F. Weltzin (2007), Response of soil respiration to elevated CO₂, air warming, and changing soil water availability in a model old-field grassland, *Global Change Biology*, **13**, 2411-2424.
- Wang, Y. -P. and B. Z. Houlton (2009), Nitrogen constraints on terrestrial carbon uptake: Implications for the global carbon-climate feedback, *Geophys. Res. Lett.*, **36**, L24403, doi:10.1029/2009GL041009.
- Way, D. A. and R. F. Sage (2008), Elevated growth temperatures reduce the carbon gain of black spruce [*Picea mariana* (Mill.) B.S.P.], *Global Change Biology*, **14**, 624-636.
- Westbrook, G. K., K. E. Thatcher, E. J. Rohling, A. M. Piotrowski, H. Pälike, A. H. Osborne, E. G. Nisbet, T. A. Minshull, V. Hühnerbach, D. Green, R. E. Fisher, A. J. Crocker, A. Chabert, C. Bolton, A. B. Möller, C. Berndt and A. Aquilina (2009), Escape of methane gas from the seabed along the West Spitsbergen continental margin, *Geophys. Res. Lett.*, **36**, L15608, doi:10.1029/2009GL039191.
- Westerling, A. L., H. G. Hidalgo, D. R. Cayan, and T. W. Swetnam (2006), Warming and earlier spring increase western U.S. forest wildfire activity, *Science*, **313**, 940-943.
- Wigley, T. M. L., C. M. Ammann, B. D. Santer, and S. C. B. Raper (2005), Effect of climate sensitivity on the response to volcanic forcing, *J. Geophys. Res.*, **110**, D09107, doi:10.1029/2004JD005557.
- Williams, K. D., W. J. Ingram, and J. M. Gregory (2008), Time variation of effective climate sensitivity in GCMs, *J. Clim.*, **21**, 5076-5090.
- Yu, Z., J. Loisel, D. P. Brosseau, D. W. Beilman, and S. J. Hunt (2010), Global peatland dynamics since the Last Glacial Maximum, *Geophys. Res. Lett.*, **37**, L13402, doi:10.1029/2010GL043584.
- Zachos, J., M. Pagani, L. Sloan, E. Thomas, and K. Billups (2001), Trends, rhythms, and aberrations in global climate 65 Ma to present, *Science*, **292**, 686-693.
- Zachos, J. C., G. R. Dickens, and R. E. Zeebe (2008), An early Cenozoic perspective on greenhouse warming and carbon cycle-dynamics, *Nature*, **451**, 279-283.

Zaehle, S., P. Friedlingstein, and A. D. Friend (2010), Terrestrial nitrogen feedbacks may accelerate future climate change, *Geophys. Res. Lett.*, 37, L01401, doi:10.1029/2009GL041345.

Zeebe, R. E., J. C. Zachos, and G. R. Dickens (2009), Carbon dioxide forcing alone insufficient to explain Palaeocene-Eocene thermal maximum warming, *Nature Geoscience*, 2, 576-580.

Zhao, M. and S. W. Running (2010) Drought-induced reduction in global terrestrial net primary production from 2000 through 2009, *Science*, 329, 940-943.